Aus dem

Department für Frauengesundheit
Universitäts-Frauenklinik

Characterization of histologically validated Endometriosis by non-invasive, marker independent Raman microspectroscopy

Inaugural-Dissertation
zur Erlangung des Doktorgrades
der Medizin

der Medizinischen Fakultät
der Eberhard-Karls-Universität
zu Tübingen

vorgelegt von
Beyer, Tara

2025

Als Dissertation genehmigt
von der Eberhard-Karls-Universität

Dekan:	Professor Dr. B. Pichler
1. Berichterstatter:	Professorin Dr. K. Schenke-Layland
2. Berichterstatter:	Professor Dr. S. Kommoss

Tag der Disputation: 19.12.2025

Inhaltsverzeichnis

List of Figures 6

List of Tables 7

List of Acronyms and Abbreviations 8

1 Introduction 12

1.1 The Human Uterus 12

1.1.1 Macroscopic Anatomy of the Uterus 12

1.1.2 Microscopic Anatomy of the Uterus 12

1.1.3 Menstrual Cycle 13

1.2 Endometriosis 15

1.2.1 Definition, Epidemiology and Prevalence 15

1.2.2 Pathogenesis 16

1.2.3 Symptoms and Clinical Presentation 16

1.2.4 Distribution of Endometriosis Locations 16

1.2.5 Classification according to r-ASRM and #ENZIAN 18

1.2.6 Therapy and Prognosis 21

1.2.7 Diagnosis 24

1.2.8 Current Screening and Diagnostic Options 25

1.2.9 Subject of current research 28

1.2.10 Endometriotic Tissue Characterization 29

1.3 Raman Microspectroscopy 29

1.3.1 Basic Principles of Raman Microspectroscopy 30

1.3.2 Inelastic Scattering – Raman Scattering 30

1.4 Prospects of RMS 31

1.5 Aim of the Study 33

2 Material and Methods 34

2.1 Materials 34

2.1.1 Chemicals 34

2.1.2 Antibodies 36

2.1.3 Devices and Equipment 37

2.1.4 Solutions and Buffers 37

2.1.5 Laboratory Equipment 39
2.1.6 Software and Analysis 40
2.1.7 Patient Samples 40
2.2 Methods 41
2.2.1 Sample generation and processing 41
2.2.2 Histology 42
2.2.3 Microscopy and Image Analysis 47
2.2.4 Raman Imaging 47
2.2.5 Analysis of Spectral Data 47
2.2.6 True Component Analysis (TCA) 48
2.2.7 Principal Component Analysis (PCA) 48
3 Results 50
3.1 Identification of endometriosis by standard pathologic staining 50
3.2 Movat Pentachrome 53
3.3 Distribution Pattern of Elastic Fibers in KO and DI 55
3.4 Collagen Fiber Distribution and Content in KO and DI 56
3.5 Quantification of Collagen Fibers 57
3.6 Heterogenous Phenotype of Endometrial Foci 60
3.7 Identification of the Prominent Tissue Components with TCA 61
3.7.1 Nuclei 64
3.7.2 Epithelial Cells with Cell Organelles other Than Nucleus 64
3.7.3 Lipids 65
3.7.4 Collagen fibers 66
3.7.5 Elastic fibers 68
3.8 PCA of KO and DI of all Components 69
3.8.1 Nuclei 69
3.8.2 Epithelial Cells 70
3.8.3 Lipids 71
3.8.4 Collagen 74
4 Discussion 78
4.1 Raman Imaging as a Complementary Technique for Histopathology 78
4.2 Advantages of RMS over Conventional Histology 78

4.2.1 Insights at the Molecular Level 78
4.2.2 Enhanced Diagnostic Accuracy 79
4.2.3 Limitations of Raman Spectroscopy 80
4.2.4 Comparison with Classic Histology 80
4.3 Future Directions 81
4.4 Endometriosis Is Associated with Altered (fibrotic) Collagen Fibers 82
4.5 Altered Lipid Composition in Endometriotic Glands 92
4.6 Distinct Composition of Epithelial Cells in KO and DI Samples 99
4.7 Nuclear Changes in Endometriotic Glands 102
4.8 Limitations of the Present Study 102
4.8.1 Number of Included Samples 102
4.8.2 Raman Artifacts 104
5 Conclusion and Outlook 106
6 Supplementary 109
7 Deutsche Zusammenfassung 112
8 Erklärung zum Eigenanteil 132
9 Veröffentlichungen 133
10 Danksagung 134

List of Figures

Figure 1 Macroscopic and microscopic visualization of the uterus 12
Figure 2 Overview of physiological changes during the menstrual cycle 14
Figure 3 Visual Overview of Endometriosis types based on location 17
Figure 4 Revised American Society for Reproductive Medicine (r-ASRM) scoring system 19
Figure 5 #ENZIAN score for the classification of endometriosis 20
Figure 6 Laparoscopic apperance of diverse endometriosis lesions 27
Figure 7 The Jabłoński diagram illustrating elastic and inelastic scattering 30
Figure 8 True Component Analysis 48
Figure 9 Standard pathologic staining methods to diagnose endometriosis. 50
Figure 10 Schematic representation of glandular organization in the endometrium 51
Figure 11 General overview of the tissue composition with Movat Pentachrome 53
Figure 12 Distribution pattern of elastic fibers in KO and DI 55
Figure 13 Histologic visualization of collagen fibers 56
Figure 14 Quantification of collagen fibers using PSR and Fast Green stain ... 58
Figure 15 IHC characterization of endometriosis 60
Figure 16 TCA of eutopic and ectopic endometrial glands 62
Figure 17 PCA of Epithelial cells PC-5 70
Figure 18 PCA of Lipids PC-2 71
Figure 19 PCA of Lipids PC-7 73
Figure 20 PCA of Collagen PC-4 74
Figure 21 PCA of Collagen PC-7 76
Figure 22 Score values of nuclei PC-1 – PC-7 109
Figure 23 PCA of Nuclei PC-1 109
Figure 24 PCA of Nuclei PC-3 110
Figure 25 Quantification of collagen fibers according to assigned hues using PSR stain 111

List of Tables

Table 1 All used chemicals in alphabetical order. 36
Table 2 All used antibodies in alphabetical order. 37
Table 3 All used devices, in alphabetical order. 37
Table 4 Recipes for all used solutions in alphabetical order 39
Table 5 Used equipment in alphabetical order. 40
Table 6 Used software for measurements and analyses. 40
Table 7 Russell-Movat Pentachrome staining protocol for cryosections. 44
Table 8 The coloring pattern according to the Russell-Movat Pentachrome technique 45
Table 9 Characteristic bands and peaks for Nuclei 64
Table 10 Characteristic bands and peaks for cell organelles and cytoplasm of the epithelial cells 65
Table 11 Characteristic bands and peaks for lipids 66
Table 12 Characteristic bands and peaks for collagen fibers 67
Table 13 Characteristic bands and peaks for elastic fibers 68
Table 14 Loadings of EC PC-5 71
Table 15 Loadings of Lipids PC-2 72
Table 16 Loadings of Lipids PC-7 74
Table 17 Loadings of Collagen PC-4 75
Table 18 Loadings of Collagen PC-7 77
Table 19 Loadings of Nuclei PC1 and PC-3 110

List of Acronyms and Abbreviations

AA-M	amino acids with methyl groups in the side chains
anti-COL I	anti-Collagen type I
anti-COL III	anti-Collagen type III
anti-PRL	anti-Perlecan
BMs	Basement membranes
β	Bending
β_{ip}	in-plane bending
CCD	Charge-coupled Device
COL I	Collagen type I
COL III	Collagen type III
COL IV	Collagen type IV
DNA	Deoxyribonucleic acid
$DPBS^{-}$	Dulbecco's phosphate buffered saline
DI	Endometriotic glands
DIE	Deep infiltrating endometriosis
δ	Deformation
δ_{as}	Asymmetric deformation
δ_{ip}	In-plane deformation
#ENZIAN	Revised ENZIAN classification
EC	Epithelial cell
ECM	Extracellular matrix
EFI	Endometriosis Fertility Index
EKU	Eberhard-Karls-Universität Tübingen

ER	Endoplasmic reticulum
ESGE	Gynaecological Endoscopy
ESHRE	European Society of Human Reproduction and Embryology
FA	Fatty acid
FB	Bladder
FFA	Free fatty acid
FI	Intestine, excluding the rectum/sigmoid colon
FSH	Follicle stimulating hormone
FU	Ureter
GAGs	Glycosaminoglycans
GnRH	Gonadotropin-releasing hormone
HDL	High-density lipoprotein
HE	Hematoxylin-eosin
HvG	Hematoxylin and van Gieson stain
IHC	Immunohistochemistry
KO	Endometrial glands
LH	Luteinizing hormone
LDL	Low-density lipoprotein
LIS	Ligamentum sacrouterinum
m	Medium
MA	Myristic acid
MIT	Mitochondria
miRNA	MicroRNA

MRI	Magnetic resonance imaging
MPS	Mucopolysaccharides
(N/R)	Nuclear-to-Cytoplasmic Ratio
ω	Wagging
PC	Phosphatidylcholine
PCA	Principal Component Analysis
PFA	Paraformaldehyde
PI	Phosphatidylinositol
PRL	Perlecan
PS	Phosphatidylserine
PSR	Picrosirius Red
PUFA	Polyunsaturated fatty acids
r-ASRM	Revised American Society for Reproductive Medicine
RNA	Ribonucleic acid
rRNA	Ribosomal RNA
ROI	Region of interest
RMS	Raman Microspectroscopy
s	Strong
SRV	Septum rectovaginale
TAG	Triacylglycerides
TCA	True component analysis
TVS	Transvaginal ultrasound

τ	Twisting
VLDL	Very low-density lipoprotein
ν	Stretching
w	Weak
WES	World Endometriosis Society
γ_ω	Wagging coordinate
γ_τ	Twisting coordinate

1 Introduction

1.1 The Human Uterus

1.1.1 Macroscopic Anatomy of the Uterus

The uterus is a primary female reproductive organ located in the lesser pelvis, between the urinary bladder and the rectum. It can be divided into two parts, the corpus, and the cervix. The rearmost part of the corpus is the fundus. The fallopian tubes emerge from the dorsolateral wall and branch out to the right and left. Their broadest segment, the ampulla, reaches the ovary [1]. The isthmus marks the transition zone from the corpus to the narrower cervix [1].

1.1.2 Microscopic Anatomy of the Uterus

The wall of the uterus is about 1.5-2 cm thick and consists of three layers. From the outside to the inside, the following layers can be distinguished: perimetrium, myometrium and endometrium [1].

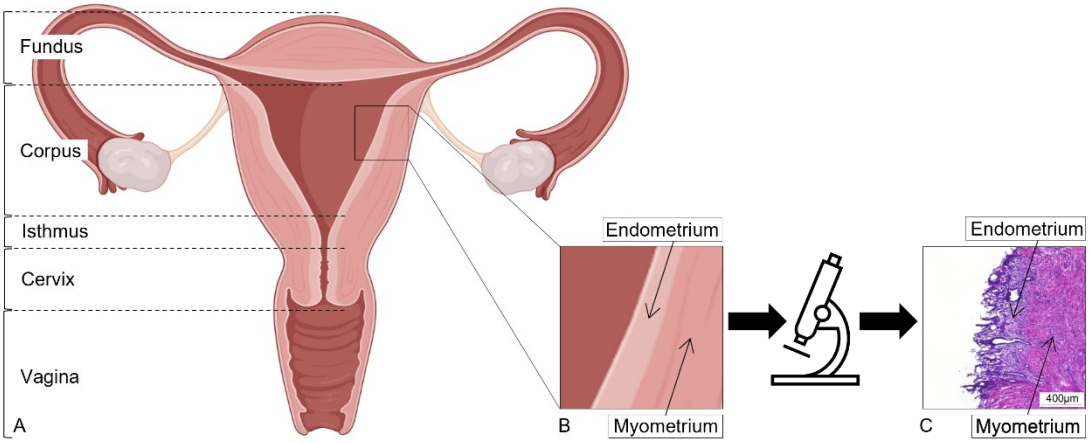

Figure 1 Macroscopic and microscopic visualization of the uterus

Anterior view of the uterus. (A), magnified part of the uterine wall (B), histologic hematoxylin-eosin (HE) stain of the endometrium and myometrium of the uterine wall (C). Created with BioRender.com

The perimetrium is the outermost layer of the uterus, consisting of a serosa with peritoneal epithelium and a thin layer of connective tissue. The serosa extends laterally to the *ligamentum latum*, which contains a network of smooth muscles, collagen fibers, elastic fibers, nerves and numerous blood and lymphatic vessels [1].

The myometrium (Fig. 1, Panel B, C) is the thickest layer of the uterus and comprises interwoven smooth muscle bundles. It plays a crucial role in the expulsive phase of childbirth [1]. It has four sublayers: *stratum subserosum*, *stratum supravasculosum*, *stratum vasculosum*, and *stratum submucosum sive subvasculare*, which is adjacent to the endometrium.

The endometrium, the innermost layer, is composed of surface epithelium, tubular glands, and a special connective tissue rich in cells and poor in fibers (Fig. 1, Panel B, C). It has two zones: the hormone-sensitive stratum functionale, which undergoes cyclical changes and is shed during menstruation, and the stratum basale, which remains unchanged during the menstrual cycle and serves to regenerate the stratum functionale. The endometrial glands experience pronounced changes during the menstrual cycle. The surface epithelium is composed of large epithelial cells (ECs) that produce protein-rich secretions, forming a protective coating and facilitating ion and fluid transport, supporting sperm survival and implantation of a fertilized egg [1].

1.1.3 Menstrual Cycle

In women of reproductive age, the endometrium undergoes monthly cyclic changes that coincide with ovarian changes. The initiation of menstruation marks the beginning of the menstrual cycle, which takes about 4 weeks [2]. The cycle is divided into a follicular phase (proliferative phase) and a subsequent luteal phase (secretory phase) of nearly equal length [2, 3]. Ovulation occurs between these two phases. The menstruation period is referred to as the luteal-follicular transition phase (desquamation phase) [3].

Hormonal fluctuations regulate these changes and prepare the uterus for potential pregnancy.

1.1.3.1 Physiological Role of Hormones

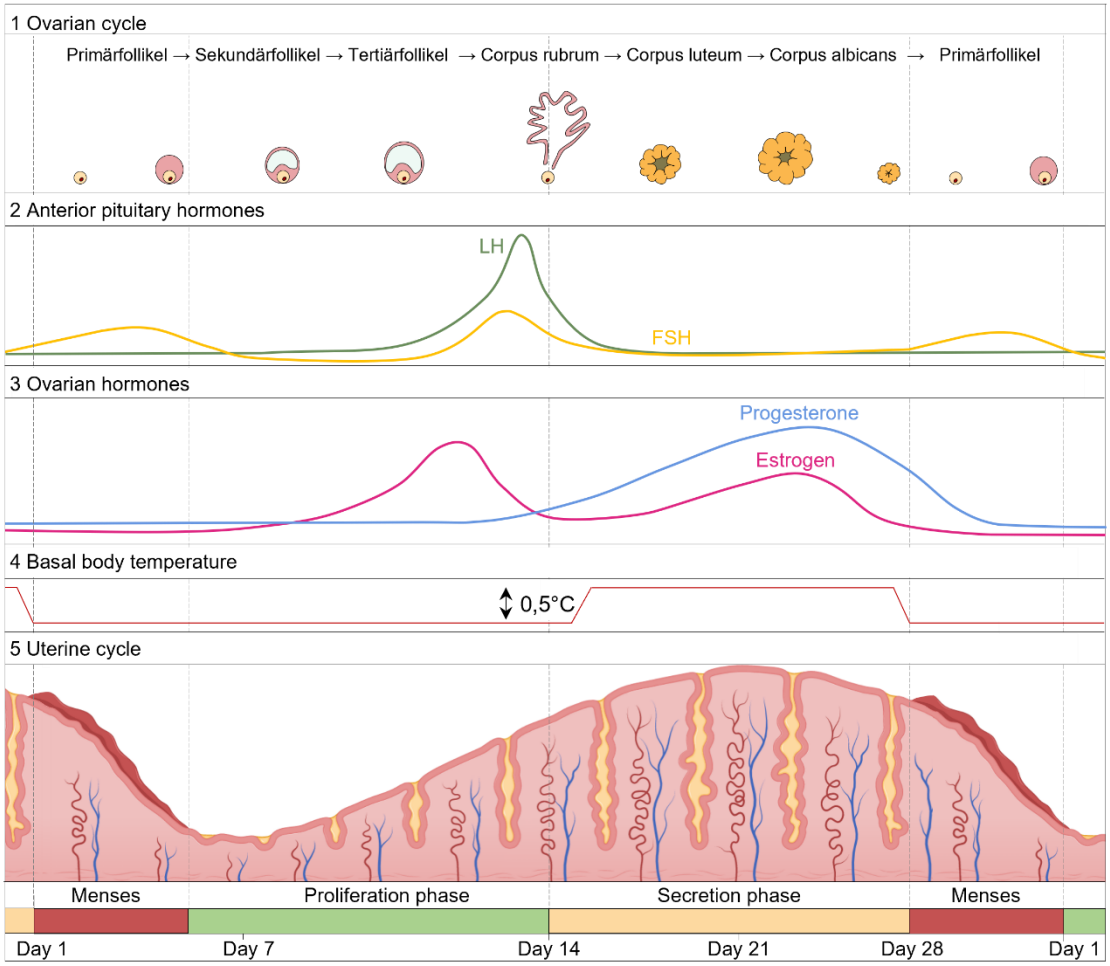

Figure 2 Overview of physiological changes during the menstrual cycle

The ovarian cycle with follicle maturation and atrophy (1), the rise and fall of the pituitary peptide hormones (2) and the ovarian steroid hormones (3), the incline of the basal body temperature in (4) and the endometrial formation and its shedding (5). Adapted from Reed et al. [2]. Created with BioRender.com

1.1.3.2 Desquamation Phase (1st–4th Day of the Cycle)

During this phase, estrogen and progesterone levels drop, causing detachment of the superficial endometrial layer and visible menstrual bleeding [3]. Prior to bleeding, intermittent contractions of the spiral arterioles occur, causing ischemia in the *stratum functionale*, resulting in tissue damage and the migration of immune cells into the stroma [3].

1.1.3.3 Proliferation Phase (5th–14th Day of the Cycle)

Elevated levels of FSH (Follicle-stimulating hormone) and LH (Luteinizing hormone) trigger the growth of ovarian follicles, with one becoming dominant. The dominant follicle produces estrogen, stimulating endometrial regeneration. Glandular proliferation begins and the cervical mucus becomes more receptive to sperm. Towards the end of the proliferative phase, a surge in LH triggers ovulation [3].

1.1.3.4 Ovulation (14th Day of the Cycle)

The LH peak triggers ovulation and basal temperature rise. Collagenases cause the follicle to burst, releasing the ovum; if fertilization does not occur within the next 24 hours, the egg degenerates. As the LH receptors increase on granulosa cells and FSH receptors decrease, luteinization (corpus luteum formation) begins [3]. Due to the increased production of progesterone and estrogen by the corpus luteum, the endometrium becomes thicker, more vascular, and gland-rich [3].

1.1.3.5 Secretory Phase (15th–28th Day of the Cycle):

Blood vessels develop between granulosa and theca cells (*corpus rubrum*). Luteal cells produce progesterone and estrogen. Endometrial glands become more secretory, preparing for potential implantation. Cervical mucus thickens to block further sperm entry [3].

1.2 Endometriosis

1.2.1 Definition, Epidemiology and Prevalence

Endometriosis is a chronic, benign, estrogen-dependent gynecological condition affecting mostly women of childbearing age, from the onset of menstruation to menopause [4]. The peak incidence is between the age of 25 and 35 [4]. While the exact prevalence is unknown, estimates suggest it affects approximately 6-10% of women worldwide [5, 6], with a high number of unreported cases [7]. Prevalence varies depending on the studied population and ranges from 2% to over 80% [8-10]. For example, endometriosis is diagnosed in 40–60% of women with dysmenorrhea, in 71–87% of those with chronic pelvic pain [9] and in about 20–30% of infertile women [9, 11].

1.2.2 Pathogenesis

Although endometriosis has been known for a long time, its pathogenesis has remained insufficiently understood [12-14]. The majority align with Sampson's theory of retrograde menstruation. According to this theory, during menstruation parts of the endometrial tissue are flushed backward through the fallopian tubes into the peritoneal cavity, where they implant on pelvis organs and develop into lesions [15].

Over time, many different theories have been proposed, rejected, and combined [14]. Underscoring that endometriosis is likely a multifactorial condition [7]. Recent research has also focused on identifying specific biomarkers in blood and urine, genetic testing, microRNAs (miRNAs), and "omics" approach in combination with medical artificial intelligence [16]. Dysbiosis of the gut microbiota may also contribute to the development and progression of endometriosis. This opens new avenues for both diagnostic and therapeutic strategies [16].

1.2.3 Symptoms and Clinical Presentation

The principal symptoms of endometriosis include lower abdominal pain, secondary dysmenorrhea, dyspareunia, dysuria, dyschezia [17], abnormal menstrual patterns, and impaired fertility [7, 13]. However, endometriosis can also be asymptomatic and may be discovered incidentally during infertility investigations [17]. The clinical presentation primarily depends on the location and extent of the disease [18].

1.2.4 Distribution of Endometriosis Locations

Endometriosis can manifest in various locations in the body, which has led to the development of classification systems. In clinical routine, endometriosis is classified by location into: e*ndometriosis genitalis interna* (Fig. 3, 1), *endometriosis genitalis externa* (Fig. 3, 2) and *endometriosis extragenitalis* (Fig. 3, 3) [19]. For precise classification, the use of scoring systems such as the revised American Society for Reproductive Medicine (r-ASRM) classification and/or the revised ENZIAN classification (#ENZIAN) (Chapter 3.2.5) is recommended [19].

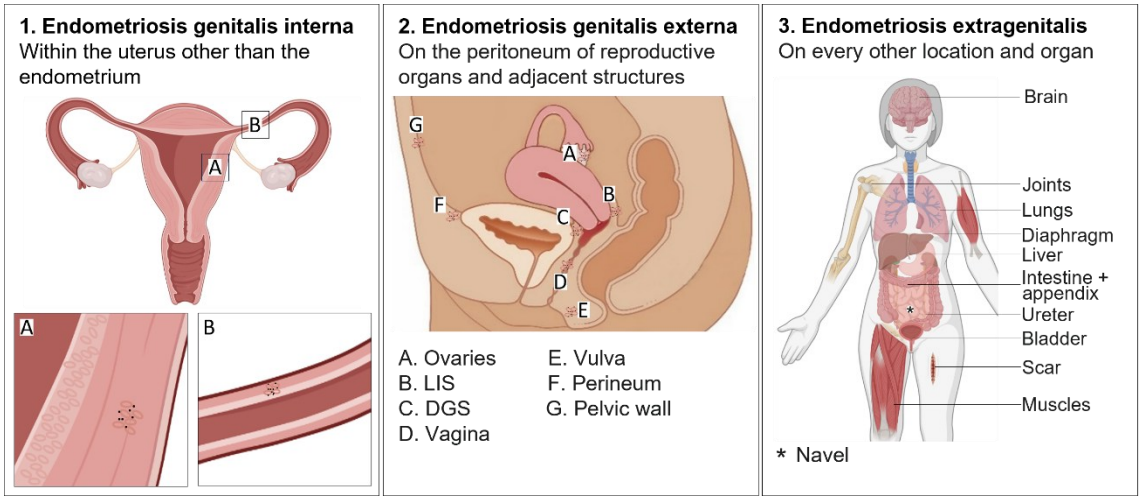

Figure 3 Visual Overview of Endometriosis Types based on Location

Endometriosis genitalis interna (1), including myometrial endometriosis (adenomyosis uteri) (A), and endometriosis within the Fallopian Tube (endometriosis tubae) (B). Endometriosis genitalis externa (2) showing potential locations (A-G) and endometriosis extragenitalis (3). Created with BioRender.com

The predominant form is endometriosis genitalis externa (Fig. 3, 2) , with foci primarily found in the pelvic peritoneum, ovaries, Ligamentum sacrouterinum (LIS), and Septum rectovaginale (SRV) [20]. In endometriosis genitalis interna (Fig. 3, 1), lesions are located within the uterus.

The exact prevalence of endometriosis genitalis interna is unknown. Lesions may be found in the myometrium (*adenomyosis uteri*) (Fig. 3, 1A), or in the Fallopian tube (*endometriosis tubae*) (Fig. 3, 1B), with the former being much more common [21]. Some studies report that around 20% of gynecological patients are affected by *adenomyosis uteri* [22].

Patients with symptomatic, confirmed extragenital endometriosis (Fig. 3, 3), account for 10–15% of all endometriosis cases, marking it as the least common type [23]. The most frequent form within this group is intestinal endometriosis, affecting about 5% of patients [23]. The most commonly involved intestinal segments are the rectosigmoid (51%), the appendix (15%), the small intestine (14%), the rectum (14%), and the cecum and colon (5%) [24]. Endometriotic lesions can also be found in scars from lower abdominal surgeries and in the

umbilical region [23]. The incidence of scar endometriosis following pelvic surgery is reported to be between 1–2% [23]. Extremely rare sites of endometriosis include the diaphragm [23, 25], the spleen, lungs, kidneys, brain or skeleton [20].

1.2.5 Classification according to r-ASRM and #ENZIAN

A precise and holistic classification of endometriosis is essential for assessing the extent, localization, and clinical-pathologic impacts. It also facilitates communication among surgeons, radiologists, and specialists in reproductive medicine, and enables the comparison of therapeutic strategies and outcomes [26].

The r-ASRM classification, updated in 1997, uses a scoring system to help assess the extent of endometriosis and the function of the reproductive organs during an invasive (i.e., surgical) procedure [26, 27]. It is currently the most globally accepted and used classification system in clinical practice and in the international literature [26].

In the r-ASRM classification, endometriotic foci on the peritoneum and ovaries as well as adhesions that partially obscure pelvic anatomy are the principal criteria used to assess disease severity. Points are awarded according to lesion size, location, and the extent of adhesions, resulting in four severity stages. Stage I (minimal), 1–5 points – Stage II (mild), 6–15 points – Stage III (moderate), 16–40 points – Stage IV (severe), >40 points (Fig. 4) [28].

Limitations of the r-ASRM score are that the stages (I-IV) do not convey the morphological complexity and extent of endometriosis. Its reproducibility is particularly limited when lesions involve the ovaries or the posterior cul-de-sac [29]. Additionally, deep infiltrating lesions, pain [30] and infertility [31] are not adequately considered. These shortcomings led to the introduction of the Endometriosis Fertility Index (EFI) by Adamson and Pasta et al. [32], which complements the r-ASRM system by providing prognostic information on the pregnancy rates in affected patients [32].

AMERICAN SOCIETY FOR REPRODUCTIVE MEDICINE
REVISED CLASSIFICATION OF ENDOMETRIOSIS

Patient's Name _____ Date _____

Stage I (Minimal) - 1-5
Stage II (Mild) - 6-15
Stage III (Moderate) - 16-40
Stage IV (Severe) - > 40
Total _____

Laparoscopy _____ Laparotomy _____ Photography _____
Recommended Treatment _____

Prognosis _____

PERITONEUM	ENDOMETRIOSIS	< 1cm	1-3cm	> 3cm
	Superficial	1	2	4
	Deep	2	4	6
OVARY	R Superficial	1	2	4
	Deep	4	16	20
	L Superficial	1	2	4
	Deep	4	16	20
	POSTERIOR CULDESAC OBLITERATION	Partial		Complete
		4		40
OVARY	ADHESIONS	< 1/3 Enclosure	1/3-2/3 Enclosure	> 2/3 Enclosure
	R Filmy	1	2	4
	Dense	4	8	16
	L Filmy	1	2	4
	Dense	4	8	16
TUBE	R Filmy	1	2	4
	Dense	4*	8*	16
	L Filmy	1	2	4
	Dense	4*	8*	16

*If the fimbriated end of the fallopian tube is completely enclosed, change the point assignment to 16.
Denote appearance of superficial implant types as red [(R), red, red-pink, flamelike, vesicular blobs, clear vesicles], white [(w), opacifications, peritoneal defects, yellow-brown], or black [(B) black, hemosiderin deposits, blue]. Denote percent of total described as R____%, W___% and B___%. Total should equal 100%.

Additional Endometriosis: _____

Associated Pathology: _____

To Be Used with Normal Tubes and Ovaries

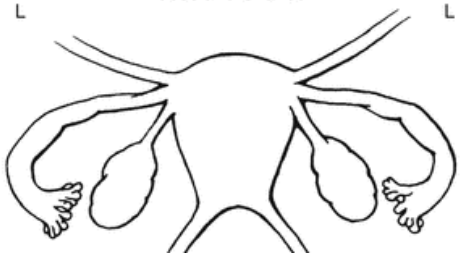

To Be Used with Abnormal Tubes and/or Ovaries

Figure 4 Revised American Society for Reproductive Medicine (r-ASRM) Scoring System

Scoring system for endometriosis affecting the peritoneum and the ovaries, with points assigned for extent and location. The total score reflects disease severity [33].

In 2021, the “Stiftung Endometriose-Forschung” (SEF) introduced the #ENZIAN classification, enhancing the assessment of DIE, by incorporating ovarian (Fig. 5 O) and peritoneal (Fig. 5 P) endometriosis and adnexal adhesions (Fig. 5 T) [26]. This classification is based on the Classification of Malignant Tumors (TNM) classification system [34]. It divides DIE into three main compartments: compartment A (SRV and vagina), B (LIS and pelvic sidewalls), and C (rectum and sigmoid colon) [35] (Fig. 5). Additional subcategories of DIE are FA (adenomyosis), FB (bladder), FI (intestine, excluding the rectum/sigmoid colon), and FU (ureter) (Fig. 5). Only the largest focus in one compartment is classified. The depth of invasion is categorized into three grades: < 1 cm (grade 1), 1–3 cm (grade 2), and > 3 cm (grade 3) [28, 35]. The #ENZIAN classification also allows for documentation of deep infiltrations outside the pelvic region and organ involvement, using special abbreviations to determine the exact location of the lesion.

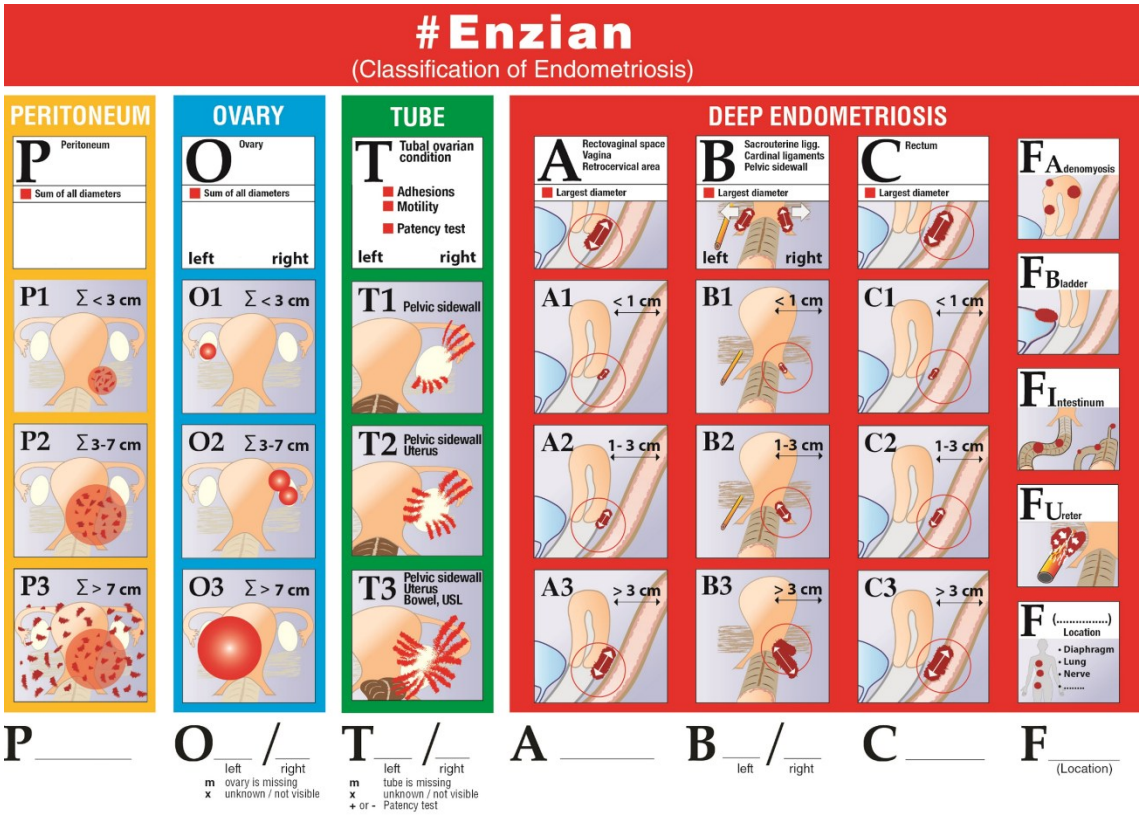

Figure 5 #ENZIAN Score for the Classification of Endometriosis

Overview of the #ENZIAN classification with detailed information on affected organ systems and compartments [36]

The #ENZIAN's stage categorization aligns with the r-ASRM classification and the recommendations of the European Society of Gynaecological Endoscopy (ESGE), the European Society of Human Reproduction and Embryology (ESHRE), and the World Endometriosis Society (WES), offering a logical and user-friendly system [26]. The aim was to standardize endometriosis classification across both pre-invasive (transvaginal ultrasound (TVS), magnetic resonance imaging (MRI)) and invasive methods [26]. Future studies are necessary to confirm the clinical validity, accuracy, and reproducibility of the #ENZIAN classification [26].

Compared to the r-ASRM score, the #ENZIAN classification offers a better assessment of the retroperitoneal structures and a detailed description of the extent of DIE [26] with high sensitivity and specificity [28]. Furthermore, this classification allows additional factors to be taken into account, such as the expected duration of surgery [37]. The main problem with the #ENZIAN score is its limited international acceptance; it is still mainly used in German-speaking countries. Despite the simplification of the scoring system, it is still perceived as more complex than the r-ASRM score [28].

1.2.6 Therapy and Prognosis

The treatment of endometriosis is a major challenge for clinicians and researchers. Both surgical and hormonal treatment options have been discussed. Neither approach, nor a combination of the two, seems to adequately address the symptoms [38]. Bohn et al. discussed the different treatment approaches for endometriosis. These include the combination, escalation of drugs prior to surgery as opposed to immediate surgical procedures [39]. Postponing surgery in cases where the pain does not respond to more than three medications could lead to a deterioration in quality of life and increased costs [39]. A mix of pharmacological, surgical, psychotherapeutic, and alternative treatments might enhance the quality of life for women living with endometriosis [40]. Regular follow-up and ongoing management are often necessary to monitor the condition and adjust treatment as needed. While the risk of cancer stemming from endometriosis is rare, meticulous surveillance is essential [40].

1.2.6.1 Non-surgical Treatment Approaches

The insights into the pathogenesis of endometriosis have significantly contributed to the development of effective pharmacological therapies [38]. First-line treatment typically includes combined oral contraceptives, which are used for both pain relief and suppression of further growth of microscopic or residual endometriosis after surgery [40]. The therapeutic effect is achieved by reducing local and systemic hormone production and inflammation [40].

Gonadotropin-releasing hormone (GnRH) agonists are commonly prescribed. They suppress ovarian estrogen production, leading to a hypoestrogenic state and amenorrhea which may result in regression of endometriotic implants [41]. Rafique et al. reported a reduction in pelvic pain and a prolonged symptom-free intervals of up to 12 months during GnRH therapy [41]. However, due to potential side effects, these drugs are only approved for a limited time. Concomitant therapy is recommended to provide symptom relief [41]. GnRH agonists suppress ovulation and are therefore suitable for women who are actively trying to conceive [41].

The pharmacological treatment of endometriosis is generally symptomatic rather than curative and often results in recurrence of symptoms when treatment is stopped [40, 42]. Alternative approaches like tetrahydrocannabinol and cannabidiol, acupuncture and physical therapy, have also shown promising results in relieving endometriosis-associated dysmenorrhea [40].

1.2.6.2 Surgical Treatment Approach

Laparoscopy is regarded as the gold standard for both definitive diagnosis and initial treatment of endometriosis [42]. Lesions can be removed by excision, vaporization, or ablation. The choice of technique depends on lesion location, patient's preference, available equipment, and expertise of the surgical team [38, 40, 42]. The aim is to remove the endometriosis lesions while preserving organs and fertility [38].

Studies have shown that laparoscopic removal provides symptomatic relief across all stages of disease severity [40]. Surgical intervention may be supported

by postoperative hormonal therapy to prevent regrowth of residual microscopic lesions [40].

Endometriosis, particularly the deep infiltrating type, may lead to anatomical distortion due to its vascular and infiltrative properties, which makes surgical dissection more challenging [40]. For successful treatment surgical expertise in retroperitoneal dissection is essential [40]. Preoperative hormonal suppression may reduce inflammation and vascularization. This creates a cleaner surgical field, allowing for a clearer view of the lesion and a more thorough excision [38, 40].

The type and extent of surgery should be tailored to each patient, taking into account factors such as age, desire for future fertility, family history, symptom severity, and intraoperative findings [40]. The ultimate goal is to comprehensively remove endometriotic tissue while preserving reproductive potential [38].

In summary, the management of endometriosis should be based on two core principles: removing ectopic endometrial tissue and preventing reimplantation until the immune status stabilizes [38]. This also includes the treatment of concomitant inflammatory and hormonal conditions [38]. It is important to note that neither pharmacological nor surgical measures can guarantee a complete cure [38]. It is crucial to incorporate individualized therapy into the perioperative strategy. [40]. Since endometriosis is complex and multifactorial, a multidisciplinary approach is required [40]. A combination of pharmacological, surgical, psychotherapeutic, and alternative therapies can improve quality of life of those affected [40]. However, symptoms may persist, and recurrence is possible. Kim et al. analyzed nine studies examining postoperative recurrence rates in abdominal wall and peritoneal endometriosis, published between 2003 and 2020 [43]. The analysis included a total of 218 patients [43]. The recurrence rates ranged from 0% and 15%, and the follow-up periods ranged from 1.1 to 235 months [43]. These findings highlight the importance of regular follow-up and personalized long-term management [43].

1.2.6.3 Physiologic Hormonal Changes influencing Endometriotic Lesions

Hormonal changes during pregnancy, particularly shifts in the estrogen-to-progesterone ratio, create favorable conditions for gestation [44]. Rising progesterone levels and declining estrogen suppress cell proliferation, which may result in stagnation or regression of endometriotic lesions, providing symptom relief [44]. However, decidualization-induced stromal hypertrophy has been linked to vascular wall nodules in endometriomas and deep infiltrating endometriosis (DIE) [44]. Studies have shown that 34–4.7% of endometriotic lesions regress during pregnancy, with 15–20% disappearing completely, while 8.8-39% of endometriomas may increase in size [44].

In postmenopausal women, declining estrogen levels and elevated FSH and LH levels often lead to symptom resolution, with only 2–5% of women remaining affected [45, 46]. It is unclear whether this reflects reactivation of pre-existing lesions, persistence, or de novo development [46]. An increased occurrence has been observed following hormone therapy or tamoxifen treatment [47].

Immediate evaluation is required for unexplained pelvic pain or abnormal uterine bleeding in postmenopausal women to rule out malignancy or the malignant transformation of endometriosis lesions [46, 47]. To optimize management and prevent malignant progression, surgical excision of all suspicious lesions is recommended [47].

1.2.7 Diagnosis

Endometriosis can potentially affect almost every organ in the body [40], and the associated symptoms and disease severity vary greatly among patients [48]. Misdiagnosis, trivialization of symptoms and the necessity of invasive procedures for definitive diagnosis are major factors contributing to delayed diagnosis, which may extend up to 10–12 years [4, 49, 50]. Fortunately, endometriosis is now often diagnosed at earlier stages [49, 51, 52], likely due to increased awareness among both physicians and patients [7].

1.2.8 Current Screening and Diagnostic Options

1.2.8.1 Medical History

The initial step in diagnosis is to gather a detailed medical history. During gynecological assessments, it is crucial to explore painful and chronic conditions [13], utilizing tools like the visual analogue scale for better pain assessment [13, 53]. Detailed questioning should cover symptoms such as dysmenorrhea, pain intensity, radiation, associated symptoms, aberrant menstruation patterns [54], and infertility, while also examining cyclic manifestations like shoulder [53], lower abdominal [54], leg (sacral plexus infiltration), and umbilical pain or bleeding [13], along with atypical symptoms like hemoptysis [55], catamenial pneumothorax [55], and recurrent headaches and migraines [13, 56, 57], potentially linked to endometriosis.

1.2.8.2 Physical Examination

A physical examination is a noninvasive, low-cost method to evaluate suspected endometriosis [53]. It may help identify affected areas by visual inspection or palpation, assessing pain distribution and evaluating organ mobility. It is especially valuable in the initial assessment of symptomatic patients [53].

However, its sensitivity and specificity vary depending on the form and localization of the endometriosis [58, 59]. Superficial lesions (e.g. vaginal or scar endometriosis) may be detected during inspection, whereas (recto)vaginal palpation may reveal painful indurations suggestive of deep pelvic endometriosis and bimanual palpation may indicate the presence of ovarian endometriomas [56]. The use of a speculum or colposcope enhances visibility of the posterior vaginal fornix and cervix [14].

Limitations include the varying experience of the examiner, patient discomfort and the unsuitability of bimanual examination for certain groups such as adolescents, non-sexually active individuals or those with a history of sexual trauma [53]. As there are no pathognomonic findings, physical examination mainly serves to support the diagnosis and rule out differential diagnoses, including endosalpingiosis, endocervicosis, Müllerianosis, reactive mesothelial hyperplasia, and malignancies [60, 61].

1.2.8.3 Advanced Non-invasive Diagnostics

The main non-invasive imaging modalities for endometriosis are TVS [54] and MRI [56]. Due to the heterogeneous manifestations of the disease, their diagnostic accuracy varies by lesion location. MRI is slightly more accurate than TVS in diagnosing adenomyosis [62, 63], particularly in the presence of other uterine pathologies such as leiomyomas [64, 65] or enlarged uteri (> 300 ml) [65]. However, the absence of standardized MRI criteria lead to inconsistent findings across studies [66].

Both TVS and MRI are effective in detecting endometriomas, which typically appear as homogeneous, anechoic cysts [56, 67]. Vercellini et al. reported no diagnostic advantage of MRI over TVS when assessing urinary tract and bladder involvement [56, 67, 68].

Sonography, including endorectal ultrasound, is well suited for detecting endometriosis in the SRV [56] and the LIS [56, 67]. Although an MRI can detect nodular endometriosis in the LIS, there is a risk of false positives due to misinterpretation of anatomy, artifacts, or postoperative changes [67].

Diagnosing peritoneal endometriosis remains particularly challenging, as lesions may be small, scattered, and often undetectable via imaging [13, 56]. Consequently, neither TVS nor MRI can definitely rule out Endometriosis genitalis externa or deep infiltrating endometriosis [13].

In general, the diagnostic accuracy of TVS strongly depends on the examiner's experience [65], whereas MRI provides more consistent and reproducible results – both in clinical practice and across research studies [66]. When non-invasive imaging is inconclusive, further diagnostic procedures, such as laparoscopy, are essential for accurate assessment and confirmation.

1.2.8.4 Advanced Invasive Diagnostics

Currently, diagnostic laparoscopy remains the most reliable method for diagnosing endometriosis. It enables the visualization of the abdominal cavity, revealing issues like peritoneal obstruction, adhesions, and defects [69]. Biopsies can be taken for histologic confirmation if needed [16]. The histologic diagnosis

of endometriosis is considered a confirmatory finding [67]. While histologic confirmation is considered definitive, achieving a diagnosis can be challenging [69] due to inconsistencies between macroscopic and histologic findings. Additionally, seemingly healthy areas can sometimes harbor endometriotic lesions [16]. Both diagnostic laparoscopy and biopsy are invasive procedures and therefore represent a major obstacle to the effective clinical management of endometriosis [16].

1.2.8.5 Laparoscopic Presentation of Endometriosis

Endometriosis exhibits a highly variable morphological appearance, with variations not only in location but also in appearance. The color spectrum of endometriotic lesions is particularly diverse (Fig. 6) [70, 71]. A typical finding includes livid, small nodular deposits on the ovaries and/or pelvic peritoneum [56]. The range of lesion color extends from blue/black [72] (Fig. 6 A) to brown [72], red (Fig. 6 B), white (Fig. 6 C) and even clear or translucent appearances [70, 72, 73] (Fig. 6 D). Pigmented lesions are generally considered typical, whereas non-pigmented lesions are regarded as atypical [56].

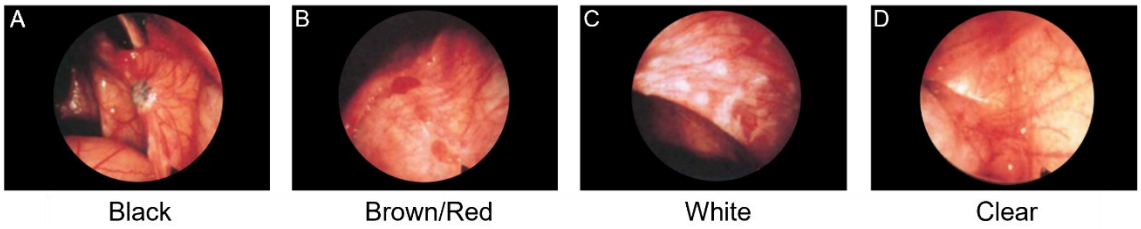

Figure 6 Laparoscopic apperance of diverse endometriosis lesions

Laparoscopic images displaying lesions of varying colors. Adapted according to [27]

Veil-like structures and cysts are classified as suspicious findings [56]. For a long time, the assumption prevailed that the colors of endometriotic lesions reflect different levels of disease activity. Red and non-pigmented [26] lesions were thought to represent active and highly vascularized implants [73, 74], whereas black lesions were considered less active [56] and white lesions were interpreted as fibrotic or inactive [70, 75].

Recent studies have challenged this concept, suggesting that lesion color does not necessarily reflect biological activity [70]. In particular, pigmented lesions

often present a discrepancy between their clinically suspicious appearance and a negative histologic result [56]. Instead, these studies suggest that the lesion color correlates with its age, glandular architecture, and glandular content [70]. Endometriosis remains a heterogeneous condition, and its macroscopic and microscopic appearance is often not specific enough for definitive diagnosis [56]. Therefore, the gold standard remains the histologic evaluation of suspicious lesions [56].

1.2.9 Subject of current research

In summary, while current imaging techniques are effective in detecting retroperitoneal endometriosis in the pelvis [76], they lack the spatial resolution to reliably identify small, superficial peritoneal and ovarian implants or adhesions [76, 77]. The clinical relevance of detecting early-stage lesions remains unclear, as not all small lesions inevitably progress to an invasive state [77]. It is hypothesized that the extent of invasion is primarily determined by local microenvironmental changes, such as interstitial hemorrhage, inflammation and subsequent colonization by endometriotic cells [19]. Thus, if endometriosis is suspected, initial drug treatment may be a more favorable initial approach [77].

Emerging postgenomic technologies and new serum and endometrial markers hold promise for future diagnostic advances [76]. Ongoing research explores candidate biomarkers in blood and biofluids, including serum, urine, saliva, and synovial fluid [78]. These biomarkers may not only aid in diagnosing or ruling out endometriosis but could also serve as tools for monitoring treatment response [79, 80]. The systematic review by Webster et al. examined liquid biopsies (serum, plasma, and urine) over a 25-year period with the aim of identifying a potential biomarker for endometriosis. Although numerous putative biomarkers were identified, none demonstrated sufficient clinical utility [79]. The authors concluded that biomarker panels, rather than individual markers, may offer better diagnostic performance [79].

Notarstefano et al. analyzed granulosa cells from patients with unilateral ovarian endometriosis using Raman Microspectroscopy (RMS). Their results suggested that endometriosis may affect the contralateral ovary as well, despite the absence

of visible lesions, highlighting the diagnostic potential of RMS for detecting subclinical or systemic effects [81].

Anastasiu et al. and Kiesel and Sourouni et al. have emphasized the value of integrating non-invasive techniques, including proteomics, genomics, and miRNA microarray technologies into the diagnostic workflow [16, 82]. These approaches may be further enhanced by incorporating artificial intelligence [16]. These methods have the potential to enhance the diagnostic capabilities for endometriosis when used in conjunction with RMS [82]. Additionally, Kiesel and Sourouni et al. underscored the significance of dysbiosis in the gut microbiota, which may be a pivotal factor in the pathogenesis and progression of endometriosis [16].

1.2.10 Endometriotic Tissue Characterization

Biopsies obtained during laparoscopic surgery are usually sent to the pathology department for histologic processing. To date, stained histopathology has been the gold standard for diagnosing disease, relying on experienced pathologists to assess subtle morphological features, making it a subjective and time-consuming process [83]. The histopathologic diagnosis of endometriosis is based on a combination of histologic and immunohistochemical staining (IHC). H&E staining is performed to assess the general tissue structures, while CD10-IHC staining specifically identifies the endometrial stroma, especially in smaller or atypical lesions [84].

1.3 Raman Microspectroscopy

Compared to other techniques, RMS provides rapid and direct insights into the molecular composition of tissues [85, 86] without the need for staining, thereby avoiding potential artefacts and interferences [83]. As a vibrational spectroscopic method, RMS gathers information about the molecular vibrations in a sample by detecting changes in the polarizability of the vibrating molecules [86]. This marker-free, non-contact, and non-destructive laser-based technique is used to analyze chemical bonds and molecular structures. RMS can be used to analyze biological samples [83, 85], enabling the detection of distinct spectral signals from proteins, nucleic acids, lipids, carbohydrates, and inorganic crystals [86, 87].

1.3.1 Basic Principles of Raman Microspectroscopy

The basic principle of RMS involves various interactions of light with molecules, such as absorption, transmission and, in rarer cases, scattering. Scattering occurs when a photon interacts with an electron [88], transferring energy that promotes the electron to a higher, virtual energy state [88] (Fig. 7). The electron subsequently relaxes back to its ground state, emitting a photon in the process [88]. The scattered light can then be detected and identified as either elastic scattering (Rayleigh) or inelastic scattering (Raman) (Fig. 7). RMS is based on the latter.

1.3.2 Inelastic Scattering – Raman Scattering

The Raman scattering can be divided into two categories based on the final vibrational level of the electron: Stokes and Anti-Stokes scattering [89] (Fig. 7).

Stokes shift occurs when the analyte molecule absorbs energy [90]. The emitted photon has a lower frequency than that of the incident photon [90] (Fig. 7). Anti-Stokes shift happens when the frequency of the emitted photon is higher than that one of the incident photon [91] (Fig. 7). This indicates that the electron is emitting energy during the scattering process [85, 90].

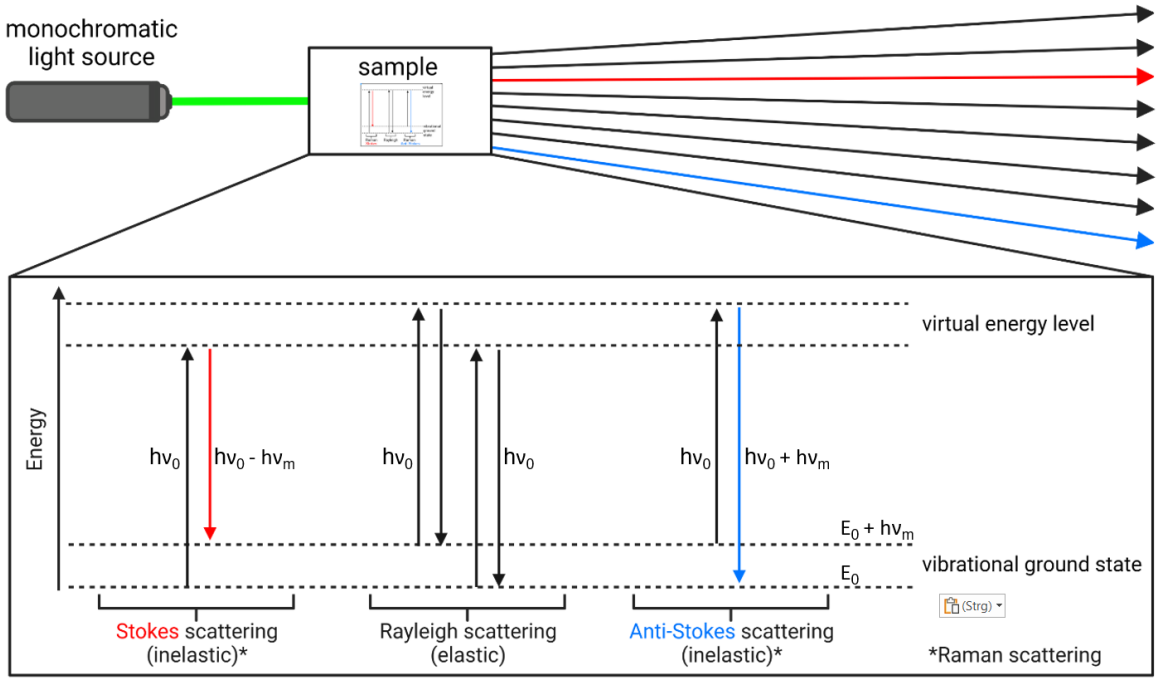

Figure 7 The Jabłoński diagram illustrating elastic and inelastic scattering

In elastic (Rayleigh) scattering, the incident photon and the re-emitted photon have the same frequency ($hv_0 = hv_0$). In inelastic (Stokes and anti-Stokes) scattering, the re-emitted photon has a different frequency to the incident photon ($hv_0 \neq hv_0$). Adapted from [92, 93]

Classical RMS is based on the measurement of Stokes scattering, which is more pronounced at room temperature [91] compared to Anti-Stokes processes [90] and typically has a stronger signal. In Anti-Stokes scattering the emitted photons have a higher energy/frequency, but lower intensity than the incident photons, making them more challenging to detect [92]. Combined analysis of both Stokes and anti-Stokes signals can provide more information about molecular vibrations in the sample and increase detection sensitivity [92].

The energy difference between incident and scattered Raman light corresponds to the frequency of the excited vibrational bond [91]. Each chemical bond in a molecule vibrates at a different frequency and produces an individual signal, resulting in an unique spectrum, also referred to as the "fingerprint" [89] of a vibration [91].

1.4 Prospects of RMS

RMS harbors considerable potential for future advances in various fields. It can measure significant biochemical changes in tissues [94], allowing for the detection of neoplastic changes before they become histopathologically visible [95, 96]. This could contribute to the surveillance of precancerous lesions and allow earlier intervention and more frequent follow-up of high-risk patients [97]. RMS improves biopsy accuracy in organs with precancerous lesions, reducing random biopsies and minimizing the risk of missing abnormal lesions [94]. Future in vivo measurements may use miniaturized needle probes in solid organs [94]. RMS also shows great potential for precise intraoperative margin analysis in solid tumors by providing detailed biochemical information with excellent diagnostic accuracy [98]. RMS could also contribute to the discovery of new biomarkers, the understanding of disease mechanisms and the development of improved treatments [99]. It holds promise for the future of clinical cancer nanomedicine [100]. It enables a rapid identification and characterization of biomolecules, body fluids, bioparticles (such as bacteria, yeast, viruses, and cells), and biological tissues. RMS can also contribute to solving issues related to infectious diseases

such as malaria [101], as well as metabolic diseases such as diabetes mellitus or atherosclerosis and neurodegenerative diseases, including Parkinson's and Alzheimer's disease [102]. In pharmaceutical development, RMS can be used for drug screening and quality control [103], improving personalized therapeutic strategies by identifying molecular biomarkers [104]. In materials science and nanotechnology, RMS supports the development of advanced materials and sustainable energy technologies [105]. RMS is also useful in the food industry, particularly for quality control during the hydrogenation of edible oils by enabling online remote control measurements of unsaturation and isomer formation [106].

1.5 Aim of the Study

Endometriosis is a gynecological disorder affecting 8–10% of women worldwide [5-7]. Definitive diagnosis requires laparoscopic surgery followed by histologic confirmation, making it an invasive and resource-intensive process [16, 67, 69]. Given the complex and multifactorial nature of endometriosis, neither pharmacological nor surgical treatment provides a definitive cure. Consequently, long-term, multidisciplinary care and continuous monitoring remain essential [38, 40].

Recent studies have demonstrated the diagnostic potential of RMS in both serum- and tissue-based applications [107]. Parlatan et al. applied RMS to blood serum and distinguished endometriosis patients from healthy controls with 100% sensitivity and specificity [107]. However, tissue-based RMS studies remain limited. Lieber et al. included endometriotic tissue in their study on ovarian pathologies and showed that RMS could differentiate low-risk tissues (normal and endometriotic) from high-risk tissues (benign-cystic and cancerous) with 93.3% sensitivity and 86.7% specificity, albeit without histologic confirmation [108]. Patel et al. used RMS to differentiate uterine tissue compartments and to distinguish cancerous from non-cancerous areas [109]. Notarstefano et al. detected metabolic alterations in granulosa cells from patients with ovarian endometriosis using RMS [81].

In this study, histologically confirmed tissue samples of eutopic endometrium and endometriotic lesions were analyzed using RMS. Glandular and stromal compartments were identified through histologic staining and selectively examined to create detailed spectroscopic fingerprints. The primary objective was to identify distinct spectral and biochemical differences between the two tissue types. Furthermore, we aimed to evaluate whether RMS is suitable as a minimally invasive, real-time, intraoperative diagnostic tool capable of differentiating endometriotic tissue without the need for biopsy.

2 Material and Methods

2.1 Materials

2.1.1 Chemicals

materials	Catalogue-/Lot number	manufacturer
Acid Fuchsin	1B-525 10G Lot# 331830	Waldeck/Diagonal
Alcian Blue 8GX	5500 10G Lot# 172430	Sigma Aldrich (Fluka)
bovine serum albumin (BSA), 30% sterile filtered	A9576 50mL Lot# SLCC6663	Sigma Aldrich
Brilliant-Crocein R	1B109 25G Lot# 201630	Waldeck/Chroma
cold water fish skin gelatin	G7765 250ML Lot# SLBD9897	Sigma Aldrich
Dulbecco's Phosphate Buffered Saline (DPBS^{-})	14190-094 500ML Lot# 1892388; 1989155	Gibco® life technologies™
Eosin G solution, 1% aqueous	3137.2 1L Lot#8782-17	Carl Roth GmbH + Co. KG
ethanol absolute (p.a.)	A1613 2.5L Lot# 8F014436; 8Q013199	AppliChem
Faramount Aqueous Mounting Medium	S3025 Lot# 10103297	Dako
Fast Green FCF	F7252 5G Lot# MKBR8790V	Sigma Aldrich
glacial acetic acid	1.000.63.1011 1L Lot# K38877863825	Merck
Hemalaun, Mayer’s	T865.2 Lot# 310299548	Carl Roth GmbH + Co. KG

Hematoxylin	5B-535 100G Lot# 342132	Waldeck/Chroma
Hematoxylin QS	H-3404 Lot# X0916	Vector Laboratories, Inc.
Hydrochloric Acid 37% p.a.	4625.1 Lot# 388100009	Carl Roth
Hydrogen peroxide 30%	95321 100ML Lot# BCBX6541	Sigma Aldrich
Hydrophobic barrier PapPen (ImmEdge)	H-4000 Lot# ZH0413	Vector Laboratories, Inc.
ImmPact™ DAB kit	SK-4105	Vector Laboratories, Inc.
ImmPACT™ VIP kit	SK-4605 Lot# ZG0312	Vector Laboratories, Inc.
ImmPress™ Kit, mouse IgG	MP7402 Lot# ZE0912	Vector Laboratories, Inc.
ImmPress™ Kit, rabbit IgG	MP7401 Lot# ZB0515	Vector Laboratories, Inc.
Iodine	I/0500/48 Lot# 1288322	Fisher Scietific
Iron-(III)-chloride	I/1035/53 Lot# 1003024	Fisher Scientific
Isomount® 2000	5547535 Lot#SM00002777	Labonord
isopropanol p.a.	33539 2.5L Lot# I354S	Riedel-de-Haen/Honeywell
methanol (AnalaR Normapur)	20847307 1.5L Lot# I291IS	VWR
normal goat serum	S1000 20ML Lot# ZG1028	Vector Laboratories, Inc.
Paraformaldehyde (PFA)	16005 1KG	Sigma Aldrich

	Lot# STBJ5933	
Phosphotungstic Acid	2635.3 250G Lot# 468277711	Carl Roth
Picric Acid (1.3% H_2O saturated)	P6744 1GA Lot# BCBP0720V	Sigma Aldrich
Potassium iodide puriss p.a.	60400 100G Lot# 126086440306005	Fluka
Resorcin-Fuchsin solution, Weigert's	X877, 1L	Carl Roth
Saffron du Gâtinais	5A-394 Lot# 302030	Waldeck/Diagonal
Sirius Red F3B (c.I. 35782) „Direct Red 80"	365548 5G Lot# MKBP5683V	Sigma Aldrich
sodium thiosulfate	S/7250 500G Lot#1012285	Fisher Scentific
TissueTek® O.C.T.	125mL E5348 Lot# 1626101005	Sakura Finetek Germany GmbH
Triton X-100	T8787 50ML Lot# MKBG6744V	Sigma Aldrich
Tween 20	P1379 100ML Lot# SZBA3190V	Sigma Aldrich
Vector® VIP Peroxidase Substrate Kit	SK-4600 Lot# ZF0517	Vector Laboratories, Inc.

Table 1 *All used chemicals in alphabetical order.*

2.1.2 Antibodies

antibody	Catalogue/LOT number	manufacturer	dilution
anti-CD10, mAb mouse IgG1	NCL-L-CD10-270 Lot# 6063359, 31mg/L	Leica Novocastra	1:100
anti-collagen I, polyclonal rabbit IgG	R1038 Lot# A1401438H	Acris	1:75

anti-collagen III, polyclonal rabbit IgG	R1040 Lot# A1200974	Acris	1:75
anti-perlecan, polyclonal rabbit IgG	sc-25848 Lot# C2309	Santa Cruz Biotechnology	1:100

Table 2 *All used antibodies in alphabetical order.*

2.1.3 Devices and Equipment

device	Type, S/N	producer
Cryotome	Microtom HM 560	Thermo Scientific
Fine scale balance	M-Power	Satorius
Freezer -20°C	Froster Labo 730	Kirsch
Freezer -80°C	Hera Freezer HFU700TV60	Thermo Scientific
Observer microscope	Discovery.V12 CL 1500 ECO	Carl Zeiss
Raman microspectrometer	alpha300 R Confocal Raman Imaging Microscope	WITec GmbH
Refrigerator 4°C	FKS 3600	Liebherr
Refrigerator with freezer	Comfort	Liebherr

Table 3 *All used devices, in alphabetical order.*

2.1.4 Solutions and Buffers

Solution	Contained solutions
0.5% HCl-Ethanol	mix 5mL of 37% hydrochloric acid (HCl) with 995mL of 70% ethanol
1% acetic acid solution	1mL of glacial acetic acid in 100mL of distilled water
3% acetic acid solution	3mL of glacial acetic acid in 100mL of distilled water
Acidified distilled water	100µL of glacial acetic acid in 100mL of distilled water
1% Alcian Blue 8GX solution	1 g Alcianblau 8GX (C.I. 74240) in 100 mL acetic acid (3%)
Brilliant-Crocein–Acid Fuchsin solution	Mix 8 parts of Stock Solution A with 2 parts of Stock Solution B.

	Stock Solution A (Brilliant Crocein R Solution): Dissolve 0.2g of Brilliant Crocein R (C.I. 27290) in 200mL of 3% acetic acid. **Stock Solution B** (Acid Fuchsin Solution): Dissolve 0.2g of Acid Fuchsin (C.I. 42685) in 200mL of 3% acetic acid.
Dilution buffer	8% $DPBS^-$ 1% bovine serum albumin (BSA) 0.1% Triton X-100 0.1% cold water fish skin gelatin 0.05% Tween 20
Ethanol solutions: 96%, 80%, 70%, 50%	100% ethanol mixed v/v with distilled water
2% ferric chloride solution	Dissolve 2g Iron-(III)-chloride in 100mL distilled water
10% ferric chloride solution	Dissolve 10g Iron (III)-chloride in 100mL distilled water
Goat block buffer	98% dilution buffer 2% goat serum
Iodine/potassium iodide solution	Dissolve 1g Potassium iodide in 5mL of distilled water and add 2g Iodine, let it stir until dissolved and add 95mL distilled water
Iron Hematoxylin Solution	Dissolve 10g hematoxylin in 100mL of ethanol p.a.
4% PFA	4g PFA 100 mL $DPBS^-$ heated up to until solution turns clear
5% Phosphotungstic Acid solution	Dissolve 5g of Phosphotungstic Acid in 100mL of distilled water.
Picrosirius Red	0.5 g Sirius Red F3B dissolved in 500 mL saturated aqueous Picric Acid (Picric Acid (1.3% H_2O saturated)). Stirred with magnetic stirrer, filtered to

	remove undissolved particles, and stored light-protected at room temperature.
5% sodium thiosulfate solution	Dissolve 5g of sodium thiosulfate in 100mL of distilled water
Van Gieson's solution	Add 5 mL of 1% aqueous acid fuchsin solution slowly to 100 mL of filtered saturated aqueous picric acid solution, mix thoroughly.
Verhoeff's staining solution	50 mL 10% alcoholic Hematoxylin solution 50 mL ethanol p.a. 50 ML 10% aqueous ferric chloride solution 50 mL iodine/potassium iodide solution
Washing Buffer	99.95 % $DPBS^-$ 0.05 % Tween 20
Weigert's A	dissolve 1g of Hematoxylin in 100mL of 96% ethanol
Weigert's B	dissolve 1.16g of $FeCl_3$ in 99mL of distilled water, add 0.68mL of 37% HCl (fuming)

Table 4 *Recipes for all used solutions in alphabetical order*

2.1.5 Laboratory Equipment

name	order number	manufacturer
Cover slips	01-2550/1	Langenbrinck GmbH
Disposable surgical scalpel	BA221; Lot: 4508952742	B-Braun; Aesculap AG
Disposable plastic tweezers	H7 301; Lot: 20170316	MediWare
Falcon® 50 mL High Clarity PP Centrifuge Tube, Conical Bottom, Sterile	352070	Corning Life Sciences
Glass cuvettes	23318005	DWK
Peel-A-Way Embedding Mold	189985	Polysciences, Inc.

Microscope slides	03-0060; Lot: 070816	R. Langenbrick
Pasteur pipettes (plastic)	ST2600111	neoLab
Petri dishes	633102	Greiner GmbH

Table 5 *Used equipment in alphabetical order.*

2.1.6 Software and Analysis

type	product name	manufacturer
Analysis software	TheUnscrambler X 10.5	Camo
Data analysis and processing	Microsoft Excel 365	Microsoft Corporation (Redmond, WA, USA)
Image editing program	ImageJ	Wayne Rasband (NIH)
Programming software	MatLab R2018a	The MathWorks
Microscopy software	ZEN 3.0 (blue edition)	Carl Zeiss
Raman analysis software	Project FIVE 5.2	WiTec
Raman measuring software	Control FIVE 5.0	WiTec
Statistic software	GraphPad Prism 6.0	GraphPad software
Text processing	Microsoft Word 365	Microsoft Corporation (Redmond, WA, USA)
Establishing connection from distance	TeamViewer14	TeamViewer (Göppingen, GER)

Table 6 *Used software for measurements and analyses*

2.1.7 Patient Samples

Two groups of patients were considered in this study. The control group consisted of patients who underwent total hysterectomy. Indications for hysterectomy included two patients with endometrial hyperplasia and consecutive hyper-, meno- , and dysmenorrhea, one patient with uterus myomatosus, one patient with PAP IIa with large portioectopy and contact bleeding. The study group consisted of women who had endometriosis lesions surgically removed from three different

sites in the pelvis. Only patients with endometriosis lesions at the LIS, the SRV, and in the *excavatio rectouterina*, the so-called Douglas pouch (DGS), were included.

At the time of collection, all patients were in the same menstrual phase, namely the proliferative phase. The average age was 44 years (39 to 48 years). In the main study, the average age was 36.75 years (31 to 41 years). The reasons for herd rehabilitation varied. However, dysmenorrhea was the predominant factor in all patients studied. All patients had different #ENZIAN and rASRM scores. Patients who were in a different menstrual cycle phase, postmenopausal or under the influence of contraceptives were excluded from the study. Both endometriosis tissue and endometrium were obtained from the Women's Hospital, Department of Women's Health, Tübingen.

2.1.7.1 Ethics application

The Ethics Committee of the Medical Faculty of the Eberhard Karls University Tübingen approved the scientific use of the tissue of the Medical Faculty of the Eberhard-Karls-University Tübingen (152/2018 BO2, approval: 29.03.2018).

2.2 Methods

2.2.1 Sample generation and processing

Endometriotic foci were removed via laparoscopic surgery. Endometrial control tissue samples were obtained either through laparoscopic hysterectomy or transvaginal hysterectomy. In laparoscopic hysterectomy, the uterus is morcellated into smaller fragments and extracted through one of the abdominal trocar sites. In transvaginal hysterectomy, access to the cervix and uterus is gained through an incision in the posterior vaginal fornix. After careful dissection and detachment of the uterus from surrounding structures, it is removed through the vaginal canal. The vaginal vault is then closed with absorbable sutures.

The endometrium was collected from the morcellated uterine tissue. For transport, both endometriotic and endometrial tissue samples were placed in pre-chilled $DPBS^{-}$. In the laboratory, the samples were embedded in plastic molds and covered with cryoprotectant medium for further processing. The specimens

were incubated at room temperature for approximately 6–8 hours to allow for water displacement and thorough infiltration with glycol-containing cryoprotectant prior to freezing at -80°C. Before sectioning, the frozen tissue blocks were equilibrated at -20°C for 10–15 minutes. Cryosections of 10 µm thickness were then cut using the Cryotome and mounted onto negatively charged microscope slides, which were subsequently stored at -20°C until further use.

2.2.2 Histology

Several histologic stains were performed and subsequently reviewed by the pathology institute to ensure and confirm the presence of endometriosis. These staining techniques were essential for a comprehensive assessment of the tissue composition in both the endometrium and the endometriosis samples and for validating the components identified through True Component Analysis.

All staining procedures were performed on 10 µm thick cryosections and followed a standardized preprocessing protocol. Briefly, cryosections were washed twice for 10 minutes in $DPBS^-$ to remove any residual TissueTek® O.C.T. compound. Subsequently, the sections were fixed in 4% PFA solution for 20 minutes, followed by an additional 10-minute wash in $DBPS^-$.

2.2.2.1 Hematoxylin-Eosin (HE) Staining

Selected slides of endometrial and endometriotic tissue underwent HE staining to allow for detailed examination of their morphological characteristics and to facilitate the identification of regions of interest. The staining was performed according to a standardized protocol established by AG Schenke-Layland (Tübingen, Germany). Following the preprocessing steps described above, the sections were immersed in Mayer's Hemalaun solution for 8 minutes and then rinsed with demineralized water. Microscopic examination ensured optimal nuclear staining. Subsequently, the sections were washed under lukewarm running tap water for 10 minutes to remove excess dye, followed by a brief demineralized water rinse. Eosin G, 1% aqueous solution was applied for 1 minute and 30 seconds, followed by another brief rinse in demineralized water. The samples were then dehydrated in an ascending ethanol series (70%, 90%, and 100%) for 5 minutes each, ending in a dual wash in 100% isopropanol p.a.

for 5 minutes. Finally, the samples were mounted using Isomount® 2000 and covered with a thin glass coverslip.

2.2.2.2 Van Gieson Staining

Van Gieson staining was used to visualize collagen fibers in tissue sections, with nuclei appearing blue-black, collagen fibers red, and muscle and cytoplasmic structures yellow. After standard slide preparation (described in Section 2.2.2), Weigert's iron hematoxylin was applied for 8 minutes to achieve nuclear staining. For this, Weigert's solution A (1% hematoxylin in ethanol) and solution B (29% ferric chloride with a small amount of hydrochloric acid) were prepared separately and mixed in a 1:1 ratio immediately before use.

The slides were then rinsed briefly with distilled water to avoid hematin precipitates and examined under the microscope. If cytoplasmic overstaining was observed, differentiation was performed for a few seconds using a solution of 0.5% HCl-ethanol. This was followed by a 10-minute rinse in running tap water to induce blueing and stabilize the staining. For collagen staining, Van Gieson's solution was applied for 3 minutes. The sections were dipped twice briefly in 70% ethanol, followed by two quick dips in 96% ethanol, then incubated for 1.5 minutes in fresh 96% ethanol. Dehydration was completed with two 5-minute incubations in 100% ethanol, followed by a 5-minute incubation in 100% isopropanol. Finally, the samples were mounted using Isomount® 2000 and covered with a glass coverslip.

2.2.2.3 Movat Pentachrome Staining

Following the standard preparation of the slides described in 2.2.2, the staining was proceeded as described in Table 7.

Solution	Incubation time [minutes]
Verhoeff's staining solution	30
Tap water (running, warm)	5
Purified water	Rinse
2% aqueous ferric chloride	1-2; differentiate under microscopic supervision, until elastic fibers are visible

Purified water	Rinse
5% sodium-thiosulfate	1
Tap water (running)	5
3% glacial acetic acid	3
1% alcian blue solution	25
Tap water (running, warm)	1
distilled Water	Rinse
Brilliant-Crocein–Acid Fuchsin	2
distilled water I	Dip in
distilled water II	Dip in
distilled water III	Dip in
1% Acetic Acid	5 dips
5% Phosphotungstic Acid I	5 min
5% Phosphotungstic Acid II	5 min
100% ethanol I	3
100% ethanol II	3
100% ethanol III	3
Saffron du Gâtinais	45
100% ethanol I	3
100% ethanol II	3
100% ethanol III	3
100% isopropanol p.a. I	5
100% isopropanol p.a. II	5
Isomount 2000	

Table 7 *Russell-Movat Pentachrome staining protocol for cryosections*

Based on Russell's modified Movat Pentachrome staining protocol [110, 111], the tissue components show the characteristic staining pattern outlined in Table 8.

Color	**Tissue structure**
Blue-black	Nuclei and elastic fibers
Yellow	Collagen and reticular fibers

Blue-green	ground substance, mucins and acidic glycosaminoglycans (GAGs)
Intense red	Fibrinoid, fibrin
Red	Muscle cells

Table 8 *The coloring pattern according to the Russell-Movat Pentachrome technique*

2.2.2.4 Weigert's Resorcin Fuchsin Staining

Following the standard slide preparation described in section 2.2.2, the cryosections were incubated in Resorcin-Fuchsin solution for 30 minutes at room temperature. Subsequently, the slides were rinsed under running tap water for 1 minute. Differentiation was performed in 96% ethanol until background staining was optimally reduced, as monitored under a light microscope. Finally, the sections were mounted using the aqueous mounting medium Isomount® 2000 and covered with a thin glass coverslip.

This staining method was applied to visualize elastic fibers within the tissue [112]. The dye complex selectively binds to components of elastic tissue, resulting in a dark violet to black coloration of elastic fibers. In contrast, cell nuclei appear red and the cytoplasm stains light red to pink. Counterstains such as eosin, van Gieson, or trichrome methods may additionally be used to enhance cytoplasmic or connective tissue contrast [113].

2.2.2.5 Picrosirius Red (PSR) and Fast Green Staining

Following the standard preparation described in section 2.2.2, the cryosections were first incubated in acidified distilled water for 5 minutes to optimize dye penetration. The slides were then stained with a mixture of PSR and Fast Green FCF for 60 minutes at room temperature. After staining, the sections were briefly dipped in 70% ethanol for 1 minute, followed by dehydration in 100% ethanol for three times, one minute each. Finally, the sections were mounted using the aqueous mounting medium Isomount® 2000 and covered with a thin glass coverslip.

2.2.2.6 Immunohistochemistry (IHC)

Following the standard cryosection preparation described above, IHC staining was performed using the ImmPRESS™ polymer immunodetection system and ImmPACT™ chromogenic substrates. Prior to staining, tissue sections were carefully encircled using a hydrophobic barrier pen (ImmEdge Pap Pen, Vector Laboratories) to confine reagents to the tissue area and prevent drying or reagent loss during incubation steps. To quench endogenous peroxidase activity, tissue sections were incubated in a solution of 1.5 mL 30% hydrogen peroxide (H_2O_2) in 50 mL methanol for 20 minutes in the dark. Nonspecific binding sites were blocked using Goat block buffer (98% dilution buffer + 2% normal goat serum) for 30 minutes at room temperature. The slides were then rinsed with $DPBS^-$.

For detection of CD10, the sections were incubated overnight at 4°C with the primary mouse monoclonal antibody (anti-CD10, mAb mouse IgG1, 1:100 dilution). After rinsing three times with $DPBS^-$, the ImmPRESS™ anti-mouse IgG reagent was applied for 30 minutes. Signal detection was carried out using the ImmPACT™ DAB kit under continuous light microscope control. The slides were then rinsed again with $DPBS^-$. Nuclear counterstaining was performed using Hematoxylin QS. The sections were then mounted with Dako Faramount Aqueous Mounting Medium.

Separate tissue slides were used for the detection of collagen I (COL I), collagen III (COL III), and perlecan (PRL). Each section was incubated overnight at 4°C with the corresponding primary polyclonal rabbit antibody: anti-COL I (diluted 1:75), anti-COL III (diluted 1:75), or anti-PRL (diluted 1:100). The following day, the ImmPRESS™ anti-rabbit IgG reagent was applied for 30 minutes. Signal visualization was performed using the ImmPACT™ VIP chromogen under light microscopic control. After rinsing with $DPBS^-$, nuclear counterstaining was performed using Hematoxylin QS. The slides were then mounted using Dako Faramount aqueous mounting medium.

2.2.3 Microscopy and Image Analysis

Tile scans were conducted to provide a rapid overview of the entire tissue. Due to the tissue thickness of 10 µm, multiple focal points (approximately 25–30) have been selected to ensure the acquisition of uniformly focused images.

2.2.4 Raman Imaging

For Raman imaging, measurements of cryo-preserved sections of endometrium and endometriosis were performed on a customized WITec alpha300 R Raman microscope equipped with a charge-coupled-device (CCD) camera. Prior to measurement, the tissue sections were rinsed and soaked in $DPBS^-$ for 10 minutes. Calibration and laser power checks were conducted on a silicon slide prior to each measurement to ensure standardization. Raman spectral maps were specifically acquired from endometrial glands (KO) and endometriotic glands (DI). For spectral acquisition, an upright 63x dipping objective, a green laser (532 nm) and a spectrograph with a grating of 600 g/mm were used. Three spectral maps per sample were recorded, each consisting of single spectrum acquired every 0.5 µm across an area of 80 × 80 µm, with an acquisition time of 0.05 seconds per spectrum and a laser power of 60 mW. The TrueSurface module, featuring more than 25 adjustable focus points, ensured precise measurement of large and coarsely textured samples.

2.2.5 Analysis of Spectral Data

The spectral maps were analyzed using Project Five 5.2 software developed by WITec GmbH. To begin, cosmic rays were eliminated from the Raman data using a filter size of 2 and a dynamic factor of 8. Afterwards, a polynomial baseline correction was applied, and the data was cropped and reduced within the range of 600 to 1800 cm^{-1}. Subsequently, a normalization of intensity was carried out.

2.2.6 True Component Analysis (TCA)

The recorded Raman spectra were analyzed using specialized data processing techniques [114, 115]. Firstly, TCA is used for image analysis, allowing direct evaluation of measurements without prior data compression or reduction. TCA clusters similar spectra and assigns them into distinct components, each represented by a specific color. This results in both intensity distribution maps and a color-coded bitmap, visually representing the spatial distribution and relationships between components within the tissue, enabling quick and easy assessment (Fig. 8; Fig. 16, 1).

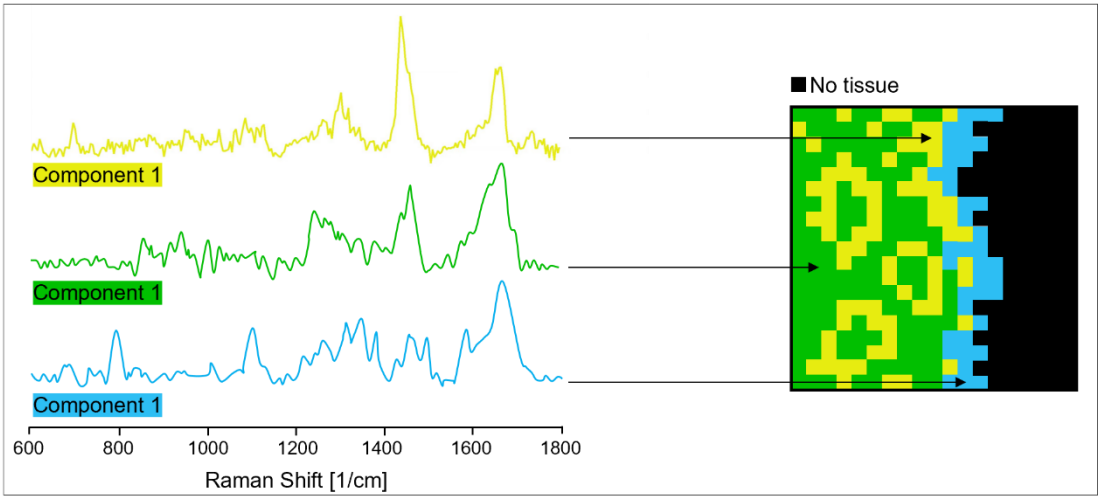

Figure 8 True Component Analysis

Exemplary representation of the Raman spectra (on the left), where spectra are grouped together as components. The resulting bitmap (on the right) reflects the distribution of these components within the sample. Adapted from [116].

2.2.7 Principal Component Analysis (PCA)

Secondly, PCA was employed to reduce the amount of data, facilitating the identification of spectral differences. The Unscrambler software was used for this purpose. In essence, PCA is a powerful multivariate data analysis technique that reduces the dimensionality of spectral data through a vector-based approach [117]. Each vector, referred to as a principal component (PC), accounts for a specific variation within the spectra. By employing an axis rotation method [118], PCA aligns these PCs along directions of maximum variance, generating matrices for scores, loadings, and residuals [119, 120]. The PCs are orthogonal linear combinations of the original variables [121], identifying natural data clusters

(similarities and common features) and outliers (significant deviations from the general pattern) [121]. Plotting the PC loadings against different variables reveals which variables contribute most to the observed differences [121]. The first PC captures the most significant variation, with subsequent components representing decreasing levels of variability in chronological order [114]. In the context of Raman data, the dataset consists of samples (e.g., endometrium and endometriosis) and variables (e.g., Raman shifts for nuclei, ECs, lipids, collagen and elastin) [12]. PCA interprets complex spectra by revealing differences between samples or sample groups, expressed as "scores," and linking them to differences in variables, referred to as "loadings" [119, 122-125]. The scores plot visually displays differences between samples or groups, while the loadings plot illustrates variations in the Raman shifts [126]. By plotting the PC values against each other, it is possible to visually evaluate correlations or separations between datasets, aiding in the identification of patterns, trends, or groupings [114]. This visualization helps to identify key peaks that characterize specific sample types and assess reproducibility within the sample set [119]. Overall, PCA provides a comprehensive overview of the relationships between different sample sets, making it invaluable for analyzing complex datasets like Raman spectroscopy data [120].

3 Results

3.1 Identification of endometriosis by standard pathologic staining

Histologic HE staining and IHC anti-CD10 antibody (anti-CD10) staining are established methods in pathology for detecting endometriosis.

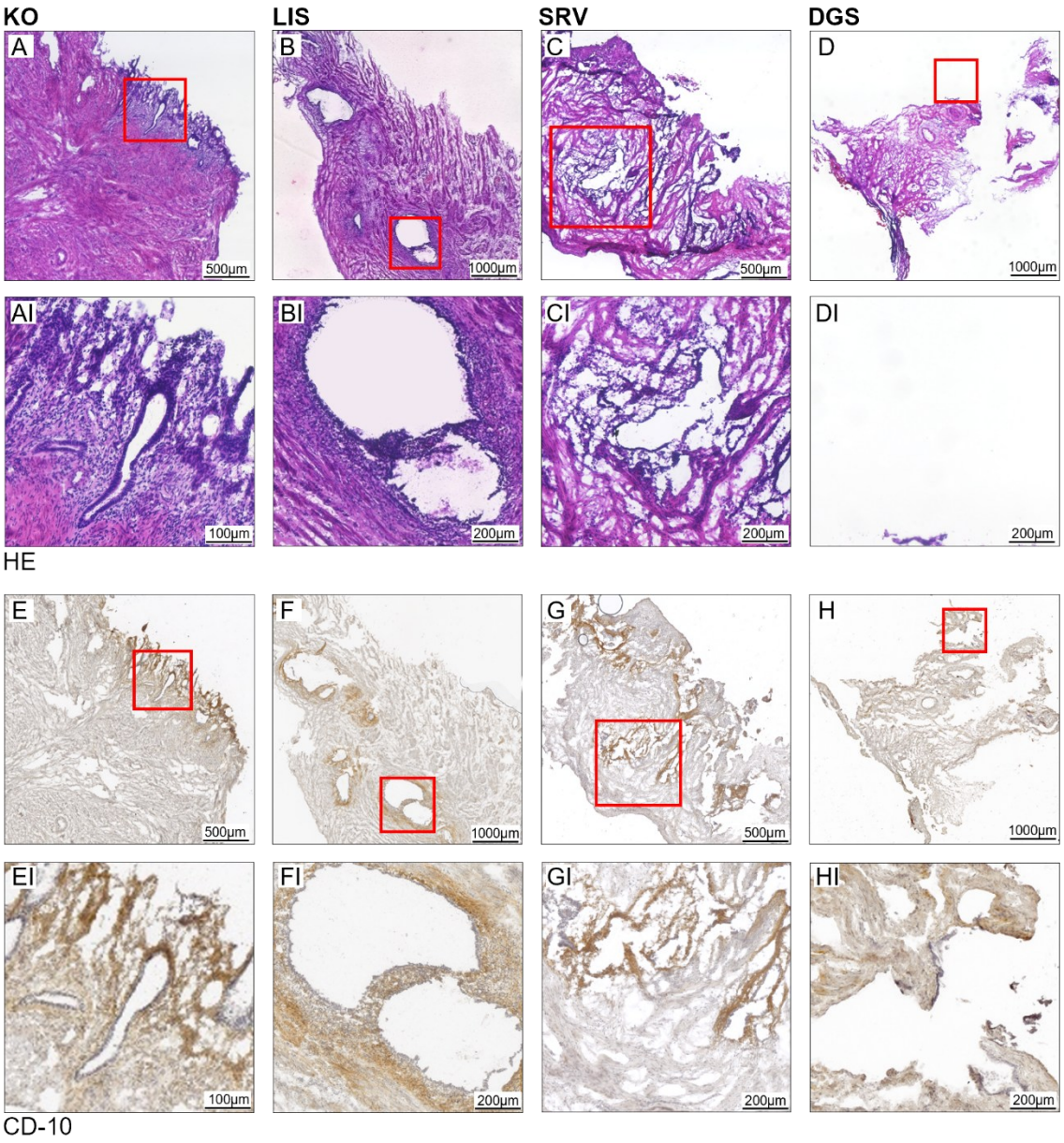

Figure 9 Standard pathologic staining methods to diagnose endometriosis.

Overview images in A–H, with corresponding magnified areas (red rectangles) in AI–HI. Each column represents a sample: KO in A and E, LIS in B and F, SRV in C and G, and DGS in D and H. The scale bars in the overview images are 1000 µm, except for C and G, where they correspond to 500 µm. The scale bars in the magnified images are 100 µm, except for C and G, where they correspond to 200 µm.

HE staining is a rapid and widely used technique that provides an overview of the general tissue architecture and highlights cellular organization or disorganization. This study used HE staining to locate endometrial and endometriotic glands, which proved particularly useful in endometriosis samples due to their irregular distribution. Following HE staining, consecutive tissue sections were stained with anti-CD10 – a marker for endometrial stroma – to confirm the presence of ectopic glandular tissue and thus verify the diagnosis of endometriosis. CD10 is commonly used in diagnostic pathology to identify endometrial stromal cells and to distinguish them from other mesenchymal or vascular components. Both staining methods are considered simple and time-efficient.

When KO samples (KO, Fig. 9A/E) are compared with DI samples (DI, Fig. 9F–H), distinct structural differences become apparent. In KO samples, the glands appear densely packed, homogeneous, and well demarcated. They are arranged in an almost orthogonal, parallel orientation to the uterine lumen and are confined exclusively to the endometrium, without invading the adjacent myometrium (see Fig. 10).

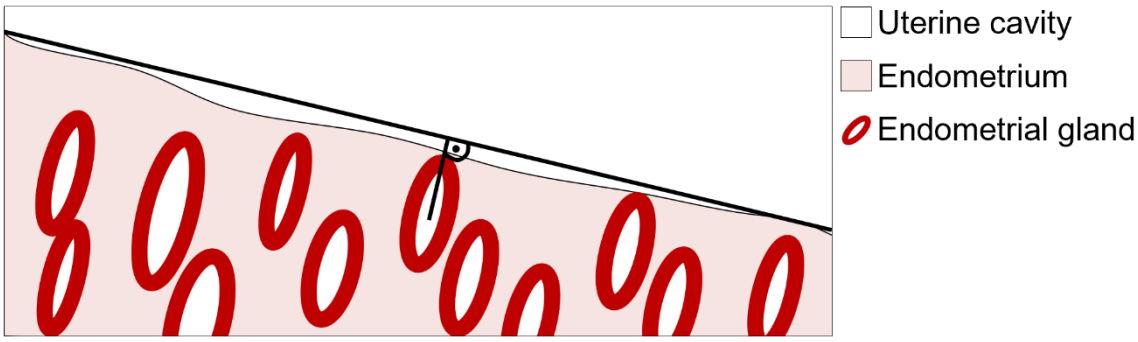

Figure 10 Schematic representation of glandular organization in the endometrium

The oval-shaped structures depict glands within the endometrium (pink). The white area represents the uterine cavity. The intersecting black lines serve to illustrate the regular, almost orthogonal orientation of the glands.

In contrast, DI samples exhibit highly irregular and disorganized glandular distributions. The glands vary markedly in shape, size, and orientation, and no consistent spatial relationship can be observed. Some glands appear isolated, while others are closely clustered or fused. This morphological heterogeneity is a characteristic feature of ectopic lesions.

In both HE- and anti-CD10 staining similar color patterns are observed in KO and DI samples. In the HE-stained sections, the endometrium appears dark violet and is therefore easily distinguishable from the adjacent paler myometrium. Glands and blood vessels both stain dark purple due to their high density of cell nuclei, which may complicate their differentiation in DI samples, where glandular structures are randomly dispersed.

Anti-CD10 staining aids in distinguishing glands from blood vessels by selectively staining the pericellular stroma in a brownish hue, while glandular ECs appear bluish, particularly evident in the magnified images (Fig. 9AI–HI). The adjacent myometrium, composed predominantly of smooth muscle tissue [1], shows minimal staining and appears pale in comparison. The presence of CD10-positive stromal tissue surrounding glandular structures is considered a diagnostic hallmark of endometriosis.

The morphology of the endometrial glands varies throughout the course of the menstrual cycle [127]. During the proliferative phase, the glands are generally uniform in shape. They appear straight, short, and narrow [128]. Inactive glands from a previous cycle may present a cuboidal and fissured shape [128]. In the mid-proliferative phase (8^{th}–10th day of the cycle), glands typically exhibit columnar epithelium and a more elongated, curved appearance [128]. In the late proliferative phase (11^{th}–14th day of the cycle), the glands become densely coiled and demonstrate mitotic activity and nuclear pseudostratification [128]. Myometrial cells, in contrast appear spindle-shaped with elongated nuclei [129]. All samples included in this study were collected in the early and mid-proliferative phase of the menstrual cycle.

3.2 Movat Pentachrome

For further morphological characterization and detailed analysis of the extracellular matrix composition in DI and KO samples, Movat Pentachrome staining was performed (Fig. 11). This histologic technique enables the differentiation of various matrix components based on their distinct color reactions (Table 8).

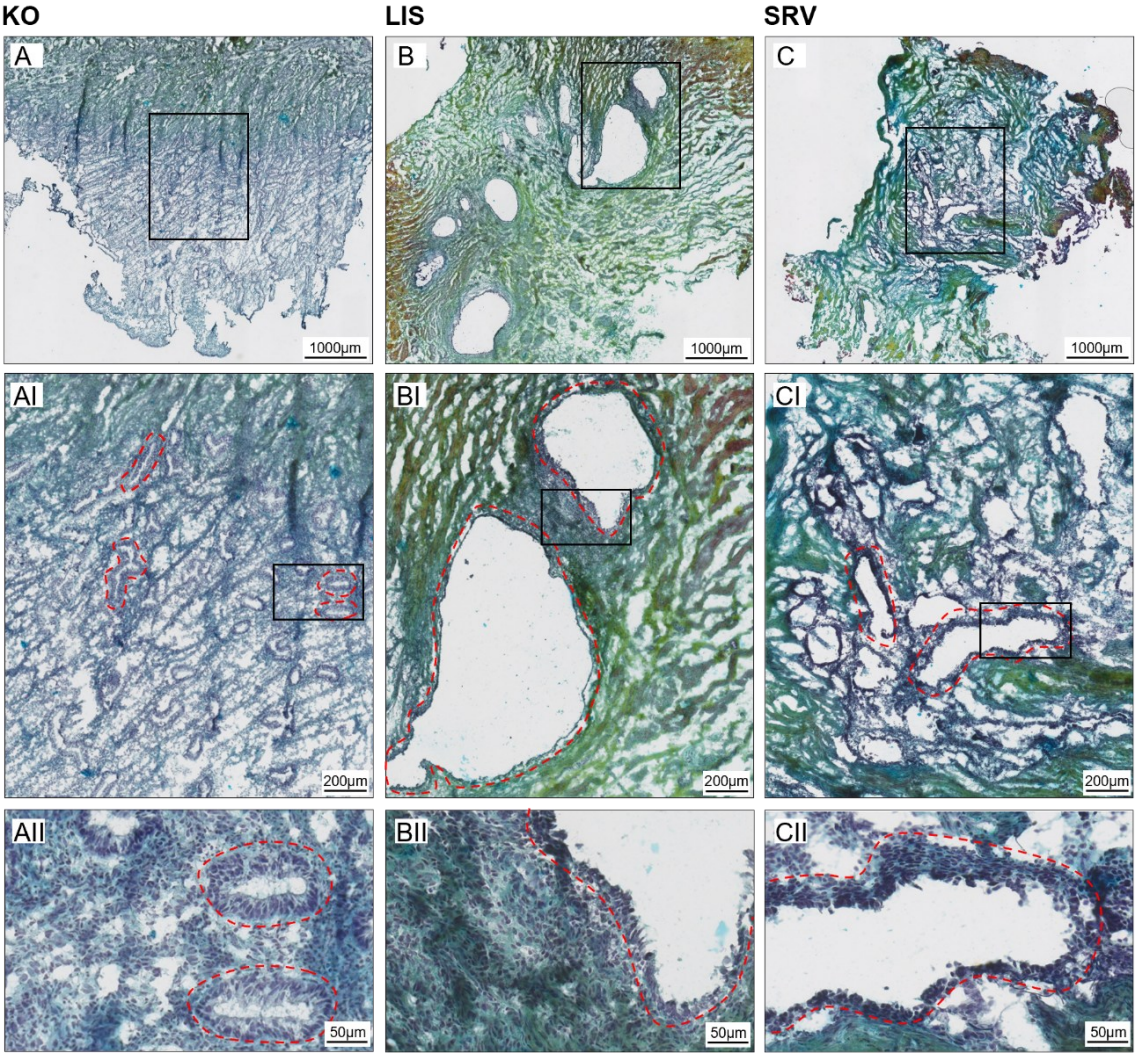

Figure 11 General overview of the tissue composition with Movat Pentachrome

KO is presented in A, DI in B (LIS) and C (SRV). Each column represents one sample. Images marked with I and II are respectively the black rectangles at higher magnification. Some of the glands are framed in red to facilitate their recognition. The scale bars are the same for each row and correspond to 1000 µm, 200 µm, 50 µm (top to bottom).

The uterine section (Fig. 11 KO) displays both the KO and the adjacent myometrium. The myometrium (Fig. 11 KO, A) appears greenish, indicating the

presence of mucins, acidic GAGs, and collagen fibers. The neighboring KO stands out due to its light blue coloring, reflecting a high concentration of GAGs. Glands within the KO are small, oval-shaped, and densely clustered together.

The ectopic glands found in the LIS (Fig. 11 LIS) are way larger compared to those in the KO. The stroma surrounding the glands and the glands themselves appear in a bluish color, consistent with the findings in the KO, indicating the presence of GAGs. The rest of the extracellular matrix presents a spectrum ranging from green to yellow, indicating a substantial amount of collagen and/or reticulin alongside mucins and GAGs. Towards the tissue's periphery, the yellow stain dominates suggesting the presence of collagen and/or reticulin. The red-stained fibrin is present in the periphery of the tissue, but not in immediate proximity to the gland itself.

Similarly, the endometriotic glands in the SRV (Fig. 11 SRV) show a blue coloration of both glands and surrounding stroma, consistent with high GAG and mucin content. As in the LIS, collagen and reticulin are present around the glands, contributing to the greenish coloration.

A comparative analysis of the endometriotic lesions of the SRV and LIS with the glands of the KO reveals several differences. Glands in the endometriotic lesions are larger, morphologically more heterogeneous, partially disrupted and lack orientation within the tissue. The glandular cells themselves are less columnar, compared to those in the KO, and exhibit a distinctly altered morphology. Notably, glandular cells in endometriotic lesions show an increased nuclear-to-cytoplasmic ratio (N/R), resulting in a darker staining appearance. Elastic fibers, which stain black in Movat Pentachrome, are observed in DI but not in KO. In addition, DI tissues show a more complex extracellular matrix composition, including collagen, reticulin, elastic fibers, mucins, and GAGs. Fibrin, identifiable by its red staining, is localized predominantly at the periphery of DI tissues.

3.3 Distribution Pattern of Elastic Fibers in KO and DI

Various staining methods are available for the visualization of elastic tissue, including Weigert's Resorcin Fuchsin, Orcein, Gomori and Verhoeff stains [130]. A common challenge is distinguishing elastic fibers from collagen and smooth muscle in different tissues, which often requires a combination of staining techniques [130].

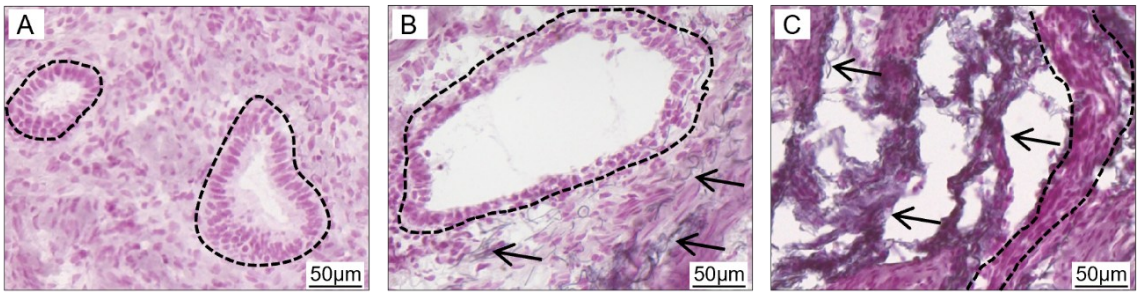

Figure 12 Distribution pattern of elastic fibers in KO and DI

Stained tissue sections with Resorcin Fuchsin displaying the KO (A) and two endometriotic lesions, the LIS (B) and SRV (C). Glands or glandular fragments are outlined in black; the elastic fibers are marked with black arrows. The scale bar represents 50 µm.

The distribution pattern revealed by Resorcin Fuchsin staining is consistent with the findings from Movat Pentachrome staining. In the KO sample (Fig. 12A), the glands can be identified by their palisade-like nuclear arrangement (outlined in black). Notably, no elastic fibers are detected in the stromal compartment of eutopic endometrial glands. These findings are consistent with the study by Egging et al. who also reported the absence of elastic fibers in eutopic endometrium and their presence in fibrotic or pathologically remodeled tissues [131].

In contrast, the ectopic glands in DI specimens (Fig. 12B and 12C) are much larger. In some cases, complete glands are visible, but in others only gland segments are visible. Numerous elastic fibers are irregularly distributed in the immediate vicinity of the glands in the pericellular stroma of these lesions. These fibers appear as dark purple to black, hair-like structures that vary greatly in density and spatial distribution (Fig. 12, black arrows). Depending on the region, the fibers may form distinct bundles or appear as a fine network separated by narrow gaps. The presence of elastic fibers in the stromal compartment in DI

suggests tissue remodeling and fibrotic changes, which can be associated with the chronic inflammation in endometriosis [132]. This is further supported by histologic studies using Elastica-Van Gieson staining, which report an increased abundance of both collagen and elastic fibers in endometriotic lesions [133].

3.4 Collagen Fiber Distribution and Content in KO and DI

Hematoxylin and van Gieson stain (HvG) are common and straightforward methods for identifying collagen and other connective tissue components. With this technique, smooth muscle fibers appear yellow, elastic fibers appear black, and collagen fibers appear red. Cell nuclei are stained black with hematoxylin.

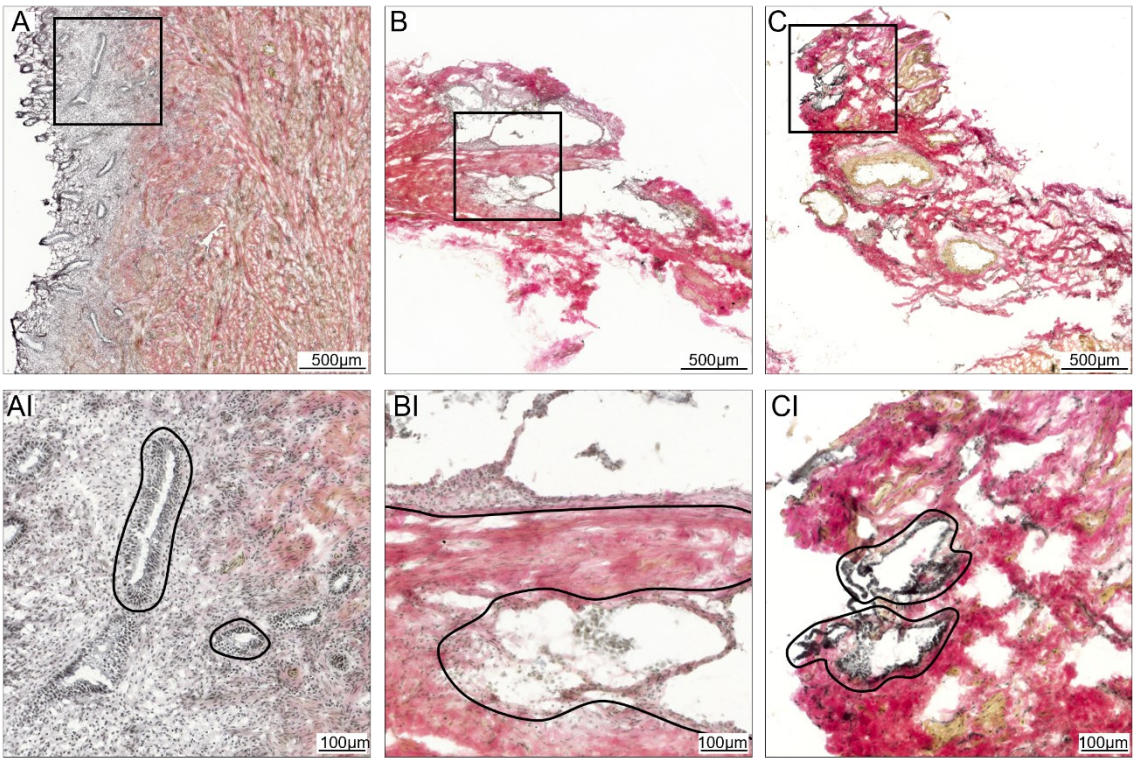

Figure 13 Histologic visualization of collagen fibers

HvG staining of KO (A) and DI samples from LIS (B) and SRV (C). Two glands are outlined in each magnified image (bottom row) in black. Scale bars correspond to 500 µm in the top row and 100 µm in the bottom row.

In the KO sample (Fig. 13 A/AI), the myometrium can be clearly distinguished from the adjacent endometrium due to its high collagen fiber content (red) and smooth muscle (yellow) content. The endometrial tissue appears dark blue due to its high cell nuclear density. As in previous stains, the glands in the KO sample

can be identified by their palisade-like arrangement of nuclei that form oval structures.

DI samples exhibit a high proportion of collagen fibers and smooth muscle tissue surrounding the glands. The glands are identifiable by the dense accumulation of cell nuclei. Compared to KO samples, the glands in DI are larger and more heterogeneous, each exhibiting a unique size and shape. The arrangement of cell nuclei within the glands is not as organized as in the endometrial glands. The nuclear arrangement within these glands is less organized.

Another key difference is the presence of elastic fibers (black) in the DI samples – particularly evident in the SRV (Fig. 13 C), which are absent in KO tissues.

3.5 Quantification of Collagen Fibers

Both Masson's Trichrome and van Gieson staining have traditionally been used for collagen visualization in tissue sections [134]. However, both methods exhibit limited sensitivity for fine collagen fibrils, potentially resulting in an underestimation of total collagen content. Moreover, van Gieson stain is prone to fading over time [134]. These limitations have led to the widespread adoption of the PSR staining method in combination with polarized light microscopy as a more robust and sensitive method for collagen assessment [134].

PSR selectively binds to basic amino acid residues (e.g., lysine, hydroxylysine, arginine) in collagen fibrils via its sulfonic acid groups [135]. Owing to its elongated molecular structure, the dye aligns parallel to the fibrils, resulting in a marked enhancement of collagen's natural birefringence—reported to exceed 700% relative to unstained sections [135]. This enhancement enables the visualization of even very fine collagen fibers.

While early studies suggested that birefringence color might be indicative of collagen type [135], more recent research has refined this interpretation. Dayan et al. demonstrated that birefringence hue is influenced not only by fiber diameter but also by fibril alignment, molecular packing, and hydration state [136]. In 2005, Rich and Whittaker introduced a four-color classification scheme—green, yellow, orange, and red—representing an ascending order of fiber thickness, which may

also reflect progressive tissue remodeling [134]. However, they explicitly rejected any correlation between hue and collagen type. Twelve years later, Rittié emphasized the multifactorial nature of birefringence and cautioned that hue analysis under polarized light microscopy should be considered a qualitative and relative measure of collagen organization [137]. She further stressed that definitive conclusions regarding fiber maturity, diameter, or subtype require validation through complementary techniques such as immunohistochemistry or electron microscopy [137].

In this study, 10 µm cryosections were stained with PSR and counterstained with Fast Green. The counterstain enhanced the contrast of non-collagenous components under brightfield microscopy by staining cytoplasmic and matrix proteins green. This facilitated the interpretation of structural orientation and tissue architecture. Tissue sections were examined under circularly polarized light. Collagen fibers appeared birefringent in varying hues, while non-collagenous elements and interstitial background remained dark. The thickness and/or maturity of collagen fibers can be classified based on the four distinct color hues defined by Rich et al. [134] in 2005. Subsequent image analysis was performed using ImageJ and MATLAB to quantify the pixel counts corresponding to each hue (green, yellow, orange, red). In the subsequent MATLAB analysis, the pixels corresponding to each color hue were counted. Collagen fibers from KO samples (n = 3) were compared with those from DI samples (n = 3), which were collected from various locations: LIS (n = 3), SRV (n = 1), and DGS (n = 1).

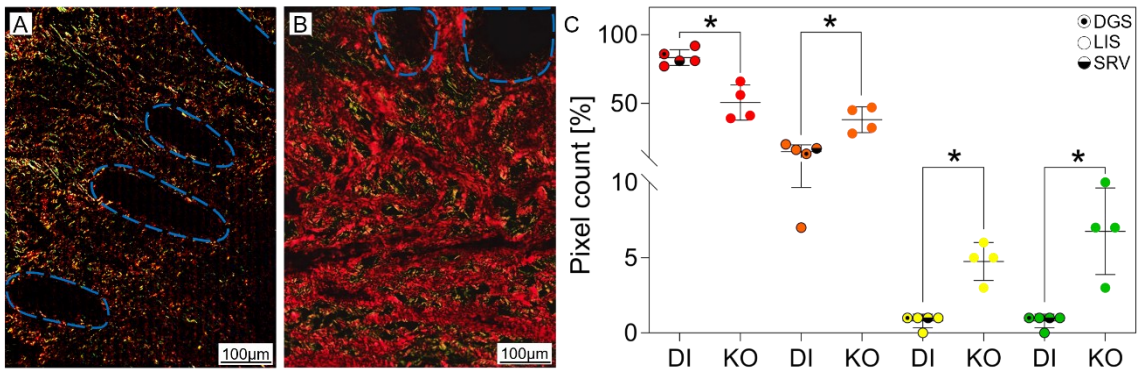

Figure 14 Quantification of collagen fibers using PSR and Fast Green stain

The glands in KO (A) and DI (B) are outlined in blue. Scale bars correspond to 100 µm. The scatter plot (C) shows the fractions of the four distinct color hues defined by Rich et al. [134]

*comparing KO (●) with DI (LIS ○, DGS ◉, SRV ◒). Mann-Whitney U test was performed to compare the individual color proportions for KO (n=4) compared to DI (n=5) (LIS n=3; SRV n=1; DGS=1). Results are expressed as mean ± SD. *p < 0.05.*

In both the KO (Fig. 14 A) and DI samples (Fig. 14 B), the glands, including their lumina, appear dark to black under circularly polarized light. Compared to DI samples, the KO tissue exhibits a markedly higher proportion of green, yellow, and orange birefringent fibers. The overall darker appearance of the KO tissue may reflect a higher proportion of non-collagenous elements or a more porous matrix. This finding is consistent with the higher abundance of thinner collagen fibers typically observed during the proliferative phase of the endometrium, a phase marked by active reconstruction of the Stratum functionale.
Statistical analysis revealed a significantly higher proportion of red fibers in the DI samples (Fig. 14 B), indicating the presence of thicker and more densely packed collagen. However, no clear differences in the distribution or arrangement of the various fiber thicknesses were detected, nor was there an increased content of thin fibers near the glands.

When comparing the ectopic glands from different anatomical locations, significant differences were also observed (Supplementary Fig. 25). In particular, the SRV and DGS samples showed markedly divergent birefringence profiles.

3.6 Heterogenous Phenotype of Endometrial Foci

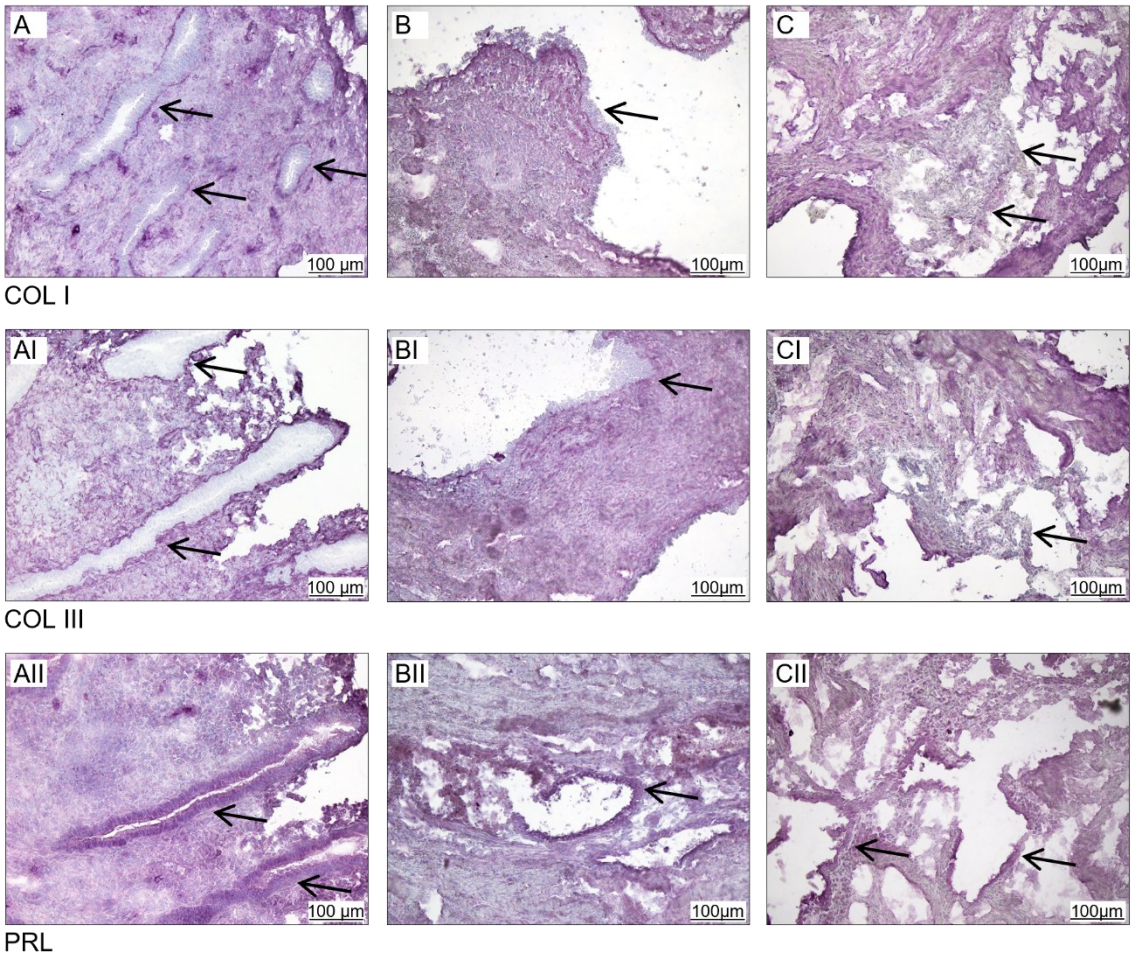

Figure 15 IHC characterization of endometriosis

IHC staining of KO (A) and DI of LIS (B) and SRV (C) with anti-COL I in A–C, anti-COL III in AI–CI, and anti-PRL, in AII–CII. The black arrows highlight the glands. The scale bars correspond to 100 µm.

The IHC stain was performed to highlight the heterogeneous phenotype of endometrial foci. The three antibodies anti-COL I (Fig. 15 A–C), anti-COL III (Fig. 15 AI-CI) and anti-PRL (Fig. 15 AII–CII) were applied to tissue samples of KO (Fig. 15 A) and DI (Fig. 15 B–C).

In the KO samples (Fig. 15 A), the epitopes of anti-COL I and anti-COL III were detected both in the stroma surrounding the glands and as a type of boundary around the glands. The well-defined and uniform glandular architecture in the KO samples, highlighted by the anti-COL I and anti-COL III staining, emphasizes the integrity and organization of these structures.

In contrast, the DI samples (Fig. 15 B–C) exhibited a rather heterogenous glandular configuration. In the LIS samples (Fig. 15 B), the endometriotic glands both anti-COL I and anti-COL III were observed as linings surrounding the glands. However, in the SRV sample (Fig. 15 C), although collagen was present around the glands, the clear demarcation of the glands observed in the KO samples was not as evident. This indicated a more disrupted or varied glandular architecture in the DI samples.

PRL staining (Fig. 15 AII, BII, CII) revealed that anti-PRL epitopes were primarily localized within the glandular cells, with punctate deposits also present in the surrounding tissue. This pattern was consistent across KO and DI samples, though the density and distribution of these deposits varied, reflecting differences in glandular and stromal composition between the samples.
The results of IHC staining showed that both anti-COL I and anti-COL III are integral components of the glandular and stromal architecture in endometrial tissue. There was a clear difference in glandular structure between KO and DI specimens, with KO specimens showing more defined and uniform glandular structures, while DI specimens showed a more heterogeneous and disrupted architecture. Anti-PRL was primarily localized within the glandular cells, but also showed a dispersed presence throughout the surrounding stroma, suggesting its involvement in the structural and functional organization of the tissue.

3.7 Identification of the Prominent Tissue Components with TCA

TCA was used to identify tissue components with similar spectral and hence biochemical properties. All similar structures showed clusters on a generated pseudocolored map (bitmap). This enabled the identification and localization of the same prominent tissue components of the glands and their surroundings in endometrial samples (Fig. 16 A), and endometriosis samples (Fig. 16 B and C).

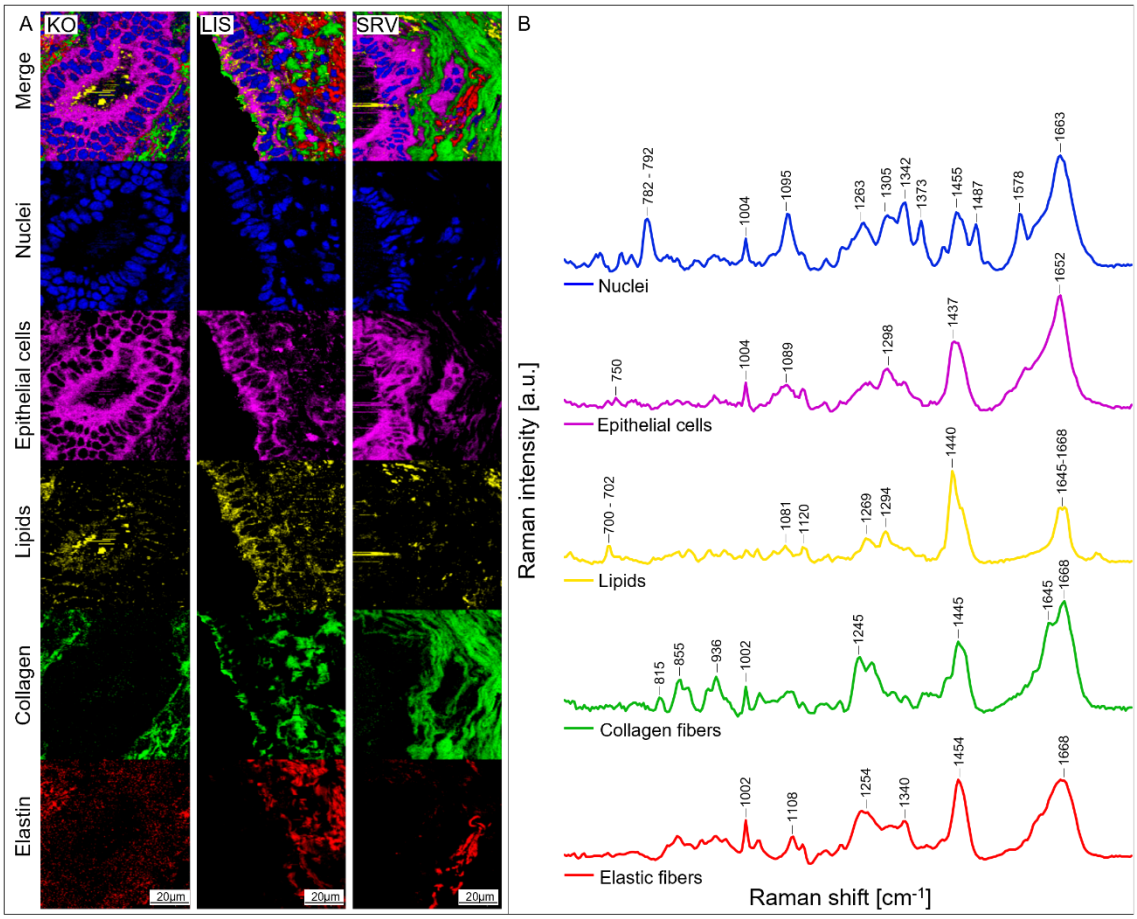

Figure 16 TCA of eutopic and ectopic endometrial glands

(A) Marker-independent TCA of KO and DI of LIS and SRV identifies nuclei (blue), ECs (pink), lipids (yellow), collagen fibers (green) and elastic fibers (red). Scale bar equals 20 µm. (B) Average spectral signatures for the molecular assignment of the tissue components with labeled characteristic peaks of the individual components.

The Raman spectra of the identified components are shown in Fig. 16 B, focusing on the fingerprint region from 600 to 1800 cm^{-1}. This spectral range contains numerous characteristic bands that reflect specific molecular vibrations related to chemical composition and structure of the sample. These bands provide detailed information about functional groups, molecular conformations, and bonding types of sample components. Raman bands arise from vibrational modes that are highly dependent on the molecular structure and intramolecular interactions; thus, spectral patterns differ significantly between substances. This region is referred to as the "fingerprint region" because it often exhibits unique substance-specific signatures, enabling precise molecular identification and discrimination.

The blue component appears in a palisade-like arrangement in both KO and DI. These clusters are tightly packed and form ring-shaped structures that vary in size and shape, particularly when comparing KO (Fig. 16 KO) with DI (Fig. 16 LIS and SRV). The Raman spectrum of the blue component (Fig. 16 B) exhibits characteristic peaks that can be attributed to nucleic acids (Table 9); indicating that this component represents cell nuclei.

The pink component was consistently located adjacent to the blue component in both KO and DI samples and was found to surround. Upon closer inspection, the pink component was observed enveloping the nuclei.

Its spectral features (Table 10) include peaks attributable to amino acids and (phospho)lipids. These findings support the interpretation that the pink component may correspond to the cytoplasm of glandular ECs. The spatial co-localization of the blue and pink components is consistent with glandular structures observed in both KO and DI samples. The yellow dot-like component was observed throughout the entire tissue sections in all samples (Fig. 16 A). Spectral analysis revealed characteristic peaks associated with cholesterol, as well as aliphatic CH_2 and C = C stretching vibrations – which are predominantly found in lipid-rich regions. Based on these spectral features, the yellow component may correspond to lipids.

The green and red components both exhibit a fibrillar morphology in the bitmap, which is particularly evident in the SRV sample (Fig. 16 SRV). These components are located around the glandular areas, i.e., the blue and pink regions, and are found exclusively outside the lumen formed by the blue component. Based on their Raman spectra, the green component could correspond to collagen fibers and the red component to elastic fibers. Interestingly, the red component was predominantly observed in the DI samples, whereas it appeared mainly as spectral noise in the KO samples. This observation is consistent with previous histologic studies reporting that the eutopic endometrium contains few or no elastic fibers [131].

3.7.1 Nuclei

The blue component (Fig. 16 A) exhibits several characteristic peaks and bands (Table 9), which can be attributed to the nucleic acid bases uracil, adenine, guanine, cytosine and thymine, as well as to the deoxyribonucleic acid (DNA) backbone and deoxyribose. Based on both image morphology (Fig. 16 A) and spectral assignment (Table 9), the blue component corresponded to the cell nuclei.

Wavenumber (cm^{-1})	Assignment	References
782–792	Uracil, Thymine, Cytosine ring breathing; O-P-O symmetric stretch	[138-142]
1084–1095	DNA backbone: PO_2 stretch	[138, 143-145]
1263	Thymine, Adenine (ring breathing modes of the DNA/ribonucleic acid (RNA) bases) =C-H bend (protein), Thymine, Adenine	[146, 147]
1304–1342	Adenine, guanine	[138-142]
1373	Thymine, adenine, guanine (ring breathing modes of the DNA/RNA bases)	[145-147]
1455	Deoxyribose	[144]
1487	Guanine, adenine	[140]
1578	Nucleic acid (adenine, guanine)	[138, 140, 145]
1659–1671	Thymine, guanine, cytosine	[139, 143, 144, 148]

Table 9 *Characteristic bands and peaks for Nuclei*

3.7.2 Epithelial Cells with Cell Organelles other Than Nucleus

Eukaryotic cells consist of cytoplasm that contains various subcellular structures such as the plasma membrane, nucleus, mitochondria (MIT), lysosomes, macromolecules (proteins, DNA, and RNA), the endoplasmic reticulum (ER), and

numerous smaller molecules involved in metabolism and nutrient storage [149, 150]. The spatial arrangement of these organelles contributes to the overall shape of the cell. Endometrial glandular ECs are simple single-layered and columnar [151]. Cell organelles like ribosomes are made up of ribosomal RNA (rRNA) and ribosomal proteins. MIT possess a double-layered membrane composed of phospholipids and proteins, and are primarily made up of proteins (60%) and lipids (35%) [152].

The pink component (Fig. 16 A) displays several characteristic Raman peaks and bands corresponding to phospholipids, proteins, and lipids (Table 10). Based on the image morphology (bitmap in Fig. 16 A) and spectral features (Table 10), this component was assigned to the ECs of the glands, including their organelles – excluding the nucleus (blue component).

Wavenumber (cm^{-1})	Assignment	References
750	Cytochrome complex inside MIT	[153, 154]
1004	Symmetric ring breathing mode of phenylalanine	[145, 152]
1089	C-C stretch	[152]
1298	CH_2 deformations (lipid); Amide III	[94]; [152]
1437	Phospholipid (phosphatidylserine); CH_2 bend of the hydrocarbon chains	[155]; [152]
1652	Lipid (C=C stretch)	[94]

Table 10 *Characteristic bands and peaks for cell organelles and cytoplasm of the epithelial cells*

3.7.3 Lipids

Based on the bitmap image (Fig. 16 A) and the peak assignments (Table 11), which are consistent with the literature data, the yellow component was identified as lipids.

The fingerprint region of the Raman spectra for lipids shows three spectral regions: 1500–1400 cm^{-1}, 1300–1250 cm^{-1}, and 1200–1050 cm^{-1}. Vibrations in the 1500–1400 cm^{-1} region are generally attributed to the scissoring motions of the CH_2 groups, whereas bands around 1300 cm^{-1} are associated with twisting

motions of the CH_3 groups. In the 1200–1050 cm^{-1} range, the observed bands are typically linked to the C–C skeletal stretching vibrations.

It is important to note that the Raman spectral characteristics of individual lipids can vary significantly, depending on multiple factors, including the degree of saturation, liquid phase state, the presence of geometric isomers, as well as polymorphic or polytypic forms. Additionally, hydrophilic functional groups may affect properties of lipid solubility [156].

Wavenumber (cm^{-1})	Assignment	References
702	Cholesterol, cholesterol ester	[155]
1030–1130	skeletal C─C stretches (cis 1030–1040; chain trans 1055–1066; chain random 1080–1085)	[138, 141, 157]
1254–1284	═CH deformations	[138-140, 143, 157]
1295–1305	twisting motions of the CH_3 groups	[156]
1440–1460	CH_2 scissors	[139, 141, 143, 158]
1645–1660	C═C cis stretch	[139, 141, 143, 148, 157, 158]

Table 11 *Characteristic bands and peaks for lipids*

3.7.4 Collagen fibers

Based on the spatial distribution (Fig. 16 A) and the peak assignments (Table 12), which are supported by literature, the green component was attributed to fibers.

Collagen is the most abundant macromolecular protein in the human body and plays a key role in the extracellular matrix (ECM) of connective tissues [159]. A prominent Raman band at 815 cm^{-1} indicates the presence of glucosyl-galactosyl-hydroxylysine, which is particularly intense in COL I compared to type IV collagen (COL IV), thereby enabling their differentiation [159].

The characteristic peak pair at 855 cm^{-1} and 936 cm^{-1} is associated with the amino acid side-chain vibrations of proline and hydroxyproline, as well as a C=C stretching of the collagen backbone [159-161]. RMS is also sensitive to the secondary structures of collagen, such as α-helix and β-sheet [159], which are crucial for the stability and organization of collagen fibrils [159]. These secondary structures are typically examined using the amide I and III bands [159].

Wavenumber (cm^{-1})	Assignment	References
815	glucosyl-galactosyl-hydroxylysine on/within leucine crosslinks in tropocollagens	[159]
855	ν(C-C) of the proline ring and ring breathing mode (δ(CCH)) of tyrosine; proline and hydroxyproline, as well as a (C=C) vibration of the collagen backbone	[160, 162, 163]
938	proline and hydroxyproline, as well as a (C=C) vibration of the collagen backbone	[160, 164]
1002	C-C aromatic ring stretching, phenylalanine (high in COL IV)	[165, 166]
1248	Amide III, β-sheet (COL III)	[162, 167-170]
1445	CH_2 and CH_3 deformation	[164]
1645	Amide I, α-helix	[94]
1668	Amide I, β-sheet	[169, 171-173]

Table 12 *Characteristic bands and peaks for collagen fibers*

3.7.5 Elastic fibers

The red component was assigned to elastic fibers due to its fibrillar morphology and distinctive Raman spectral features. Elastic fibers are supramolecular assemblies primarily composed of elastin, a key protein that provides connective tissues with their elastic recoil properties [174, 175].

Elastin has a largely disordered structure and lacks a well-defined secondary structure as reported by Bruce et al. and confirmed by Mammi et al. The amide I and III bands of elastin appear at approximately 1668 cm^{-1} and 1250 cm^{-1}, respectively, reflecting its irregular chain conformation [176]. Furthermore, elastin appears to lack a well-defined secondary structure. A unique biochemical feature of elastin is the presence of the amino acids desmosine and isodesmosine – unique tetrasubstituted aromatic pyridinium derivatives that serve as covalent cross-links within the insoluble elastin network [174-176]. Raman bands at 1108 cm^{-1} and 1340 cm^{-1} have been attributed to the vibrational modes of these cross-links [175-177]. A desmosine analysis can be used to determine the elastic fiber content in tissue samples [174].

Wavenumber (cm^{-1})	Assignment	References
1002	C-C aromatic ring stretching, phenylalanine	[165, 166, 174]
1108	νCC, νCN, νCO; desmosine, isodesmosine	[175-177]
1250	ν(CN), δ(NH), Amide III, β-pleated sheet	[138, 142, 174, 175, 178]
1340	$\delta(CH_2)$, $\gamma_\omega(CH_2)$, $\gamma_t(CH_2)$, desmosine	[175-177]
1454	Amide II, $\delta(CH_2, CH_3)$	[164, 175-177]
1668	Amide I, β-sheet	[176, 177]
δ (deformation), γ_ω (wagging coordinate), γ_T (twisting coordinate), ν (stretching)		

Table 13 *Characteristic bands and peaks for elastic fibers*

3.8 PCA of KO and DI of all Components

In contrast to TCA, which isolates and quantifies specific components, PCA enables a comprehensive analysis of multidimensional data by reducing complex patterns to essential features. To investigate the molecular differences between the KO (n=3) and DI (n=3) samples, PCA was performed for nuclei, ECs, lipids, and collagen fibers. TCA revealed that no elastic fibers were present in the stroma of the KO samples (Fig. 16), therefore no PCA was performed for this component.

Three scans of three different glands were performed per sample. From each of these scans, 200 spectra were extracted, resulting in a total of 4800 spectra per component. In the scatter plot (Fig. 17–21 A), each point represents one of these 4800 data points. For each donor, the spectra were averaged to create a single point in the graph: blue for KO and red for DI (Fig. 17–21 C).

From two LIS donors, additional samples were collected from the SRV and DGS regions. For each region, three scans from three distinct glands were acquired, following the same protocol as for the primary samples. Consequently, the DI analyses now include two additional data points representing the SRV and DGS regions (Figs. 17–21C).

3.8.1 Nuclei

The PCA of the nuclear spectra revealed no significant differences between the KO and DI samples across the first seven PCs. However, certain trends were observed, suggesting potential underlying patterns and group-specific variations (Supplementary Fig. 22).

3.8.2 Epithelial Cells

3.8.2.1 PC-5 of Epithelial Cells

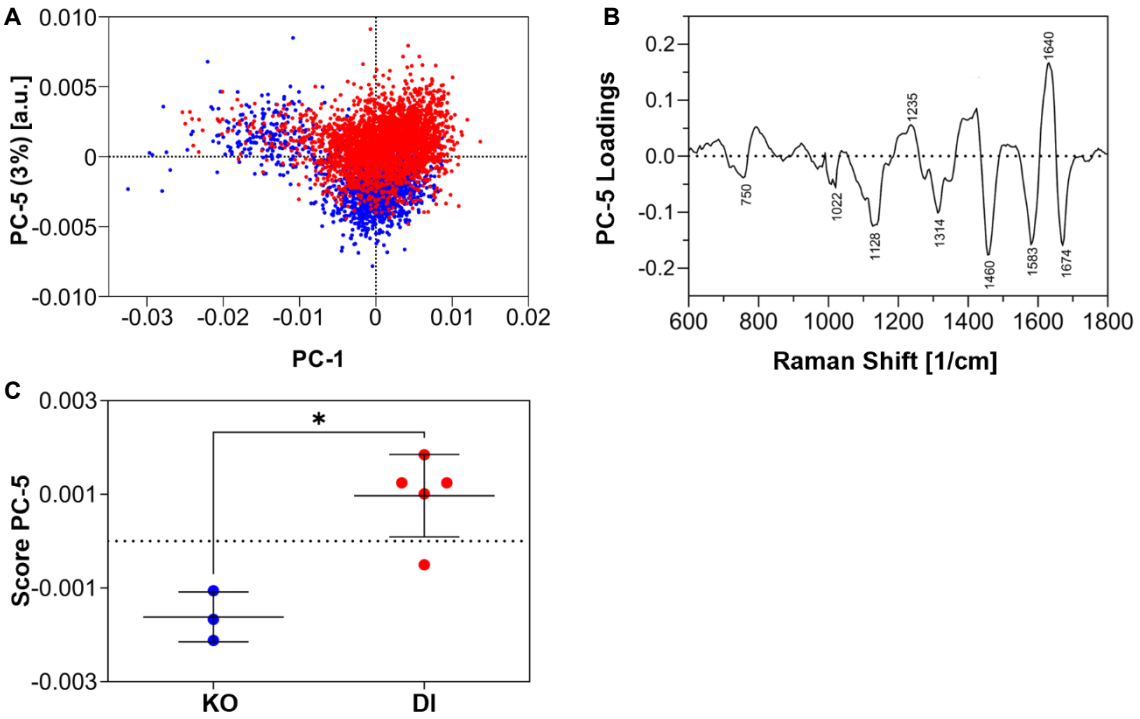

Figure 17 *PCA of Epithelial cells PC-5*
Scores plot of PC-5 and PC-1 (A). Loadings of PC-5 (B). The characteristic wavenumbers are labeled. Two-tailed Mann-Whitney U test was performed to obtain the score value of PC-5 comparing the KO (blue) and DI (red) (C). KO n=3, DI n= 5. DI from LIS (n=3), SRV (n=1) and DGS (n=1).

Wavenumber (cm^{-1})	Assignment	References
(w) 750	Cytochrome complex inside MIT	[153, 154, 179]
(w) 1022	ν(CC), ν(CO), β_{ip}(COH) D-(+)-glucose	[180]
(s) 1128	Cytochrome C	[179]
(m) 1235	Amide III (β-fold)	[181]
(m) 1315	Cytochrome C	[179]
(s) 1460	$\delta(CH)_2$ D-(+)-glucose; Glycogen	[180]
(s) 1583	Cytochrome C	[179]
(s) 1640	Amide I; α-helix/triple-helix (ordered helical structures)	[182-186]
(s) 1674	Amide I; disordered structure	[187, 188]

β_{ip} (in-plane bending), s (strong), m (medium), w (weak)

Table 14 *Loadings of EC PC-5*

The score values of PC-5 show a significant difference between the spectral signatures of KO and DI of the ECs.

PC-5 accounts for 3% of the total variance. In the score plot, DI samples are shifted towards the positive y-axis, while KO samples are shifted towards the negative y-axis. The corresponding loadings (Fig. 17 B) indicate which spectral bands contribute to this separation. Spectral bands associated with the upward clustering of DI samples are located at 1235 cm^{-1} and at 1640 cm^{-1}. In contrast, bands with higher intensity in the KO samples include 750 cm^{-1}, 1022 cm^{-1}, 1128 cm^{-1}, 1314 cm^{-1}, 1460 cm^{-1}, 1583 cm^{-1}, 1674 cm^{-1}. A more detailed overview of the peak assignments can be found in Table 17.

3.8.3 Lipids

3.8.3.1 PC-2 of Lipids

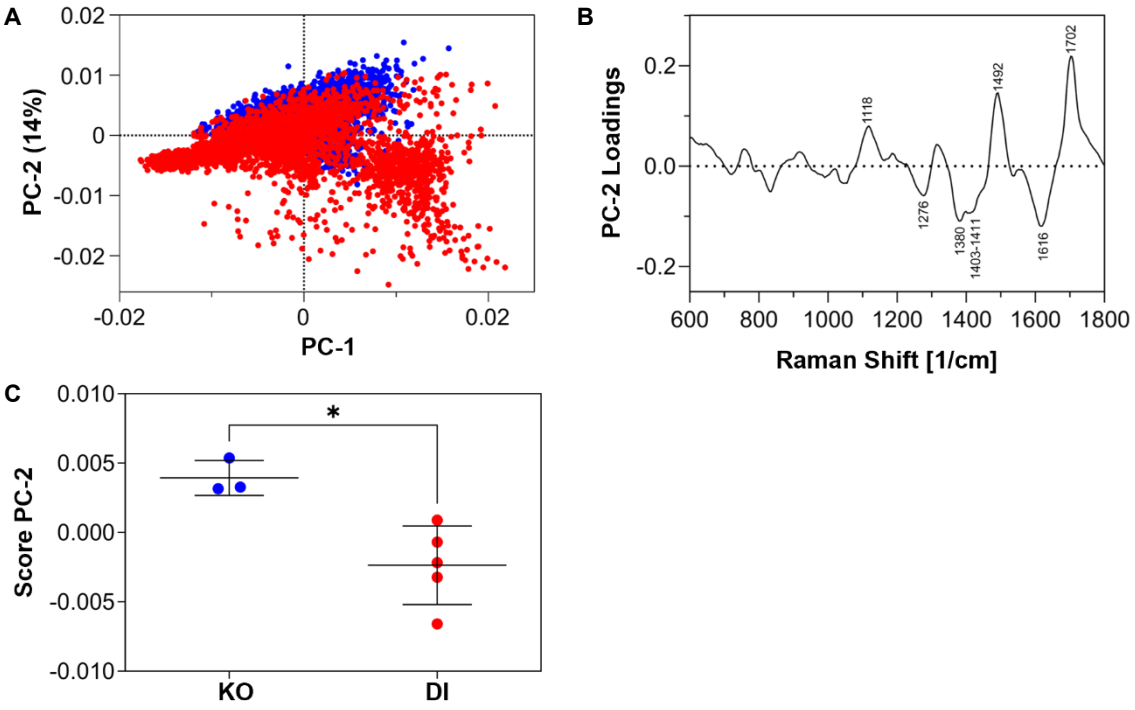

Figure 18 *PCA of Lipids PC-2*
Scores plot of PC-2 and PC-1 (A). Loadings of PC-2 (B). The characteristic wavenumbers are labeled. Two-tailed Mann-Whitney U test was performed to obtain the score value of PC-2 comparing the KO (blue) and DI (red) (C). KO n=3, DI n= 5. DI from LIS (n=3), SRV (n=1) and DGS (n=1).

Wavenumber (cm^{-1})	Assignment	References
(w) 1118	C-C stretch (ν(C-C))	[94, 156, 189]
(w) ~1270	Typical phospholipids; C=C groups in unsaturated fatty acids (FAs); δ_{ip}(=C-H) in an unconjugated cis double bond	[190]; [155]; [106, 191]
(m) 1379	ν(C=C) symmetric stretch	[181]
(sh) 1415	CH vibrations/rocking in lipids	[189]
(m) 1493	conjugated C=C vibrations	[189]
(s) 1699–1710	ν(C=O) carbonyl band in free fatty acids (FFAs)	[192]
δ_{ip} (in-plane deformation)		

Table 15 *Loadings of Lipids PC-2*

PC-2 accounts for 14% of the total variance in the dataset and reveals a clear separation between lipid-associated signals in DI and KO samples. The KO samples cluster towards the positive y-axis, while the DI samples are positioned towards the negative y-axis (Fig. 18 A). The corresponding loadings (Fig. 18 B) provide insight into the spectral features responsible for this separation.

The upward clustering of KO is primarily driven by spectral bands at 1118 cm^{-1}, 1493 cm^{-1} and 1699–1710 cm^{-1}. In contrast, DI tissues show relatively higher intensities at ~1270 cm^{-1} and 1415 cm^{-1}. For further details, refer to Table 15.

3.8.3.2 PC-7 of Lipids

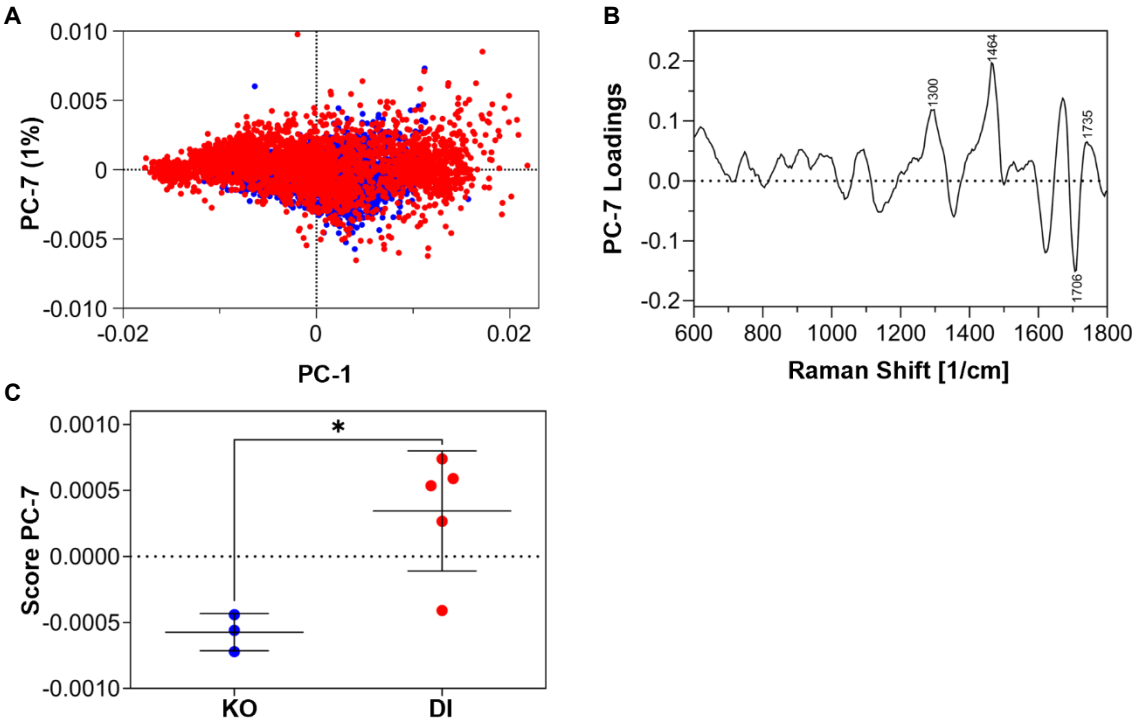

Figure 19 *PCA of Lipids PC-7*
Scores plot of PC-7 and PC-1 (A). Loadings of PC-7 (B). The characteristic wavenumbers are labeled. Two-tailed Mann-Whitney U test was performed to obtain the score value of PC-7 comparing the KO (blue) and DI (red) (C). KO n=3, DI n= 5. DI from LIS (n=3), SRV (n=1) and DGS (n=1).

Wavenumber (cm^{-1})	Assignment	References
(m) 1295	τ(CH_2) sphingomyelin	[156]
(s) 1464	β(CH_2/CH_3) in cholesterol and cholesterol esters	[156]
(s) 1626	symmetric stretching of conjugated dienes (oxidation products of polyunsaturated fatty acids (PUFAs))	[193]
(s) 1672	ν(C=C) sphingomyelin (Membrane lipids); Ceramide	[107, 156] [155]
(s) 1699 - 1710	ν(C=O) carbonyl band in FFAs	[192]
(m) 1741	ν(C=O) in cholesterol and cholesterol ester	[155, 156]

β (bending), τ(twisting)

Table 16 *Loadings of Lipids PC-7*

The score value of PC-7 (Fig. 19 C) also reveals a significant difference in the lipid-associated spectral profiles between DI and KO samples. In contrast to PC-2, PC-7 accounts for only a small proportion of the total variance of the data, namely 1%. The KO samples cluster along the negative y-axis, while the DI samples are positioned on the positive y-axis.

The corresponding loadings (Fig. 19 B) provide insights into the lipid-related spectral features driving this separation. The downward clustering of KO is mainly associated with Raman peaks at 1626 cm^{-1} and 1706 cm^{-1}. In contrast, DI samples exhibit stronger intensities at 1289–1297 cm^{-1}, 1464 cm^{-1}, 1672 cm^{-1} and 1741 cm^{-1}. For more detailed spectral assignments, refer to Table 16.

3.8.4 Collagen

3.8.4.1 PC-4 of Collagen

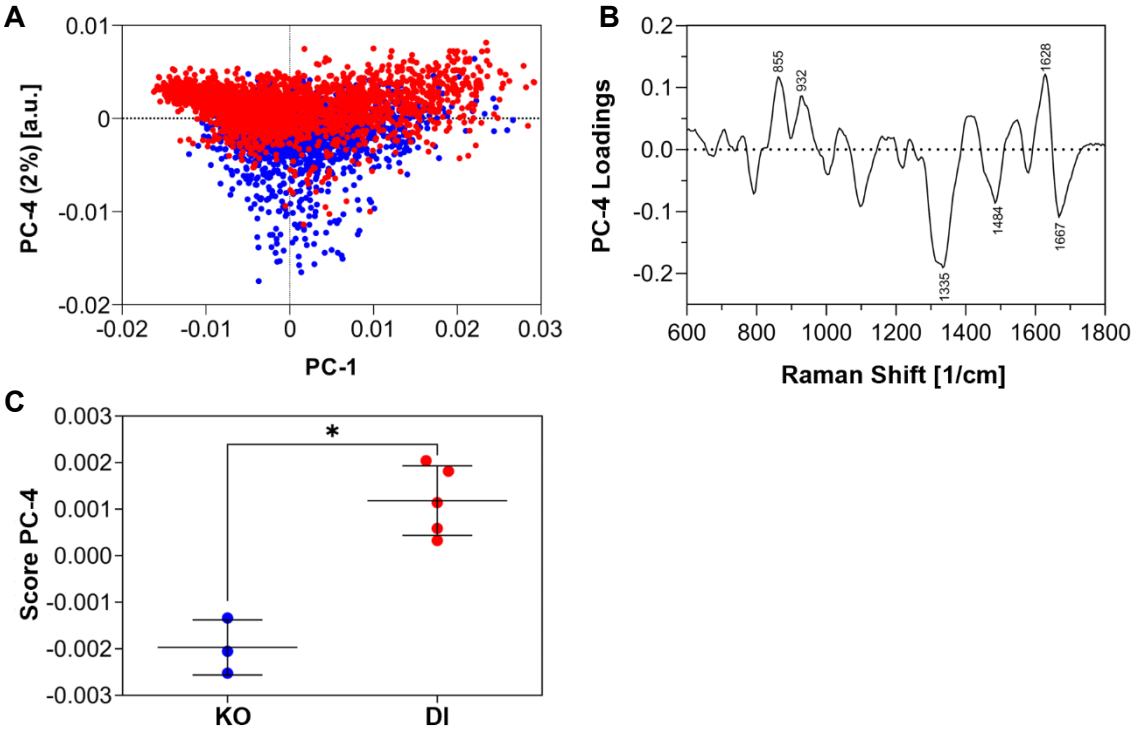

Figure 20 *PCA of Collagen PC-4*
Scores plot of PC-4 and PC-1 (A). Loadings of PC-4 (B). The characteristic wavenumbers are labeled. Two-tailed Mann-Whitney U test was performed to obtain the score value of PC-4

comparing the KO (blue) and DI (red) (C). KO n=3, DI n= 5. DI from LIS (n=3), SRV (n=1) and DGS (n=1).

Wavenumber (cm^{-1})	Assignment	References
(m) 855	ring breathing mode (δ(CCH)) of tyrosine and ν(C–C) of proline ring	[94, 163, 194]
(m) 932	ν(C-C), α-helix, proline, valine (proline/glycogen), collagen	[94, 163, 195, 196]
(s) 1335	ω(CH_3CH_2), collagen, COL IV, amide III	[94, 148, 161, 163, 197]
(m) 1484	amide II (largely due to a coupling of CN stretching, β_{ip}(N-H); δ_{as}(CH_3)	[164]
(m) 1628	Amide I band; α-helix/triple-helix (ordered helical structures)	[182-186]
(m) ~1674	Amide I disordered structure	[187, 188]
ω (wagging), δ_{as} (asymmetric deformation)		

Table 17 *Loadings of Collagen PC-4*

PC-4, which accounts for 2% of the total variance, reveals significant differences in the spectral signatures of collagen fibers between KO and DI samples (Fig. 20 B). The DI samples cluster along the positive y-axis, whereas the KO samples are shifted towards the negative y-axis.

The downward clustering of KO samples is mainly driven by spectral bands at 1335 cm^{-1}, 1484 cm^{-1}, and ~1674 cm^{-1}. In contrast, the upward clustering of DI samples is characterized by the peak pair at 855 cm^{-1} and 928 cm^{-1}, as well as a prominent band in the amide I region at 1628 cm^{-1}. For detailed spectral assignments, refer to Table 17.

3.8.4.2 PC-7 of Collagen

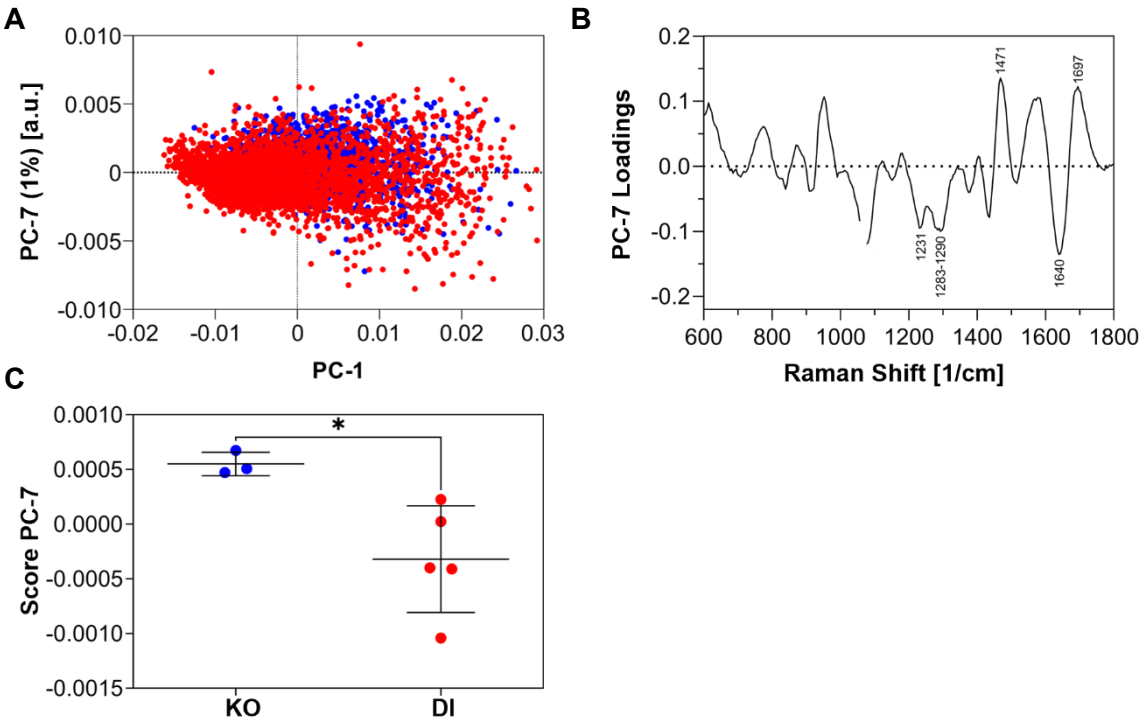

Figure 21 *PCA of Collagen PC-7*
Scores plot of PC-7 and PC-1 (A). Loadings of PC-7 (B). The characteristic wavenumbers are labeled. Score value of PC-7 for KO and DI (C). The blue dots represent the KO, while the red dots represent DI.

Wavenumber (cm^{-1})	Assignment	References
(m) 1231	β-strand in the secondary structure of polypeptides; Amide III: ν(C-N), β(N-H)	[198, 199]
(m) 1283-1290	Amide III: ν(C-N), β(N-H); Collagen, ω(CH_2) and the ν(C-N) of the cyclic proline side chain	[199, 200]
(s) 1471	Amide II (extended conformation); Amide II' (α-helix); $\delta_{as}CH_3$ in Leucine	[198, 199, 201-203]
(s) 1640	Amide I band (protein band); α-helix/triple-helix (ordered helical structures)	[182-186]
(s) 1697	Amide I (random coil)	[187, 204]

Table 18 *Loadings of Collagen PC-7*

The score values of PC-7 (Fig. 21 C) also show a significant difference between the collagen features in DI and KO. In contrast to PC-4, PC-7 describes only 1% of the total variance of the data. The KO samples cluster towards the positive y-axis, while the DI samples cluster towards the negative y-axis. The loadings (Fig. 21 B) provide insights into why the KO samples cluster upwards. Specifically, the spectral bands at 870 cm^{-1}, 952 cm^{-1} and 1697 cm^{-1} are mainly responsible for the upward clustering, whereas the bands at 1231 cm^{-1}, 1283-1293 cm^{-1}, and 1640 cm^{-1} contribute to the downward clustering of the DI (for further information see Table 18).

4 Discussion

4.1 Raman Imaging as a Complementary Technique for Histopathology

Both RMS and classical histopathology are well-established methods used in medical diagnostics and research. RMS has emerged as a promising complementary technique, offering several advantages over conventional histologic methods, which typically involve tissue sectioning and staining. In this section, the key differences, advantages, and limitations of both approaches are discussed in the context of tissue characterization and diagnostic application.

4.2 Advantages of RMS over Conventional Histology

RMS offers several advantages over conventional histologic staining methods, especially when working with sensitive materials or living cells. Unlike histologic techniques, which require fixation, sectioning, and staining, RMS is a label-free, non-destructive method that does not require any sample extraction or chemical treatment [205, 206]. This greatly simplifies the preparation process, reduces potential sample degradation, and saves time and laboratory resources [206].

RMS relies on the detection of the scattering of inelastic monochromatic light [205]. This allows for the analysis of tissues in their natural state, making RMS compatible with in vivo applications. Unlike techniques based on fluorescent or chromogenic labeling, RMS provides intrinsic molecular information without altering the sample. Additionally, due to the weak Raman scattering of water, RMS can be applied to aqueous or hydrated samples [205], making it particularly suitable for the analysis of biological tissues [206].

The ability to acquire data in real time with minimal sample manipulation makes RMS a valuable tool for dynamic or longitudinal studies [207, 208]. These features make RMS a powerful complement to conventional histology, particularly when molecular sensitivity, sample integrity, and rapid analysis are essential.

4.2.1 Insights at the Molecular Level

The high spatial resolution of RMS enables detailed visualization of subcellular structures, while its high molecular specificity facilitates the identification of

distinct components within a sample [1, 2]. By capturing cellular changes at the molecular level, RMS allows for a more precise characterization of pathologic processes than conventional histologic methods, which often fail to detect subtle biochemical alterations [209].

RMS is particularly valuable in oncology, where early molecular changes may precede visible morphological alterations. Yang et al. demonstrated that Raman-based analysis can distinguish malignant from benign breast tissue with high sensitivity and specificity [209]. These findings underscore the potential of RMS as a powerful diagnostic tool that can provide information beyond what is visible under a microscope.

4.2.2 Enhanced Diagnostic Accuracy

Research has indicated that RMS can outperform traditional histologic techniques in terms of sensitivity and specificity. By identifying specific molecular and biochemical changes, it is possible to precisely differentiate between healthy and diseased conditions [210], a feature that classical histology cannot achieve because it relies solely on morphological criteria. For example, a study on renal tumor characterization revealed that RMS was able to distinguish between malignant and benign tissue with high accuracy, surpassing classical histologic assessments [211].

In cancer diagnostics, on the other hand, Raman techniques can be used to identify tumor margins and types based on their unique spectral signatures, which has been shown to improve diagnostic accuracy in brain tumors [212]. Furthermore, the integration of machine learning algorithms with Raman data has enhanced classification accuracy, thereby supporting its potential as a routine diagnostic tool [213].

In the field of neurosurgery, RMS has demonstrated its ability to detect tumor infiltration in tissues that appear to be non-pathologic on standard histologic examination [214]. This not only enhances surgical precision but also facilitates the development of personalized treatment strategies based on the tumor’s biochemical profile.

4.2.3 Limitations of Raman Spectroscopy

Despite its numerous advantages, RMS presents several challenges. One major limitation is the low signal intensity of spontaneous Raman scattering, which often requires long acquisition times. Although advances in instrument development have partially addressed this issue, the sensitivity of Raman signals can still be affected by factors such as sample quality, preparation techniques, and interference from background fluorescence [215, 216]. Furthermore, the interpretation of Raman spectra is complex and often requires advanced data analysis techniques, such as multivariate statistical methods. This complexity of analysis represents an additional hurdle for the clinical translation and routine application of RMS [210].

4.2.4 Comparison with Classic Histology

Classical histology remains the gold standard for many pathologic examinations. Histopathologic staining enables the identification of tissue components in KO and DI samples. However, it is invasive and requires extensive sample preparation, mainly providing morphological information. Tissue samples must be fixed, cut, and stained. This irreversibly alters their original biochemical composition [217, 218]. These procedures are time-consuming, resource-intensive, and dependent on the experience of the personnel carrying them out [217, 218].

Another limitation is the reliance on subjective interpretation by pathologists, which can lead to inter-observer variability and increase the risk of inaccurate diagnoses, particularly in cases with subtle or ambiguous morphological changes [217, 218]. Furthermore, conventional staining methods lack molecular specificity. Although they can highlight certain tissue structures, they cannot reliably differentiate between molecular subtypes, as is the case with PSR staining, for example. As mentioned in Section 3.5, PSR provides information about the qualitative and relative measure of collagen organization [137]. However, additional complex or targeted techniques are required to specify collagen types [219].

Histologic approaches are inherently invasive, and are limited by the inability to obtain real-time molecular information from tissue samples. The reliance on subjective interpretation by pathologists further introduces variability and potential for diagnostic errors, particularly in cases of ambiguous morphological features [217, 218]. Moreover, tissues cannot be preserved in their native state as the original tissue structure is irreversibly damaged by the staining detergents. Histologic staining requires complex protocols and experienced laboratory staff. Additionally, the staining protocols are often time-consuming.

In contrast, RMS provides objective, label-free biochemical information directly from the sample in its near-native state. In this way molecular alterations that are invisible to standard histologic procedures can be detected and quantified [209]. This is particularly advantageous in oncology, where precise tumor classification, differentiation of subtypes and margin assessment are essential for treatment planning [212].

In the context of this study, RMS-based collagen analysis revealed differences in collagen composition and alterations in secondary protein structures in KO and DI samples, which might contribute to the persistence or even pathogenesis of endometriosis. In addition, the lipid analysis revealed an increased proportion of unsaturated lipids in DI samples compared to the KO samples. The ECs of the DI samples showed a greater content of ordered and stable protein structures, whereas KO samples exhibited a higher degree of structural disorder, which may influence their functional properties.

4.3 Future Directions

As Raman spectroscopy continues to evolve, its integration with artificial intelligence and machine learning is expected to further enhance its clinical applicability. RMS generally provides fast results, which facilitates the efficient analysis of large datasets. The development of automated systems for spectral analysis could provide consistent and objective diagnostic insights, reducing inter-observer variability associated with traditional histologic evaluations [220]. In addition, advances in probe technology and miniaturization of Raman systems are likely to facilitate wider application of these techniques in routine clinical

practice. Thus, RMS can serve as a complementary tool to the original histopathologic staining methods.

4.4 Endometriosis Is Associated with Altered (fibrotic) Collagen Fibers

The next tissue component analyzed in this study to identify differences between KO and DI was collagen. Collagen is an important structural protein and major constituent of the ECM [221]. It plays a central role in both physiological tissue homeostasis and pathologic remodeling.

Jiang et al. indicated that inflammation plays a pivotal role in the condition of endometriosis [222]. Chronic and/or uncontrolled inflammation can lead to fibrotic tissue remodeling over time [161, 223, 224]. In fibrotic processes, excessive deposition of connective tissue in ECM can be observed, resulting in increased tissue stiffness [223, 225]. One of the main components of the ECM is collagen [226]. Fibrotic ECMs are characterized by an excessive accumulation especially of the fibrillar COL I, COL III [227] and fibronectin, synthesized by activated fibroblasts and myofibroblasts [228].

To evaluate collagen organization, we performed quantitative analysis of PSR staining under polarized light microscopy. This method visualizes collagen fibers based on their birefringence properties, which are influenced by physical characteristics such as fiber thickness, bundling, packing density, and orientation - rather than their biochemical composition [134-137, 229]. Although the color classification defined by Rich et al. is still a matter of debate, it is widely accepted that PSR is based on birefringence [134].

In our study, significant differences were observed between KO and DI samples across all color categories. KO tissue exhibited a predominance of green and yellow birefringent collagen fibers, which likely reflects thinner, less organized collagen fibers. This may be explained by the physiological cyclic degradation and subsequent regeneration of the endometrium. During the proliferative phase of the menstrual cycle, the previously shed stratum functionale is rebuilt, which includes the de novo synthesis of collagen fibers. Becker and Beyer et al. demonstrated that the transition to ovulation and the secretory phase is marked by a simultaneous increase in orange and red fibers and a decrease in green and

yellow fibers. [221]. The loss of previously formed collagen fibers occurs during subsequent menstruation, initiating a new cycle [221].

The DI samples were analyzed in the same menstrual phase as the KO samples. However, in DI, the collagen fibers in the stroma surrounding the ectopic glands exhibited a predominance of orange and red birefringence. This may indicate that the collagen fibers in DI stay unaffected by the cyclic remodeling observed in the eutopic endometrium. Additionally, the chronic inflammatory milieu of DI lesions may promote fibrotic remodeling. Fibrotic remodeling of the ECM is associated not only with increased collagen fiber maturation, but also with their alignment. The parallel alignment of myofibroblasts is crucial for the synthesis of collagen fibers. These resulting parallel collagen fibers lead to increased tissue stiffness [221].

We further compared our three DI subtypes (LIS, DGS, SRV). Significant differences were primarily observed in the red and orange fiber categories – those associated with stronger birefringence [134, 135]. These discrepancies may result from differences in the local tissue microenvironment, mechanical stress, and variability which may contribute to the observed heterogeneity.

While PSR staining effectively visualizes collagen fiber organization via birefringence, it does not allow for the identification of specific collagen types. Matsuzaki et al. reported that COL I predominates in the stroma of ectopic glands, underscoring its crucial role in fibrosis associated with peritoneal endometriosis [230]. To obtain a more detailed biomolecular analysis of collagen fibers, more specific techniques such as RMS are employed. For instance, Becker et al. used RMS to investigate the excessive deposition of COL I during fibrotic ECM remodeling [161].

We also analyzed all our samples with RMS to gain deeper insights into the molecular changes of collagen fibers in the KO and DI. Our PCA results identified two significant PCs, PC-4 and PC-7, with PC-4 accounting for 2% of the variance and PC-7 for 1%.

Although both PCs accounted for a smaller portion of the variance and did not highlight the greatest differences between KO and DI, analyzing their loadings plots may still provide valuable insights. The collagen features contributing to the separation in PC-4 and PC-7 must be interpreted with caution as they describe less significant differences compared to lower-numbered PCs (e.g., PC-1 and PC-2).

In the loadings of PC-4, an altered molecular composition of collagen, particularly regarding its secondary structure, was observed between KO and DI. The following section discusses the relevant peaks and their possible meanings in relation to the tissues studied. Spectral shifts were observed in the PC-4 loadings, including the characteristic peak pair at ~855-870 cm^{-1} and ~930-950 cm^{-1}, as well as a peak at 1335 cm^{-1}, the amide III region (1200-1300 cm^{-1}), the amide II region (1470-1575 cm^{-1}) and the amide I region (1650-1700 cm^{-1}).

Typical secondary structures of proteins include the α-helix, β-sheet, loops, and turns. The α-helix is a frequently occurring structure in proteins. It is a rigid, tightly packed, right-handed helical structure that is stabilized by hydrogen bonds [231]. These bonds form between the carbonyl groups (-C=O) of each peptide bond and the N-H groups of the peptide bonds [231]. Only a single polypeptide chain is needed to form an α-helix [231]. The β-sheet structure is looser and less densely packed compared to the α-helix [231]. It consists of adjacent β-strands that are stabilized by hydrogen bonds between them. These β-strands can occur in parallel or antiparallel orientations. Several (at least two) polypeptide chains are required to form a β-sheet [231]. The β-sheet structure is highly versatile, contributing to various functions in proteins such as enzymes, antibodies, transport proteins, membrane proteins, and viral envelopes [231]. Loops and turns are flexible regions that connect the α-helices and β-sheets. Turns are shorter segments that cause sharp directional changes in the polypeptide chain [232]. These regions are important for the overall folding and function of proteins [232].

The characteristic peak pair at ~855 cm^{-1} and 932 cm^{-1} shows increased signals in endometriosis. The spectral shift at ~855 cm^{-1} can be attributed to the ν(C-C)

of the proline ring and the ring breathing mode (δ(CCH)) of tyrosine [94, 163, 194], while the peak at 932 cm^{-1} can be assigned to the ν(C-C) of the α-helical protein (proline, valine) [94, 163, 195, 196]. The peak at ~855 cm^{-1} indicates changes in the structural components of the amino acids proline and tyrosine. Proline along with hydroxyproline and glycine is a crucial amino acid in collagen [200, 233]. Similarly, the peak at 932 cm^{-1} highlights alterations in the secondary structure of collagen. Becker and Lu et al. assigned the characteristic peak pair at 855 and 936 cm^{-1} - indicative of proline - to COL I [161]. They also noted that COL IV shared many spectral features with COL I but exhibited increased signal intensity at 1335 cm^{-1}, which will be discussed in the next paragraph [232]. The increased signals observed at the characteristic peak pair imply that the molecular composition and structural integrity of collagen fibers are altered in endometriosis. α-helices are rigid and tightly packed [231], and generally regarded as highly ordered structures. The conformation of proteins may be altered in pathologically modified tissue. The increased signals observed in this characteristic peak pair indicate that the molecular composition and structural integrity of collagen fibers are altered in DI.

The CH_3CH_2 wagging mode of COL IV, observed around 1335 cm^{-1}, is more pronounced in KO samples [94, 148, 161, 163, 197]. Studies have shown that normal epithelial tissues exhibit characteristic collagen bands at 1031, 1204, 1282, and 1337 cm^{-1}. In contrast, many malignant epithelial tissues lack these collagen-related peaks. This has been attributed to the degradation of the epithelial basement membranes (BMs) and the surrounding stroma by invasive cancer cells [234].

Evers and Willebrand et al. investigated the status of the BM in endometriosis. Since the BM is mainly comprised of COL IV, laminin, and acetyl heparin sulfate proteoglycan [235], they used a specific COL IV antibody staining to show that all endometriotic lesions, regardless of their location, were surrounded by a continuous, intact BM [236]. However, recent studies have shown that endometriotic lesions may grow through mechanisms similar to peritoneal metastasis, including BM invasion [237]. Furthermore, E-cadherin-negative, N-

cadherin-positive endometriotic ECs exhibited invasive growth in vitro [237]. D'Alterio et al. also described the invasion of the BM in cases of deeply infiltrating endometriosis of the ureter [238].

In the present study, the spectral peak at 1335 cm^{-1} could therefore indicate a difference in the integrity of the BM between normal endometrial tissue and endometriosis. The presence of this peak in normal endometrial tissue indicates an intact BM, whereas its change or absence in endometriotic tissue may reflect BM disruption or invasion, which is consistent with the observed invasive behavior of the previously cited studies of endometriotic lesions.

Further spectral shifts observed in the PC-4 loadings were found in the amide I, II and III regions. The individual amide bands each provide unique insights into the structural and conformational properties of the protein [239], as they correspond to distinct vibrational modes within the protein's peptide backbone [240]. Therefore, they can provide valuable information about the secondary structure and dynamics of proteins. The amide III region, which is characterized by in-plane N-H deformations (δ(NH)) in combination with C_α-N stretching, occurs in the spectral range of ∼1230–1340 cm^{-1} [239]. The amide II region, which primarily results from the out-of-phase combination of in-plane N-H deformation and a small amount of C_α-N stretching, is found in the range of ~1450-1575 cm^{-1} [198, 199, 201, 202, 239]. The amide I mode, which mainly results from C=O stretching vibrations (ν(C=O)) of the peptide backbone and in-plane deformations (δ(NH)) of the secondary structure of peptides or proteins [186, 199, 241], is localized in the spectral range at ∼1630–1700 cm^{-1} [187, 199, 239].

We identified a peak in the amide II region at 1484 cm^{-1}, which was shifted towards the KO. The amide II band is more complex than the amide I band [202]. Although it is rarely used for structural studies [7] due to interference from amino acid side chain vibrations and its weakness in the Raman spectrum [199], the amide II band can still provide valuable structural information about the secondary structure of polypeptides [201, 242].

The spectral band 1445-1480 cm^{-1} can be assigned to the antisymmetric deformation vibration of methyl groups (-CH_3) ($\delta_{as}(CH_3)$) [242]. An increased signal in this region may reflect a higher content of amino acids with methylated side chains (AA-M), such as alanine, valine, leucine, isoleucine, and methionine [243, 244]. These amino acids share hydrophobic methyl groups that tend to associate with each other rather than interacting with water [244]. This, in turn, stabilizes the three-dimensional structure of water-soluble proteins. The different sizes and shapes of their hydrocarbon side chains allow for a compact arrangement with few gaps [244]. Based on the results on the PCA, we assume that KO samples contain a relatively higher proportion of water-soluble proteins with a stable three-dimensional structure compared to DI samples.

Alternatively, the increased signal at $\delta_{as}(CH_3)$ may also indicate increased protein methylation, which plays a role in gene expression, protein-protein interactions, subcellular localization, and cellular signaling pathways [245]. However, further validation is required to confirm this interpretation.

In the spectral range of the amide I band, we identified two major bands: one at 1628 cm^{-1} which was more pronounced in the DI, and another at ~1674 cm^{-1} which was shifted towards the KO. The amide I region is most commonly used for structural studies as it is highly sensitive to small changes in molecular geometry and hydrogen bonding of the peptide group [199]. The amide I band can be roughly subdivided into three secondary structures: turns (1635-1640 cm^{-1}), α-helix (1650-1655 cm^{-1}), β-family (1665-1670 cm^{-1}), and random coil above 1670 cm^{-1} [187].
The amide I band at 1628 cm^{-1} can be attributed to ordered helical structures [182], such as the triple-helix [182, 186]. The amide I band at ~1674 cm^{-1} represents a rather disordered secondary structure (random coil [187]) with a lack of hydrogen bonds [204].

These findings suggest that the DI samples exhibit a more ordered and stable protein structure, while KO samples show increased structural disorder, which could have implications for their functional properties. These observations may

be explained as follows: During the menstrual cycle, the endometrium undergoes phases of growth, differentiation, detachment, and reconstruction [246]. This dynamic process requires flexible and adaptable protein structures, which could lead to a higher content of disorganized secondary structures. Additionally, the high metabolic activity in the endometrium and the extensive ECM remodeling [246], involving the degradation and synthesis of various structural proteins, especially during phases of rapid growth and tissue repair, may result in the accumulation of unfolded or partially folded proteins that have not yet fully adopted their final ordered configuration, contributing to the observed disordered secondary structures. Furthermore, hormonal fluctuations during the menstrual cycle may influence protein folding and stability, potentially leading to a temporary increase in disordered protein structures during certain phases of the cycle.

Explanations for the higher content of ordered helical structures in endometriosis may lie in the repeated damage or inadequate healing, resulting in an overaccumulation of collagen and other ECM proteins around inflamed or impaired tissue, leading to permanent scarring, disruption of tissue structure, and potentially also organ dysfunction [247] (e.g., dysfunction of the fallopian tubes due to scarring, endometriomas [248]). Garcia et al. described several fibrotic mediators that contribute to this excessive accumulation and thus play a crucial role in the development and progression of fibrosis in all types of endometriosis [247]. A key component of the ECM is collagen, characterized by a triple helical structure consisting of three intertwined polypeptide chains [249]. This collagen triple helix follows a repeating amino acid sequence (Gly-X-Y)n, where X normally stands for proline and Y for hydroxyproline [186]. Accordingly, the above-mentioned amplified spectral intensities of the characteristic peak pair for collagen at ~855 cm^{-1} and 932 cm^{-1}, which can be assigned to collagen, may support this thesis.

Stone et al. investigated the spectral profiles of four different neoplastic tissues (esophagus, colon, breast, and prostate) [94]. They found that neoplastic tissues had a higher content of β-sheet proteins and disordered protein structures, while non-neoplastic control tissues showed an increased proportion of α-helical

proteins [94]. Our results differ from their findings. In the endometriosis samples, we identified peaks indicative of α-helical proteins, whereas in the healthy endometrial samples, we observed peaks indicative of disordered protein structures. It should be emphasized that the benign control tissues analyzed in Stone's study differ fundamentally from the endometrium, which undergoes monthly degradation, regeneration, and remodeling [250]. Regarding the higher content of α-helical proteins in the DI, it is important to mention that although endometriosis has typical features of cancer, such as the presence of oncogenic driver mutations, invasive potential and the ability to metastasize, it is not considered a malignant disease [251]. Chui et al. proposed referring endometriosis as a "benign" neoplasm [251]. A major difference to malignant diseases is that endometriosis is not lethal [225].

Moving on to the results of the PC-7 loadings. Care should be taken when interpreting the PC-7 collagen loadings as they only account for 2% of the variance. The reported differences could just as easily represent noise or artifacts.

The loadings of PC-7 showed two elevated spectral bands in DI in the amide III region (1230–1300 cm^{-1}) that can be assigned to C-N stretching and N-H bending. The peak at 1231 cm^{-1}, sensitive to β-strand/β-sheet structures in the secondary structure of polypeptides [198, 231] and the spectral range between 1283 -1290 cm^{-1}, which can be assigned to CH_2 wagging vibration from the glycine backbone and proline side chains [164, 200] or the α-helix conformation of polypeptides or proteins [94, 198], depending on the literature [190].

Cárcamo et al. also described two spectral peaks (1248 and 1271 cm^{-1}) occurring in the amide III region. They hypothesised that the two peaks occurring in collagen may be related to the biphasic nature of the tropocollagen molecule along the chain (proline-rich (non-polar) and proline-poor (polar) regions) [60]. Our peaks are somewhat shifted, with the peak at 1248 cm^{-1} appearing at 1231 cm^{-1} and the peak at 1271 cm^{-1} appearing at ~1283–1290 cm^{-1} [252].

The most striking difference between collagen and other proteins is the high proportion of glycine, proline and hydroxyproline residues [200, 233]. Jackson et al. hypothesized that these two amino acids are responsible for the spectral properties of collagen in the range of 1200–1400 cm^{-1} [200]. They attributed the increased intensity of the amide III absorption to the unusual nature of the glycine and proline side chains, which could lead to an atypical collagen structure [200]. Additionally, the mixing with the CH_2 wagging vibration and the C-N stretching vibration of the cyclic proline side chain may also contribute to the intensity in this spectral region [200].

Andrus and Strickland et al. also assigned this spectral range to collagen and found that collagen-like scarring seems to be a major product of chronic inflammation [234]. They observed an increased absorption in the 1200-1700 cm^{-1} range in inflamed tumor tissue [234]. Pronounced alterations in the amide III region due to the transition from normal to inflamed tissue were also observed by Malini et al. [190]. Inflamed tumors exhibit changes in the secondary protein structure within this spectral range, comparable to those seen in malignant tumors [234]. These changes are thus likely due to the functional or biosynthetic activity of the cells, rather than being specific to malignancy [234].

The results of these studies are consistent with our findings. Since endometriosis is associated with an inflammatory process [253], the peaks we observed in the amide III region (at 1231 cm^{-1} and 1283–1290 cm^{-1}) are shifted towards DI.

Peaks contributing to the downwards shift on the KO are found in the amide II region at 1471 cm^{-1} and 1484 cm^{-1}. Wolpert and Hellwig et al. attributed the peak at 1471 cm^{-1} to the asymmetric deformation of CH_3 ($\delta_{as}(CH_3)$) in the aliphatic amino acid leucine [203]. Dutta et al. demonstrated that the levels of the amino acids' alanine, lysine, phenylalanine and leucine were significantly lower in the endometrial tissue of women with endometriosis compared to healthy controls [254]. This decrease is attributed to the physiological mechanism of tissue damage and repair in endometriosis [254]. In response to the tissue damage, there is an increased breakdown of the body's own proteins, which leads to the

release of free amino acids into the bloodstream [254]. This consequently leads to a reduction in the content of amino acids in the tissue with a simultaneous increase in their content in the bloodstream [254]. This could therefore explain a relatively lower proportion of leucine in the endometriosis tissues and thus the shift of the spectral peak in the direction of the endometrium. Our results can be reconciled with these findings, as this peak is relatively more pronounced in our healthy KO.

To conclude, distinct peaks differentiating collagen features from KO and DI were identified in the PC-4 and PC-7 loadings (Fig. 22/23 B). Spectral shifts observed in DI at ~855 cm^{-1} and 932 cm^{-1} indicative for the amino acid proline can be attributed to COL I [161]. In contrast, increased intensities for COL IV (~1335 cm^{-1}) were found in the KO-derived spectra [94, 148, 161, 163, 197]. Additionally, increased intensities were observed in the amide II band (1448 cm^{-1}, 1471 cm^{-1} and 1484 cm^{-1}) [198, 199, 201-203, 239] and in the amide I region for disordered secondary structures [187]. Spectral shifts towards DI were found in the amide I region for ordered helical structures [182, 186] and the amide III region [164, 198, 200, 231].

These findings suggest that collagen remodeling in endometriosis involves not only an increased deposition of COL I but also significant changes in the structural organization of collagen. This increased deposition may contribute to the development of a more fibrotic and structurally rigid ECM, which is a key factor in the pathologic fibrosis [255] observed in endometriosis. The chronic and cyclically repeated tissue damage associated with endometriosis may further aggravate this process and lead to a progressive accumulation of ECM components [247]. This, in turn, results in persistent scarring, disruption of normal tissue architecture, and, in severe cases, organ malfunction [247]. For instance, endometriosis can lead to scarring of the fallopian tubes and thus to their dysfunction. In addition, alterations in secondary protein structures could further impair tissue function, contributing to the persistence and progression of the disease. In addition, alterations in secondary protein structures have been observed in endometriosis. Similar structural changes are known from several

neurodegenerative diseases, including Alzheimer's disease, Parkinson's disease, and amyloidosis [256]. These changes often involve an abnormal conformational transition from the typical α-helical structure to β-pleated sheet configurations that expose hydrophobic amino acid residues and promote protein aggregation, which can impair normal cell function [256]. Although the exact mechanisms involved in endometriosis are not yet fully understood, these observations suggest that altered secondary structures may significantly impair tissue function and contribute to the persistence and progression of endometriosis through mechanisms similar to those found in neurodegenerative diseases.

4.5 Altered Lipid Composition in Endometriotic Glands

Various studies in the literature have reported on the role of altered lipid composition in endometriosis. Marchandot et al., for example suggested a strong association between endometriosis and an elevated atherogenic lipid profile, systemic inflammation, increased oxidative stress, and endothelial dysfunction [257]. Mu et al. stated that women with laparoscopically confirmed endometriosis had an increased risk of hypercholesterolemia and hypertension, compared with women without endometriosis, and conversely, women who had hypercholesterolemia had a higher risk of subsequent laparoscopically confirmed endometriosis [258]. The Japan Nurses' Health Study reinforced these observations by indicating that women with endometriosis have a 30% increased chance of experiencing elevated cholesterol levels [257]. Melo et al. also highlighted the unfavorable lipid profile observed in endometriosis patients [259]. Although all lipoproteins were elevated in women with endometriosis, the difference was most pronounced for LDL levels, which were 38% higher in women with endometriosis compared to the control group [259]. Total cholesterol and triglycerides were also elevated in this group compared to controls [259]. While systemic lipid changes in endometriosis are well documented by blood-based analysis, RMS also offers the possibility to directly examine the lipid composition in the tissue. This direct tissue analysis enables a more detailed understanding of lipid distribution and its potential impact on the pathology of

endometriosis. In this way, knowledge can be gained on a new level that is not possible through systemic blood tests alone.

In this study, we were able to detect lipid-related differences between KO and DI using RMS. A total of seven main components were calculated in the analysis and their value plots were analyzed. PC-2 and PC-7 showed significant results. PC-2 explains 14% of the total data variability, whereas PC-7 accounts for only 1%, suggesting that the latter may primarily reflect noise or artifacts. To identify and understand the key features underlying for the differences in lipid composition of KO and DI, the following analysis therefore focuses primarily on the loadings plot of PC-2.

Increased spectral intensities correlating to endometriosis were observed at 1270 cm^{-1} (ν(C-C)) [94, 156] and 1379 cm^{-1} (C=C groups [155, 181] and an in-plane =C-H deformation in an unconjugated cis double bond (δ_{ip}(=C–H) *cis)* [106, 191]) which can be associated with an unsaturated FA chain [155, 181] in typical phospholipids [190].
In the body, lipids serve as the fundamental components of cell membranes and as energy stores. The most prominent types of membrane lipids include phospholipids, glycolipids and cholesterol [191, 260]. These lipids are amphipathic, meaning they have both hydrophobic and hydrophilic parts. The typical structure of lipids consists of FAs - carboxylic acids with hydrocarbon chains of varying lengths and a carboxyl group at the end [191, 260]. Unsaturated FAs contain one or more double bonds in the hydrocarbon chain, usually in a cis-configuration, their double bonds are not conjugated, as they are separated by one or more methylene groups (-CH2-) [191, 260].

Sadeghi-Jorabchi et al. introduced innovative quantitative models to assess the degree of unsaturation in FAs. One method involves calculating the intensity ratio of a band near 1270 cm^{-1} to the band at 1300 cm^{-1}. Additionally, these models help determine the ratio of cis to trans isomers and the number of double bonds in hydrocarbon chains [106]. They attributed the peak at 1272 cm^{-1} to the in-plane

deformation of the =C-H bond in a non-conjugated cis double bond (δ_{ip}(=C–H) *cis*) [106, 191]. Cis FAs are essential for the function of cell membranes. The cis-configuration of the double bonds in unsaturated FAs leads to bends in the FA chain [261]. Such bends influence the structure and functionality of biological membranes. In contrast to unsaturated FAs, saturated FA chains can form tight bonds [261]. Unsaturated FAs, on the other hand, form flexible, liquid aggregates [261]. Unsaturation leads to an increase in chain spacing, which results in increased membrane flexibility and reduced membrane rigidity [261]. Koster et al. pointed out that spectral peaks can represent several chemical entities, for example the peak at 1271 cm^{-1} can be assigned to amide III binding vibrations in extracellular vesicle proteins, while at the same time it represents C=C bonds in FAs and aliphatic chains [189].

Malini et al. claimed that the spectral range of 1200-1800 cm^{-1} shows differences between normal and malignant tissues, while in the range of 900-1400 cm^{-1} differences between malignant, premalignant and inflammatory conditions can be observed. For typical phospholipids, which show almost no contribution from proteins, spectral peaks are seen at 1750 cm^{-1} (C=O), 1650 cm^{-1} (C=C), 1440 cm^{-1} (strong CH_2 bend), 1330 cm^{-1} and 1270 cm^{-1} as well as a broad peak at 1080 cm^{-1} [190].

Independently, Krafft et al. also found that the Raman spectra of phosphatidylcholine (PC), phosphatidylserine (PS) and phosphatidylinositol (PI) show spectral bands at 1270 and 1660 cm^{-1}, which are characteristic of C=C groups in unsaturated FA chains [155]. They discovered that spectral bands of saturated and unsaturated FA chains are dominant in the range of 1000 - 1700 cm^{-1}. The high intensity of the spectral bands allows quantification of the total lipid concentration in lipid-containing biological material [155].

To summarize, the two spectral peaks in our PC-2 loadings can be assigned to unsaturated FAs found in phospholipids, indicating an altered composition of cell membranes in endometriosis that may influence their flexibility and fluidity [261].

Cellular membranes form the boundaries between living cells and their organelles [262]. Lipids are constantly being added to and removed from these membranes, which is why they can be described as dynamic structures [262]. Cell membranes play a crucial role in cellular communication and function. Higher membrane fluidity indicates a greater need for structural changes [262]. There is a correlation between membrane fluidity, cell function, and development and the respective cell type [262]. Changes in membrane fluidity have also been observed in certain types of cancer [262]. For example, the cells can adapt to new requirements through increased permeability [262]. In lung cancer, membrane fluidity can serve as a prognostic tool, as it influences the colonization potential of the lung, metastasis and the motility of the tumor cells [262]. Chen et al. also observed increased membrane fluidity in cancer tissue, which resulted in a facilitated transmembrane molecule transport and metabolism [181]. Ammendolia et al. stated that changes in membrane fluidity may weaken membrane resistance in the event of subsequent damage [263].

In the loadings of PC-2, the spectral peaks at 1118 cm^{-1} and 1493 cm^{-1} are more pronounced in the endometrium, while the peak at 1415 cm-1 is more prominent in endometriosis. These peaks represent C-C stretching vibrations (ν(C-C)) [94, 156], conjugated C=C vibrations [189] and CH rocking/vibration in lipids, respectively.

Koster et al. stated that the peaks at ~1118 cm^{-1}, 1188 cm^{-1} (C-C or C-O, e.g., phospholipids), 1415 cm^{-1}, and 1493 cm^{-1} are strongly represented in very low-density lipoproteins (VLDL), low-density lipoproteins (LDL), and chylomicrons, while they are less represented in high-density lipoproteins (HDL). The analysis of spectral peaks can provide useful information about the lipid composition of various lipoproteins and give insights into different chemical structures [189].

The main categories of lipoproteins are chylomicrons, VLDL, intermediate-density lipoprotein (IDL), LDL and HDL [264]. VLDL transport triglycerides, cholesterol, and proteins from the liver to peripheral tissues for energy use, essential bioactivities or storage [264, 265]. LDL deliver cholesterol to cells throughout the body, essential for cell membrane structure and hormone

synthesis. Chylomicrons carry dietary triglycerides and cholesterol from the intestines to the liver and other tissues [264]. HDL collect excess cholesterol from tissues and transport it back to the liver for excretion [265].

Elevated levels of VLDL, LDL and chylomicrons in the endometrium can lead to an increase in triglycerides and cholesterol and ensure hormone synthesis. In the proliferative phase, these components may be required to support appropriate cell proliferation and growth. The ectopic endometrial cells also require sufficient energy to keep themselves alive and possibly even to continue to grow.

The loadings of PC-2 show a peak at 1699-1710 cm^{-1}, indicating a carbonyl band position (ν(C=O)) [192], which is higher in the endometrium.

Spectral analysis of pure compounds allowed for clear discrimination between FFAs and other similar moieties based on the carbonyl band position (1699–1710 cm^{-1} range) [192]. Wrobel et al. reported that the identification of the shift of the C=O carbonyl band within the ester group enables the detection of various lipid groups, including cholesteryl esters, triglycerides and FFAs. The shift in band position from amide I (1680 cm^{-1}) to higher wavenumbers (1710-1750 cm-1) can therefore be considered a lipid-specific marker [192]

The position of the carbonyl band corresponds to the structure of the compound. The upper position (above 1740 cm^{-1}) of the C=O stretching band can be attributed to triglycerides, while the middle region (1715-1740 cm^{-1}) consists mainly of cholesteryl ester signals and the lower region (1699-1710 cm^{-1}) falls within the range of FFAs [192]

This would imply that more FFAs are found in the endometrium compared to endometriosis [13]. This correlates with the previous findings that the endometrium needs the energy from the FFAs to have sufficient energy to grow, differentiate, and prepare for potential implantation.

The PCA results for PC-7 must be interpreted with caution, as PC-7, as already mentioned, only accounts for about 1% of the data.

The spectral peaks at 1295 cm^{-1} ($\tau(CH_2)$) [158] and 1670 cm^{-1} ($\nu(C=C)$) [107, 156] were elevated in endometriosis and can be linked to the membrane lipid sphingomyelin [156]. The peak at 1670 cm^{-1} can also be assigned to ceramide [155]. Sphingomyelin is a sphingolipid that is particularly abundant in the plasma membrane and plays a crucial role in maintaining the integrity of the cellular membrane [156].

Sphingolipids are involved in many intracellular functions and inflammatory processes [266]. They regulate endothelial and vascular integrity and function [266]. Changes in these sphingolipids are associated with vascular dysfunctions and chronic inflammatory states [266]. Lee et al. found an enrichment of (glucosyl)ceramide and an accumulation of very long-chain monounsaturated sphingolipids (sphingomyelin, ceramide and glucosylceramide) in endometriotic lesions [267]. They suggested that the main source of ceramide is through the hydrolysis of sphingomyelin rather than de novo synthesis [267]. Lee et al. also observed that sphingosine-1-phosphate receptors were upregulated in both ectopic and eutopic endometrium [267]. The reduced response to the apoptosis-inducing effect of ceramide suggests cellular dysregulation leading to increased cell proliferation and the growth of endometriotic lesions [267]. Marchandot et al. found that elevated ceramide levels affect not only apoptosis and cell growth, but also the formation of reactive oxygen species, possibly leading to fertility problems in affected women via oocytotoxicity [257].

Spectral peaks, which were also higher in DI compared to KO, appeared at 1464 cm^{-1} ($\beta(CH_2/CH_3)$) and 1741 cm^{-1} ($\nu(C=O)$). They can both be assigned to cholesterol and cholesterol esters [156].

As previously mentioned, various studies have linked an altered lipid composition, including hypercholesterolemia, to endometriosis [257-259]. A disruption of cholesterol (CHL) levels can also be associated with various other diseases, such as cardiovascular disorders, Huntington's disease, and Alzheimer's disease [156]. It should also be noted that CHL is of enormous biological importance due to its role as a component of the cell membrane [156]. Its most important functions are to provide adequate stabilization and fluidity and

to control membrane permeability [156]. In addition, CHL is crucial for lipid metabolism and serves as a precursor for numerous biologically active compounds [156]. CHL can exist in various forms, including free form, esterified form (cholesterol esters) and as part of lipid-protein complexes (lipoproteins such as HDL and LDL) [156].

Czamara et al. observed changes in lipid distribution and composition in inflamed endothelial cells, identifying two subtypes of lipid structures: one rich in saturated lipids and cholesteryl esters, and the other primarily containing unsaturated lipids and cholesterols [268]. A significant increase in unsaturated lipids and cholesterols was found in the lipid bodies within inflamed cells' cytoplasm [268]. These lipid bodies showed co-localization of unsaturated lipids and cholesterols, indicating that the produced lipids are cholesteryl esters [268]. This is consistent with our observations of higher amounts of cholesterol ester bonds in endometriosis.

The two peaks that are higher in the KO are located at 1626 cm^{-1} (symmetric stretching of conjugated dienes (oxidation products of PUFA)) [193] and 1699–1710 cm^{-1} (ν(C=O) carbonyl band position (in FAA)) [192]. The latter was also found in PC-4.

Killeen et al. described an elevated spectral peak at 1626 cm^{-1} and attributed this band to the symmetric stretching of conjugated dienes, which are generally recognised as oxidation products of PUFA [193]. Acute inflammation is characterised by changes in lipid peroxidation levels, particularly by primary products such as conjugated dienes [269]. Conjugated dienes are recognised as toxic metabolites that can affect lipoproteins, enzymes and nucleic acids [269]. Extensive conjugation may be associated with increased molecular polarisability and thus increased Raman activity [193]. They concluded that the peak at 1626 cm^{-1} could be useful for identifying the oxidation of PUFA [193].

In fact, this peak better matches the inflammatory environment in endometriosis. In the endometrium, the peak at 1626 cm^{-1} may indicate a modulated inflammatory response. Conjugated dienes could, for example, regulate the

production of cytokines and chemokines, which are crucial for the recruitment and activation of immune cells during the menstrual cycle.

To conclude, this section highlights the lipid-related differences observed between KO and DI samples, with particular emphasis on the role of membrane lipids (sphingolipids), cholesterol, and conjugated dienes. Elevated levels of membrane lipids such as sphingomyelin and ceramide in the DI samples may indicate a link between cellular dysregulation and chronic inflammatory conditions [266], potentially contributing to the fertility disorders commonly associated with endometriosis [257]. The elevated cholesterol and cholesterol ester levels in the tissue samples of the DI are consistent with altered lipid profiles in the blood samples as reported in numerous studies [257, 259].

The KO samples show an increased occurrence of conjugated dienes [269]. This inflammation is an indication of oxidative stress. The reason for this could be the recruitment and activation of immune cells during the preparation of the endometrium for imminent ovulation.

4.6 Distinct Composition of Epithelial Cells in KO and DI Samples

ECs are built up of various components, including the cell membrane, Golgi apparatus, ribosomes, peroxisomes, cytoplasm, cytoskeleton, MIT, lysosomes, RNA, the ER and numerous small molecules [149, 150]. All these components work together to maintain the structural integrity of the cell and perform vital functions necessary for its survival and functioning. The cell nucleus is not included here, as it has been assigned to another separate component (blue). MIT play a pivotal role in the endometrium by providing the necessary energy for the various processes that take place during the menstrual cycle. In living cells, cytochrome c resides within the inner membrane of the MIT [179]. In PC-5, the loadings show peaks at 750 cm^{-1}, 1128 cm^{-1}, 1315 cm^{-1}, and 1583 cm^{-1}. All of these can be assigned to cytochrome c [179, 270] and are shifted toward the KO. Increased energy demand arises due to enhanced growth, tissue renewal, and preparation for a potential implantation of a fertilized egg. The endometrium examined was obtained in the proliferation phase, a phase characterized by an increased metabolism due to the reconstruction of the previously shed stratum

functionale [271]. This is consistent with the higher energy demand. Although some of these bands coincide with Raman signals from lipids and proteins (1128 cm^{-1} and 1315 cm^{-1}), the alterations in the intensity are most likely derived from the bands of cytochrome c [270].

The PC-5 loadings of ECs show elevated spectral bands shifting to the KO at 1022 cm^{-1}, and 1460 cm^{-1}. The peak at 1022 cm^{-1} can be assigned to ν(CC), ν(CO), β(COH) in D-(+)-glucose [180] and the spectral intensity at 1460 cm^{-1} can be assigned to $\delta(CH)_2$ in D-(+)-glucose and also in glycogen [180].

Although endometriosis is considered a benign disease, it shares several characteristics with cancer, such as uncontrolled cell proliferation, the ability to metastasize, and invasiveness [251, 272], leading to frequent associations between the two conditions. In light of the cancer-like features of endometriosis, the findings of Colagar et al. are relevant; they reported a decrease in carbohydrate concentration, including glycogen, in cancerous tissue compared to normal tissue [180]. Similarly, Stone et al. found that dysplastic and cancerous tissues have lower levels of glycogen, carbohydrates, protein disulfide bonds, and carotenoids compared to the healthy controls. These observations seem to confirm well-known biochemical changes associated with tumor progression, including increased metabolism for cell division, higher nuclear to cytoplasmic ratio, altered protein conformation, and tissue calcification [142].

The elevated glycogen levels observed in KO compared to DI may indicate that, unlike in cancer, endometrial cells retain higher carbohydrate reserves, possibly reflecting different metabolic demands or a less aggressive metabolic reprogramming compared to cancer and endometriotic cells. Chiriboga et al. highlighted that variations in glycogen intensity are important for interpreting glycogen-dependent effects such as cell maturation and hormone dependence [273]. In cancerous tissue, abnormal glycogen levels are often markers of metabolic reprogramming. Young et al. demonstrated that there is also metabolic reprogramming in endometriosis [274, 275] and the surrounding peritoneum. They demonstrated a shift to aerobic glycolysis (Warburg effect) similar to what can be observed in tumorigenesis [275]. In this environment, glycolysis is used

for energy production. The resulting increase in lactate concentration nourishes endometriotic cells, promoting lesion establishment and progression, as well as immune evasion, thereby facilitating the survival of ectopic endometrial cells, similar to cancer metastasis [275]. Chronic stress further alters the microenvironment, affecting multiple metabolic pathways and facilitating the implantation and invasion of endometriotic cells [274].

The metabolic reprogramming in endometriosis, which is similar to that observed in cancer cells, suggests that endometriotic lesions exhibit increased glycolysis, which supports the cells' proliferation and survival requirements under pathologic conditions.

The higher glycogen content in KO compared to DI may reflect the differing metabolic environments and inflammatory states of these tissues. Changes in the spectroscopic characteristics of glycogen might be due to variations in its concentration, the presence of different metabolites, or alterations in the cellular environment.

Bands exhibiting higher intensities in DI compared to the KO include 1235 cm^{-1}, attributed to the β-fold in the amide III band [181], and 1640 cm^{-1}, associated with ordered helical structures in the amide I region [182-186]. In contrast, the spectral intensity at 1674 cm^{-1}, which is higher in the KO, can be assigned to disordered structures in the amide I band [187, 188].

Our results suggest that the DI samples have a more ordered and stable protein structure, whereas the KO samples show greater structural disorder, which may have implications for their functional properties. DI-derived proinflammatory proteins trigger an enhanced inflammatory response that appears to promote the persistence of these lesions rather than their destruction [276]. The α-helix and the β-sheet provide information on how the polypeptide chains are folded. They are crucial for the stability of the proteins [159]. Both α-helix and β-sheets typically exhibit a remarkable stability [277]. The increased stability is consistent with the theory suggesting a fibrotic component in endometriosis [161]. Fibrotic tissue is known to be very stable and contains densely packed collagen fibers.

Additionally, the increased presence of glycogen in the KO samples may indicate alterations in cellular energy storage and metabolism, which may be linked to the heightened energy requirement during the proliferative phase of the menstrual cycle.

4.7 Nuclear Changes in Endometriotic Glands

In our study, RMS did not allow significant discrimination between KO and DI based on the nuclear component. We analyzed the trends using PC-1 ($p = 0.14$) and PC-3 ($p = 0.25$) to investigate the differences between KO and DI. In KO tissue, increased spectral signatures were detected in the phosphate scaffold of DNA [278], the DNA base guanine [279, 280] and the amide III region [281]. In endometriosis, the cytosine signals [282], the CH_3 content (methyl groups) [199, 283] and the amide II band dominated. The different spectral intensities of the amide II and amide III bands may provide evidence for alterations in the histone packing of the DNA. Beyer and Becker et al. were able to detect increased methylation and 5mC foci in DI, indicating altered chromatin organization that disrupts physiological cell function [221]. Subsequent Ki67 staining revealed lower proliferative activity in DI compared to KO, indicating the epigenetic methylation changes [221].

In a recent study, Letsiou et al. identified DNA methylation, histone modifications, and small RNA actions as the primary mechanisms altering chromatin structure. They can lead to either gene silencing or gene expression and create repressed or permissive chromatin states [284]. DNA methylation is considered one of the most important epigenetic mechanisms regulating development and response to environmental stressors [284]. Under stress, the DNA methylation profile may undergo substantial change [284].

4.8 Limitations of the Present Study

4.8.1 Number of Included Samples

A total of 40 tissue samples were collected from donors (13 KO and 21 DI), but only seven met the inclusion criteria of the study. The criteria included: no hormonal contraception, being premenopausal (KO: 39–48 y., DI LIS: 31–41 y.),

in the proliferation phase of the menstrual cycle, having DI in the lesser pelvis (LIG, SRV, DGS), and a histologically confirmed diagnosis (for DI). All other anamnestic circumstances such as smoking behavior, (number of) previous surgeries, duration of endometriosis, pregnancies and number of children were not included in the analysis. The study's small sample size limited the generalizability of the findings, and there was considerable variance among donors within each group.

For subsequent Raman measurements, three patients were included in the KO group and three in the DI group. From the latter, three samples were taken from the LIS. Additionally, two more samples were taken from two donors, one from the SRV and one from the DGS. All patients were in the same cycle phase, namely the proliferation phase. The proliferation phase follows immediately after menstruation and is therefore relatively easy to identify. In this phase, the stroma surrounding the glands is tightly bundled and exhibits some mitotic activity [128]. The spindle-shaped cells in the stroma have enlarged nuclei and little cytoplasm [128]. The ECs of the glands display microvilli and cilia [128]. The glands themselves are small, straight, narrow, and almost uniform in shape [128]. The proliferation phase was chosen due to its clear identifiability and the homogeneity of the glands, which should lead to better comparability of the samples.

We worked with cryopreserved samples, which is a great advantage for the RMS as it enables better comparability with in vivo conditions. The tissue can be analyzed more quickly on the measurement days as no deparaffinization is required. Raman spectroscopy often encounters difficulties with paraffin-embedded sections, as paraffin produces strong signals in both the fingerprint and higher wavelength regions of the spectrum, overlapping with biological signals [165, 285]. The paraffin components can be removed by (digital) deparaffinization, however this can significantly affect the lipid content of the samples and should be used with caution when analyzing lipid changes [248]. Digital dewaxing, on the other hand, prevents molecular changes in the sample due to paraffin removal, but at the same time limits the number of spectral regions available for analysis [285]. In contrast, cryosections are free of these paraffin peaks. Consequently, the signals of the tissue lipids are not distorted during

Raman measurements. Another factor contributing to altered lipid and protein content in samples is fixation with formalin [285]. Formalin causes tissue changes that can alter the Raman spectrum [163, 285]. It promotes the cross-linking of amine groups in the fingerprint region associated with proteins [163, 285]. Our cryopreserved samples were soaked in $DPBS^-$ rather than formalin, as is usually the case with paraffin samples.

However, the storage of cryopreserved tissue is more complex compared to paraffin samples. Cryoblocks must be stored at -80°C and then thawed to -20°C prior to cutting, with the temperature kept as stable as possible during the cutting process. Any thawing and refreezing stresses the tissue and should be avoided. Cryosections are fragile and tend to deteriorate noticeably over time, so they cannot be stored for extended periods. Cryopreserved tissue is less compact than paraffin-embedded tissue, making it more prone to tearing during cutting. The low tissue stability required a relatively large section width of 10 µm. The glands in the DI specimens showed a high degree of variability. Large glands occasionally exhibited tissue tears, and very small glands were often absent in contiguous sections due to the large section width. Careful handling of cryopreserved tissue is required to obtain high quality tissue sections for staining and subsequent analysis. Furthermore, histologic staining protocols often need to be adjusted for cryopreserved tissue as it behaves differently than paraffin-embedded samples.

4.8.2 Raman Artifacts

General problems associated with Raman spectroscopy, such as fluorescence and the inherent weakness of the Raman effect, limit its application in many areas [286]. Autofluorescence occurs when molecules absorb light at the excitation wavelength and subsequently emit light at longer wavelengths [287]. In Raman measurements, this contributes to background noise and can obscure the other Raman signals under investigation [286]. Choosing an appropriately long excitation wavelength can attenuate fluorescence, but exacerbates the problem of weak Raman signals, as the intensity of Raman scattering is inversely proportional to the fourth power of the excitation wavelength [286]. In many cases, it is not possible to increase the laser power to amplify the weak signal,

as biochemical cells are sensitive and susceptible to photodegradation and thermal damage.

Atkins et al. found that Raman spectroscopic analysis of red blood cells, whole blood, and purified plasma/serum also has specific limitations because certain components, such as hemoglobin, produce dominant signals that can mask other signals [287]. We used a laser source with a wavelength of 532 nm to analyze our samples. Due to insufficient processing, some samples still contained remnants of erythrocytes or siderophages, i.e. hemoglobin. We therefore also observed autofluorescence in our samples.

For highly absorbing Raman samples, the localized heat generation at the focal point of the incident laser can be so intense that the investigated molecules may be irreversibly damaged or thermally decomposed, leading to the destruction of the ROI for further analysis [288].

In our analysis of the lipid component (yellow dots) (Fig. 31 1), we observed that the laser beam sets small particles in motion. This phenomenon, known as “optical tweezing” [289], occurs when the intensity profile of the laser beam creates a force that pulls the particles towards the center of the beam [289]. When the laser beam is highly focused and directed downwards, it can create a three-dimensional trap that pulls the particles towards the focal point [289]. Ashkin et al. showed that a single, highly focused laser beam is sufficient to trap small dielectric particles in three dimensions [289]. In the resulting bitmaps, these particle movements appeared as visible yellow lines (Fig. 31 A and B), which are presumably due to loose particles from sample preparation or contaminated $DPBS^-$ that has been stored for too long and are therefore considered artifacts.

5 Conclusion and Outlook

This study utilized histologic and spectroscopic techniques to analyze differences between the glands and their surrounding stroma in endometrial tissue and endometriotic lesions. Standard pathologic staining methods proved to be effective in identifying glandular structures and differentiating between KO and DI. Movat Pentachrome staining provided insights into the extracellular matrix composition, revealing differences in the distribution of collagen fibers, elastic fibers, GAGs, and fibrin between KO and DI samples. Disparities in collagen fiber thickness/maturity between KO and DI were revealed by PSR staining and subsequent quantitative analysis. Endometriosis samples exhibited a higher prevalence of thick, mature collagen fibers, indicative of fibrotic remodeling associated with the benign disease. The distribution pattern of elastic fibers, identified through Resorcin Fuchsin staining, showed a more irregular and dense presence of elastic fibers around ectopic glands in DI samples compared to KO.

The RMS analysis provided a detailed molecular characterization of the tissue components. The TCA identified nuclei, ECs, lipids, collagen fibers, and elastic fibers within the samples. The consecutive PCA revealed significant biochemical differences in the composition of collagen fibers, tissue lipids, and epithelial cells between KO and DI.

Spectral differences between KO and DI tissues revealed shifts in the DI samples that can be attributed to COL I [161], the amide I region for ordered helical structures [182, 186], and the amide III region [164, 198, 200, 231]. In contrast, the KO samples showed increased spectral intensities for COL IV [94, 148, 161, 163, 197], disordered secondary structures in the amide I region [187] and the amide II band [198, 199, 201-203, 239]

The altered lipid profiles in the DI samples indicated a higher content of unsaturated FAs, potentially affecting membrane fluidity and cellular function.

The composition of KO ECs showed significant differences in spectral intensities, particularly in bands attributable to cytochrome c [179, 270]. This may reflect

increased energy requirements related to enhanced tissue growth, regeneration, and preparation for potential implantation of a fertilized egg. Additionally, the higher glycogen levels observed in KO samples may indicate increased energy storage to support these metabolic demands. In contrast, DI samples exhibited higher intensities in bands associated with β-sheet structures in the amide III region [181], and ordered helical structures in the amide I region [182-186]. Both α-helices and β-sheets typically exhibit a remarkable stability [277]. These increased spectral shifts in DI may be explained by chronic inflammation leading to fibrosis and scar tissue formation, altered protein synthesis favoring ordered α-helical and β-sheet structures, cellular stress responses causing protein misfolding, and increased protein degradation resulting in stable polypeptide aggregates [277].

In this study, RMS proved to be effective in differentiating between eutopic and ectopic endometrial glands and their surrounding stroma. By integrating RMS with imaging techniques (such as ultrasound, MRI), a more comprehensive diagnostic approach may be achieved.

Hollon et al. focused on Stimulated Raman Histology (SRH), an optical imaging method capable of providing fast, label-free images of biological tissue with submicrometer resolution [212]. Innovations in fiber laser technology have enabled the development of a Food and Drug Administration (FDA)-registered system able to generate SRH images in the operating room [212]. The integration of SRH images with Deep Convolutional Neural Networks (CNNs) enabled automatic image classification [212]. The diagnostic accuracy of SRH paired with CNNs equals or exceeds that of conventional HE histology [212]. Hollon et al. stated that the technology has the potential to be applied to other medical specialties such as dermatology, head and neck surgery, breast surgery, and gynecology [212]. Future developments may include the prediction of molecular changes and integration into modern molecular diagnostics [212].

Overall, RMS has proven to be a powerful tool with significant potential for advancements in various research and clinical diagnostics areas. Its integration into diverse scientific and medical fields promises to increase diagnostic

accuracy, advance research, and improve patient care through its detailed molecular analytical capabilities. By measuring significant biochemical changes in tissues, RMS enables the early detection of pathologic alterations before they become histopathologically visible. This early detection capability enables timely intervention, ultimately improving patient outcomes.

6 Supplementary

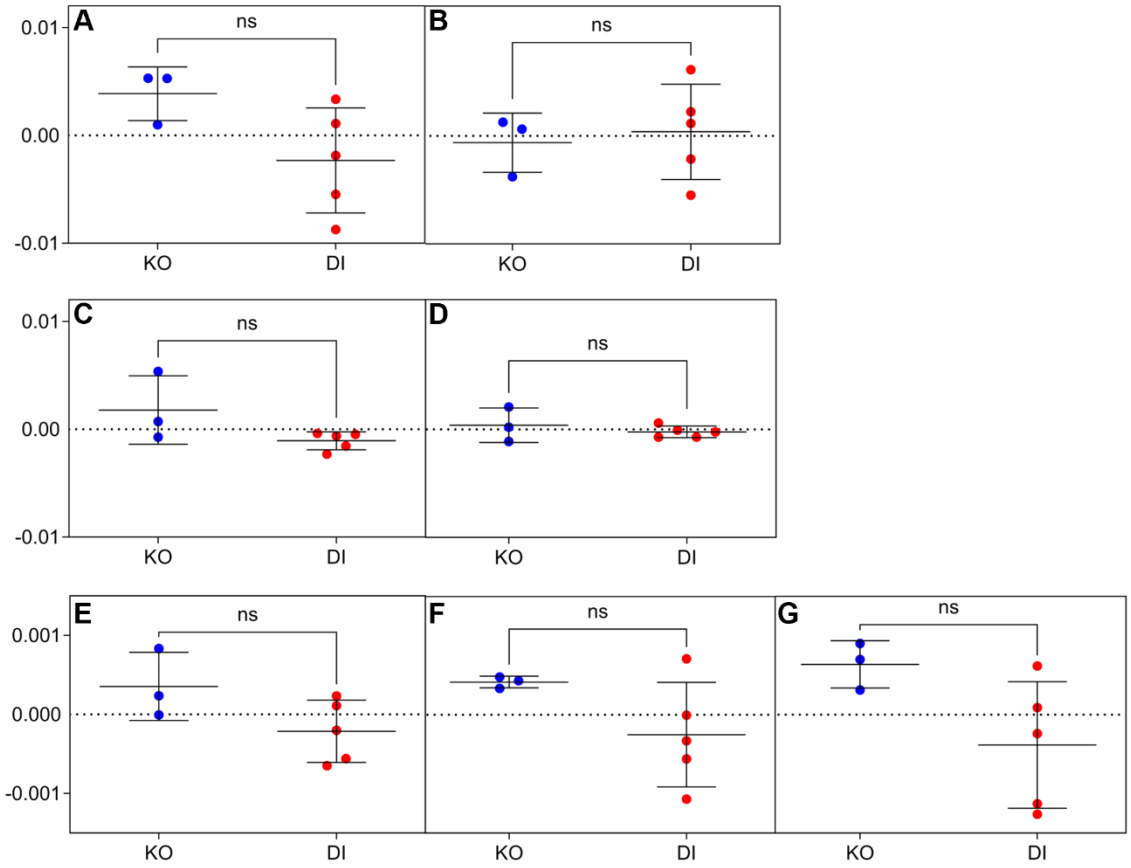

Figure 22 Score values of nuclei PC-1 – PC-7
The Mann-Whitney U test was conducted for PC-1 (A), PC-2 (B), PC-3 (C), PC-4 (D), PC-5 (E), PC-6 (F), and PC-7 (G) to compare the scores of KO (n=3) and DI (n=5). No significant differences in the scores between the groups were found. The blue points represent KO, and the red points represent DI.

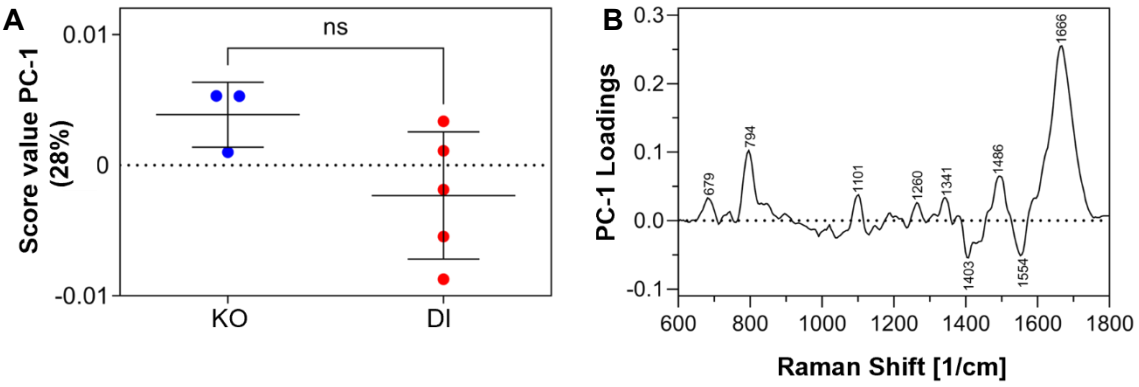

Figure 23 PCA of Nuclei PC-1
Score value of PC-1 for KO and DI (A). Loadings of PC-1 (B). The characteristic wavenumbers are labeled. The blue dots represent the KO, while the red dots represent DI.

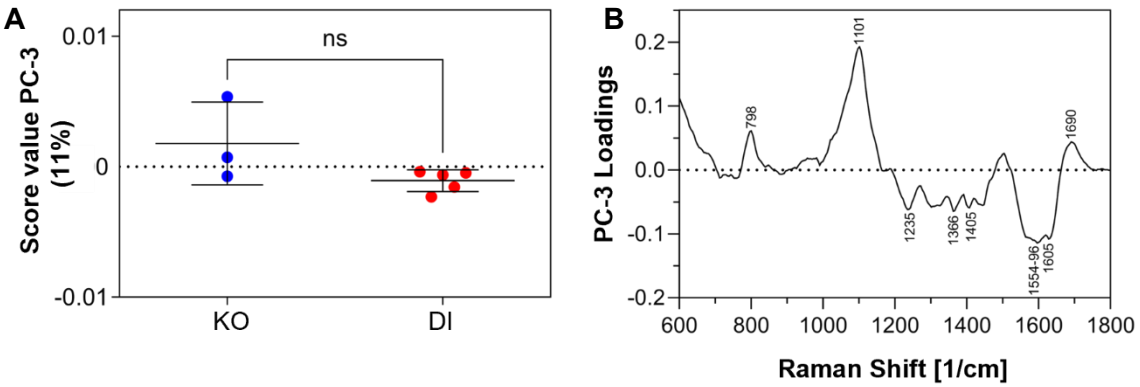

Figure 24 PCA of Nuclei PC-3
Score value of PC-3 for KO and DI (A). Loadings of PC-3 (B). The characteristic wavenumbers are labeled. The blue dots represent the KO, while the red dots represent DI.

Wavenumber (cm^{-1})	Assignment	References
676	Guanine	[279]
794	PO_2^-	[290]
798	PO_2^-	[290]
1096	PO_2^-	[290]
1256	Amide III	[281]
1341	Guanine	[290]
1366	CH_3	[283]
1401	bending modes of methyl groups	[199]
1484	Guanine	[290]
1554	Amide II	[291]
1592	Amide II	[291]
1605	Cytosine	[282]

Table 19 *Loadings of Nuclei PC1 and PC-3*

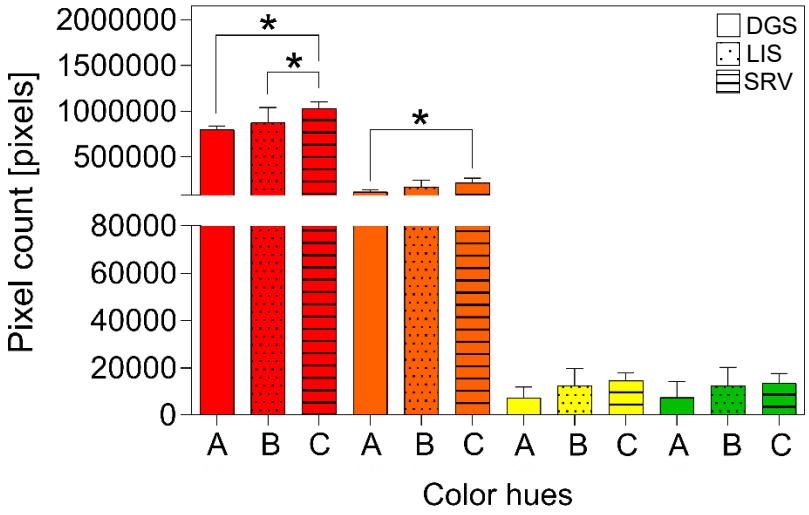

Figure 25 Quantification of collagen fibers according to assigned hues using PSR stain

*The bar graph compares the collagen fibers in the stroma of ectopic glands from different DI localizations: DGS (A), LIS (B), and SRV (C). The fractions of each color (red, orange, yellow, green) are defined according to Rich et al. [134]. A Kruskal-Wallis Test followed by Dunn's Test was performed to compare the individual color proportions for DGS (n=1), LIS (n=3), and SRV (n=1). Results are expressed as mean ± SD. *p<0.05.*

7 Deutsche Zusammenfassung

Endometriose ist eine weit verbreitete gynäkologische Erkrankung, die hauptsächlich Frauen im gebärfähigen Alter betrifft. Sie ist gekennzeichnet durch das Vorkommen von ektopem endometriumähnlichem Gewebe außerhalb des Uterus und geht häufig mit chronischen Schmerzen, Dysmenorrhoe, Dyspareunie, Dyschezie, Dysurie sowie Infertilität einher. Aufgrund ihrer heterogenen Symptomatik und fehlender spezifischer Biomarker gestaltet sich die Diagnosestellung oft schwierig. Der derzeitige Goldstandard ist die laparoskopische Operation mit anschließender histologischer Bestätigung. Trotz der geringen Komplikationsrate stellt dieses Verfahren einen invasiven Eingriff mit nicht zu vernachlässigenden Risiken dar. Zudem führt keine der aktuellen Behandlungsoptionen – weder chirurgisch noch medikamentös – zu einer endgültigen Heilung. Hormonelle Langzeittherapien sind in vielen Fällen symptomlindernd, jedoch insbesondere für junge Patientinnen mit Kinderwunsch keine zufriedenstellende Option.

Vor diesem Hintergrund war es Ziel dieser Studie, das diagnostische Potenzial der Raman-Mikrospektroskopie (RMS) zur Unterscheidung von eutopem und ektopem Endometriumgewebe zu untersuchen. Bei der RMS handelt es sich um eine nicht-invasive, markerunabhängige Technik, mit der auf Basis von Photon-Molekül-Wechselwirkungen organische und anorganische Materialen analysiert und Gewebe anhand ihrer chemischen Zusammensetzung charakterisiert werden können.

Zur Beantwortung der Fragestellung wurden histologisch bestätigte Gewebeproben von eutopem Endometrium (KO) und endometriotischen Herden (DI) mit der RMS untersucht. Dabei wurden kryokonservierte Gewebeschnitte verwendet, um den nativen Gewebeverhältnissen möglichst nahe zu kommen. Insgesamt wurden Proben von sechs Patientinnen eingeschlossen (n=3 KO; Alter 39–48 Jahre, Mittelwert: 44 Jahre; n=3 DI; Alter 31–41 Jahre, Mittelwert: 36,75 Jahre). Bei zwei DI-Patientinnen konnten zusätzliche Herde aus verschiedenen Lokalisationen (*Ligamentum sacrouterinum* (LIS), *Douglas-Raum*

(DGS) und *Septum rectovaginale* (SRV)) gewonnen werden. Alle Proben wurden in der proliferativen Phase entnommen.

Nach histologischer Färbung zur Lokalisation der Drüsenregionen und des umgebenden Stromas erfolgte die Raman-spektroskopische Messung des konsekutiven, nativen Gewebeschnitts. Die resultierenden Spektren wurden mittels PCA- und TCA-Analyse ausgewertet, um Unterschiede in der molekularen Zusammensetzung der Gewebe zu identifizieren. Dies ermöglichte eine detaillierte molekulare Charakterisierung der Kollagenmerkmale, der Lipidprofile und der Zusammensetzung der Epithelzellen. In den Spektren der Zellkerne konnten keine signifikanten Unterschiede gefunden wurden.

Die Ergebnisse dieser Studie zeigen das Potential der RMS auf zur Differenzierung zwischen KO und DI. Langfristig könnte die Methode als ergänzendes Diagnoseinstrument weiterentwickelt werden, um endometriotische Läsionen z.B. während minimal-invasiver Operationen in Echtzeit sicher zu identifizieren und von gesundem Gewebe zu unterscheiden. Aufgrund der begrenzten Fallzahl sind jedoch weiterführende Studien mit größeren Patientenkollektiven und zusätzlichen Läsionslokalisationen erforderlich, um die diagnostische Genauigkeit und klinische Relevanz zu validieren. Die identifizierten molekularen und strukturellen Unterschiede zwischen KO und DI könnten darüber hinaus neue Ansatzpunkte für zukünftige therapeutische Ansätze bieten.

1. Gerhard Aumüller, J.E., Joachim Kirsch, Siegfried Mense, *Anatomie*. 3., kompl. überarb. u. akt. Auflage ed. 2014: Thieme (Verlag).
2. Reed, B.G. and B.R. Carr, *The Normal Menstrual Cycle and the Control of Ovulation*, in *Endotext*, K.R. Feingold, et al., Editors. 2000, Inc. Copyright © 2000-2021, MDText.com.: South Dartmouth (MA).
3. Baumann, R., *Physiologie*. 2010: Georg Thieme Verlag.
4. Arruda, M.S., et al., *Time elapsed from onset of symptoms to diagnosis of endometriosis in a cohort study of Brazilian women.* Hum Reprod, 2003. **18**(4): p. 756-9.
5. Burney, R.O. and L.C. Giudice, *Pathogenesis and pathophysiology of endometriosis.* Fertil Steril, 2012. **98**(3): p. 511-9.
6. Streuli, I., et al., *Endometriosis after menopause: physiopathology and management of an uncommon condition.* Climacteric, 2017. **20**(2): p. 138-143.
7. Oehmke, F., et al., *State of the data on endometriosis.* Der Gynäkologe, 2007. **40**: p. 521-526.
8. Mounsey, A.L., A. Wilgus, and D.C. Slawson, *Diagnosis and management of endometriosis.* Am Fam Physician, 2006. **74**(4): p. 594-600.
9. Falcone, T. and R. Flyckt, *Clinical management of endometriosis.* Obstetrics & Gynecology, 2018. **131**(3): p. 557-571.
10. Tulandi, T. and D. Redwine, *Endometriosis: advances and controversies.* 2003.
11. Nagele, F., *Endometriose–Ein unterschätztes Leid.* J Gynäkol Endokrinol, 2009. **3**: p. 45-46.
12. Samani, E.N., et al., *Micrometastasis of endometriosis to distant organs in a murine model.* Oncotarget, 2019. **10**(23): p. 2282-2291.
13. Mechsner, S., *Endometriose.* Der Schmerz, 2016. **30**(5): p. 477-490.
14. Schindler, A.E., *Epidemiologie, pathogenese und diagnostik der endometriose.* Journal für Fertilität und Reproduktion, 2007. **17**(4): p. 22-27.
15. Adams, P.S., *Endometriosis of the Bladder: Report of a Case.* The Journal of Urology, 1938. **40**(3): p. 390-396.
16. Kiesel, L. and M. Sourouni, *Diagnosis of endometriosis in the 21st century.* Climacteric, 2019. **22**(3): p. 296-302.
17. Agarwal, N. and A. Subramanian, *Endometriosis - Morphology, clinical presentations and molecular pathology.* J Lab Physicians, 2010. **2**(01): p. 001-009.
18. Galle, P.C., *Clinical Presentation and Diagnosis of Endometriosis.* Obstetrics and Gynecology Clinics of North America, 1989. **16**(1): p. 29-42.
19. Oehmke, F., et al., *Datenlage zur Endometriose.* Der Gynäkologe, 2007. **40**(7): p. 521-526.
20. Ulrich, U., et al., *National German Guideline (S2k): Guideline for the Diagnosis and Treatment of Endometriosis.* Long Version – AWMF Registry No. 015-045, 2014. **74**(12): p. 1104-1118.
21. Horn, L.-C., et al., *S2k-Leitlinie Diagnostik und Therapie der Endometriose – Anforderungen an die PathologieS2k guidelines for the*

diagnosis and treatment of endometriosis—Recommendations for pathology. Der Pathologe, 2021. **43**.
22. Donnez, J., C.A. Stratopoulou, and M.-M. Dolmans, *Endometriosis and adenomyosis: Similarities and differences.* Best Practice & Research Clinical Obstetrics & Gynaecology, 2024. **92**: p. 102432.
23. Bergqvist, A., *Different types of extragenital endometriosis: A review.* Gynecological Endocrinology, 1993. **7**(3): p. 207-221.
24. Veeraswamy, A., et al., *Extragenital Endometriosis.* Clinical Obstetrics and Gynecology, 2010. **53**(2).
25. Redwine, D.B., *Diaphragmatic endometriosis: diagnosis, surgical management, and long-term results of treatment.* Fertility and Sterility, 2002. **77**(2): p. 288-296.
26. Keckstein, J., et al., *The #Enzian classification: A comprehensive non-invasive and surgical description system for endometriosis.* Acta Obstet Gynecol Scand, 2021. **100**(7): p. 1165-1175.
27. *Revised American Society for Reproductive Medicine classification of endometriosis: 1996.* Fertil Steril, 1997. **67**(5): p. 817-21.
28. HAAS, D., et al., *The rASRM score and the Enzian classification for endometriosis: their strengths and weaknesses.* Acta Obstetricia et Gynecologica Scandinavica, 2013. **92**(1): p. 3-7.
29. Hornstein, M.D., et al., *The reproducibility of the revised American Fertility Society classification of endometriosis**Supported in part by grant MO1 RR02635 from the National Institutes of Health, Bethesda, Maryland, to the Brigham and Women's Hospital General Clinical Research Center, Boston, Massachusetts, and by a grant from Hoechst-Roussel Pharmaceuticals Inc, Somerville, New Jersey.* Fertility and Sterility, 1993. **59**(5): p. 1015-1021.
30. Vercellini, P., et al., *Endometriosis and pelvic pain: relation to disease stage and localization.* Fertil Steril, 1996. **65**(2): p. 299-304.
31. Guzick, D.S., et al., *Prediction of pregnancy in infertile women based on the American Society for Reproductive Medicine's revised classification of endometriosis.* Fertil Steril, 1997. **67**(5): p. 822-9.
32. Adamson, G.D. and D.J. Pasta, *Endometriosis fertility index: the new, validated endometriosis staging system.* Fertil Steril, 2010. **94**(5): p. 1609-15.
33. Lee, S.-Y., Y.-J. Koo, and D.-H. Lee, *Classification of endometriosis.* Yeungnam University Journal of Medicine, 2020. **38**.
34. Tuttlies, F., et al., *[ENZIAN-score, a classification of deep infiltrating endometriosis].* Zentralbl Gynakol, 2005. **127**(5): p. 275-81.
35. Haas, D., et al., *Efficacy of the revised Enzian classification: a retrospective analysis. Does the revised Enzian classification solve the problem of duplicate classification in rASRM and Enzian?* Arch Gynecol Obstet, 2013. **287**(5): p. 941-5.
36. Keckstein, J., et al., *The #Enzian classification: A comprehensive non-invasive and surgical description system for endometriosis.* Acta Obstetricia et Gynecologica Scandinavica, 2021. **100**(7): p. 1165-1175.
37. Haas, D., et al., *Preoperative planning of surgery for deeply infiltrating endometriosis using the ENZIAN classification.* European Journal of

Obstetrics & Gynecology and Reproductive Biology, 2013. **166**(1): p. 99-103.
38. Sarkisova Viktoriya, V., *Epidemiology, Theories Of The Development, Conservative And Operative Treatment Of The Endometriosis.* The Peerian Journal, 2023. **15**: p. 84-93.
39. Bohn, J.A., et al., *Stepwise Approach to the Management of Endometriosis-Related Dysmenorrhea: A Cost-Effectiveness Analysis.* Obstetrics & Gynecology, 2021. **138**(4).
40. Nezhat, C., et al., *Optimal Management of Endometriosis and Pain.* Obstetrics & Gynecology, 2019. **134**(4).
41. Rafique, S. and A.H. Decherney, *Medical management of endometriosis.* Clinical obstetrics and gynecology, 2017. **60**(3): p. 485.
42. Meuleman, C., et al., *Surgical treatment of deeply infiltrating endometriosis with colorectal involvement.* Human Reproduction Update, 2011. **17**(3): p. 311-326.
43. Kim, S.J., et al., *Cumulative Recurrence Rate and Risk Factors for Recurrent Abdominal Wall Endometriosis after Surgical Treatment in a Single Institution.* Yonsei Medical Journal, 2022. **63**(5): p. 446.
44. Navarro, R., et al., *Endometriosis in pregnancy.* Abdominal Radiology, 2020. **45**: p. 1741-1753.
45. Imboden, S. and M.D. Mueller, *Lebensqualität bei Patientinnen mit Endometriose.* Gynäkologische Endokrinologie, 2018. **16**(2): p. 76-79.
46. Secosan, C., et al., *Endometriosis in Menopause-Renewed Attention on a Controversial Disease.* Diagnostics (Basel), 2020. **10**(3).
47. Ladanyi, C., et al., *Postmenopausal endometriosis, where are we now?* Curr Opin Obstet Gynecol, 2019. **31**(4): p. 267-278.
48. Greene, R., et al., *Diagnostic experience among 4,334 women reporting surgically diagnosed endometriosis.* Fertility and sterility, 2009. **91**(1): p. 32-39.
49. Hadfield, R., et al., *Delay in the diagnosis of endometriosis: a survey of women from the USA and the UK.* Human Reproduction, 1996. **11**(4): p. 878-880.
50. Hudelist, G., et al., *Diagnostic delay for endometriosis in Austria and Germany: causes and possible consequences.* Human reproduction, 2012. **27**(12): p. 3412-3416.
51. Dmowski, W.P., et al., *Changing trends in the diagnosis of endometriosis: a comparative study of women with pelvic endometriosis presenting with chronic pelvic pain or infertility.* Fertility and sterility, 1997. **67**(2): p. 238-243.
52. Vercellini, P., et al., *Chronic pelvic pain in women: etiology, pathogenesis and diagnostic approach.* Gynecological Endocrinology, 2009. **25**(3): p. 149-158.
53. Pascoal, E., et al., *Strengths and limitations of diagnostic tools for endometriosis and relevance in diagnostic test accuracy research.* Ultrasound in Obstetrics & Gynecology, 2022. **60**(3): p. 309-327.
54. Halis, G., S. Mechsner, and A.D. Ebert, *The diagnosis and treatment of deep infiltrating endometriosis.* Dtsch Arztebl Int, 2010. **107**(25): p. 446-55; quiz 456.

55. Nezhat, C., et al., *Multidisciplinary treatment for thoracic and abdominopelvic endometriosis.* Jsls, 2014. **18**(3).
56. Steck, T., et al., *Endometriose: Entstehung, Diagnose, Verlauf und Therapie*. 2011: Springer-Verlag.
57. Tietjen, G.E., et al., *Migraine Is Associated With Menorrhagia and Endometriosis.* Headache: The Journal of Head and Face Pain, 2006. **46**(3): p. 422-428.
58. Bazot, M. and E. Daraï, *Diagnosis of deep endometriosis: clinical examination, ultrasonography, magnetic resonance imaging, and other techniques.* Fertility and sterility, 2017. **108**(6): p. 886-894.
59. Bazot, M., et al., *Diagnostic accuracy of physical examination, transvaginal sonography, rectal endoscopic sonography, and magnetic resonance imaging to diagnose deep infiltrating endometriosis.* Fertility and Sterility, 2009. **92**(6): p. 1825-1833.
60. Habiba, M., I. Brosens, and G. Benagiano, *Müllerianosis, endocervicosis, and endosalpingiosis of the urinary tract: a literature review.* Reproductive Sciences, 2018. **25**: p. 1607-1618.
61. Horn, L.-C., et al., *S2k-Leitlinie Diagnostik und Therapie der Endometriose – Anforderungen an die Pathologie.* Der Pathologe, 2022. **43**(2): p. 117-125.
62. Aznaurova, Y.B., et al., *Molecular aspects of development and regulation of endometriosis.* Reproductive Biology and Endocrinology, 2014. **12**(1): p. 50.
63. Bazot, M. and E. Daraï, *Role of transvaginal sonography and magnetic resonance imaging in the diagnosis of uterine adenomyosis.* Fertility and Sterility, 2018. **109**(3): p. 389-397.
64. Bazot, M., et al., *Ultrasonography compared with magnetic resonance imaging for the diagnosis of adenomyosis: correlation with histopathology.* Human Reproduction, 2001. **16**(11): p. 2427-2433.
65. Dueholm, M. and E. Lundorf, *Transvaginal ultrasound or MRI for diagnosis of adenomyosis.* Current Opinion in Obstetrics and Gynecology, 2007. **19**(6): p. 505-512.
66. Zhang, M., et al., *MRI of Adenomyosis: Where Are We Today?* Canadian Association of Radiologists Journal, 2022. **74**(1): p. 58-68.
67. Brosens, I., et al., *Diagnosis of endometriosis: pelvic endoscopy and imaging techniques.* Best practice & research Clinical obstetrics & gynaecology, 2004. **18**(2): p. 285-303.
68. Vercellini, P., et al., *The pathogenesis of bladder detrusor endometriosis.* American Journal of Obstetrics and Gynecology, 2002. **187**(3): p. 538-542.
69. Dmowski, W.P., *Pitfalls in clinical, laparoscopic and histologic diagnosis of endometriosis.* Acta Obstetricia et Gynecologica Scandinavica, 1984. **63**(sup123): p. 61-66.
70. Strehl, J.D., et al., *Correlation of histological and macroscopic findings in peritoneal endometriosis.* Int J Clin Exp Pathol, 2014. **7**(1): p. 152-62.
71. Brosens, I.A., *Is mild endometriosis a progressive disease?* Human Reproduction, 1994. **9**(12): p. 2209-2211.

72. Sasamoto, N., et al., *Circulating proteomic profiles associated with endometriosis in adolescents and young adults.* Human Reproduction, 2022. **37**(9): p. 2042-2053.
73. Donnez, J. and A. Van Langendonckt, *Typical and subtle atypical presentations of endometriosis.* Current Opinion in Obstetrics and Gynecology, 2004. **16**(5): p. 431-437.
74. Nisolle, M. and J. Donnez, *Peritoneal endometriosis, ovarian endometriosis, and adenomyotic nodules of the rectovaginal septum are three different entities.* Fertility and Sterility, 1997. **68**(4): p. 585-596.
75. Nisolle, M., F. Casanas-Roux, and J. Donnez, *Immunohistochemical analysis of proliferative activity and steroid receptor expression in peritoneal and ovarian endometriosis.* Fertility and Sterility, 1997. **68**(5): p. 912-919.
76. Schweppe, K.W., *[Not Available].* Zentralbl Gynakol, 1999. **121**(7): p. 330-5.
77. Brosens, J., et al., *Noninvasive diagnosis of endometriosis: the role of imaging and markers.* Obstet Gynecol Clin North Am, 2003. **30**(1): p. 95-114, viii-ix.
78. Moisoiu, V., et al., *SERS liquid biopsy: An emerging tool for medical diagnosis.* Colloids Surf B Biointerfaces, 2021. **208**: p. 112064.
79. May, K.E., et al., *Peripheral biomarkers of endometriosis: a systematic review.* Human Reproduction Update, 2010. **16**(6): p. 651-674.
80. May, K.E., et al., *Endometrial alterations in endometriosis: a systematic review of putative biomarkers.* Human Reproduction Update, 2011. **17**(5): p. 637-653.
81. Notarstefano, V., et al., *Vibrational characterization of granulosa cells from patients affected by unilateral ovarian endometriosis: New insights from infrared and Raman microspectroscopy.* Spectrochimica Acta Part A: Molecular and Biomolecular Spectroscopy, 2019. **212**: p. 206-214.
82. Anastasiu, C.V., et al., *Biomarkers for the Noninvasive Diagnosis of Endometriosis: State of the Art and Future Perspectives.* Int J Mol Sci, 2020. **21**(5).
83. Prats-Mateu, B. and N. Gierlinger, *Tip in-light on: Advantages, challenges, and applications of combining AFM and Raman microscopy on biological samples.* Microsc Res Tech, 2017. **80**(1): p. 30-40.
84. Potlog-Nahari, C., et al., *CD10 immunohistochemical staining enhances the histological detection of endometriosis.* Fertil Steril, 2004. **82**(1): p. 86-92.
85. Mariani, M.M. and V. Deckert, *Raman Spectroscopy: Principles, Bene.ts, and Applications*, in *Methods in Physical Chemistry*. 2012. p. 419-444.
86. Esmonde-White, F. and M. Morris, *Emerging Raman Applications and Techniques in Biomedical and Pharmaceutical Fields; Raman Imaging and Raman Mapping*. 2010, Springer, Berlin, Heidelberg.
87. Brauchle, E. and K. Schenke-Layland, *Raman spectroscopy in biomedicine - non-invasive in vitro analysis of cells and extracellular matrix components in tissues.* Biotechnol J, 2013. **8**(3): p. 288-97.
88. Brauchle, E. and K. Schenke-Layland, *Raman spectroscopy in biomedicine – non-invasive in vitro analysis of cells and extracellular*

matrix components in tissues. Biotechnology Journal, 2013. **8**(3): p. 288-297.
89. Devitt, G., et al., *Raman Spectroscopy: An Emerging Tool in Neurodegenerative Disease Research and Diagnosis.* ACS Chem Neurosci, 2018. **9**(3): p. 404-420.
90. John, N. and S. George, *Chapter 5 - Raman Spectroscopy*, in *Spectroscopic Methods for Nanomaterials Characterization*, S. Thomas, et al., Editors. 2017, Elsevier. p. 95-127.
91. Devitt, G., et al., *Raman Spectroscopy: An Emerging Tool in Neurodegenerative Disease Research and Diagnosis.* ACS Chemical Neuroscience, 2018. **9**(3): p. 404-420.
92. Renata, J., *Micro and nanocapsules as supports for Surface-Enhanced Raman Spectroscopy (SERS).* Physical Sciences Reviews, 2016. **1**(1).
93. Sitarski, A., *Development of Spectroscopic Methods for Dynamic Cellular Level Study of Biochemical Kinetics and Disease Progression.* 2017.
94. Stone, N., et al., *Raman spectroscopy for identification of epithelial cancers.* Faraday Discuss, 2004. **126**: p. 141-57; discussion 169-83.
95. Kendall, C., et al., *Raman spectroscopy, a potential tool for the objective identification and classification of neoplasia in Barrett's oesophagus.* The Journal of Pathology, 2003. **200**(5): p. 602-609.
96. Raja, P., et al., *Characterization of blood plasma of normal and cervical cancer patients using NIR raman spectroscopy.* Vibrational Spectroscopy, 2019. **102**: p. 1-7.
97. Farooq, A., et al., *On-chip Raman spectroscopy of live single cells for the staging of oesophageal adenocarcinoma progression.* Scientific Reports, 2024. **14**(1): p. 1761.
98. Hubbard, T.J.E., A. Shore, and N. Stone, *Raman spectroscopy for rapid intra-operative margin analysis of surgically excised tumour specimens.* Analyst, 2019. **144**(22): p. 6479-6496.
99. Chen, T., A. Yavuz, and M.C. Wang, *Dissecting lipid droplet biology with coherent Raman scattering microscopy.* Journal of Cell Science, 2021. **135**(5).
100. Canetta, E., *Current and Future Advancements of Raman Spectroscopy Techniques in Cancer Nanomedicine.* Int J Mol Sci, 2021. **22**(23).
101. Hobro, A.J., et al., *Raman spectroscopic analysis of malaria disease progression via blood and plasma samples.* Analyst, 2013. **138**(14): p. 3927-3933.
102. Ryzhikova, E., et al., *Raman spectroscopy and machine learning for biomedical applications: Alzheimer's disease diagnosis based on the analysis of cerebrospinal fluid.* Spectrochim Acta A Mol Biomol Spectrosc, 2021. **248**: p. 119188.
103. Gala, U. and H. Chauhan, *Principles and applications of Raman spectroscopy in pharmaceutical drug discovery and development.* Expert Opin Drug Discov, 2015. **10**(2): p. 187-206.
104. Zhang, S., et al., *Molecular Fingerprint Detection Using Raman and Infrared Spectroscopy Technologies for Cancer Detection: A Progress Review.* Biosensors (Basel), 2023. **13**(5).

105. Lin, X.M. and J.F. Li, *Applications of In Situ Raman Spectroscopy on Rechargeable Batteries and Hydrogen Energy Systems.* ChemElectroChem, 2023. **10**.
106. Schulz, H. and M. Baranska, *Identification and quantification of valuable plant substances by IR and Raman spectroscopy.* Vibrational Spectroscopy, 2007. **43**(1): p. 13-25.
107. Parlatan, U., et al., *Raman spectroscopy as a non-invasive diagnostic technique for endometriosis.* Sci Rep, 2019. **9**(1): p. 19795.
108. Lieber, C., et al., *Diagnostic tool for early detection of ovarian cancers using Ramanspectroscopy*. BiOS 2000 The International Symposium on Biomedical Optics. Vol. 3918. 2000: SPIE.
109. Patel, I.I., et al., *High contrast images of uterine tissue derived using Raman microspectroscopy with the empty modelling approach of multivariate curve resolution-alternating least squares.* Analyst, 2011. **136**(23): p. 4950-4959.
110. Movat, H.Z., *Demonstration of all connective tissue elements in a single section; pentachrome stains.* AMA archives of pathology, 1955. **60**(3): p. 289-295.
111. Russell Jr, H., *A modification of Movat's pentachrome stain.* Archives of pathology, 1972. **94**(2): p. 187-191.
112. *Commercial Resorcin-Fuchsin as a Stain for Elastic Fibers.* Stain Technology, 1960. **35**(6): p. 347-357.
113. Bancroft, J.D. and C. Layton, *12 - Connective and other mesenchymal tissues with their stains*, in *Bancroft's Theory and Practice of Histological Techniques (Eighth Edition)*, S.K. Suvarna, C. Layton, and J.D. Bancroft, Editors. 2019, Elsevier. p. 153-175.
114. Zbinden, A., et al., *Non-invasive marker-independent high content analysis of a microphysiological human pancreas-on-a-chip model.* Matrix Biology, 2020. **85-86**: p. 205-220.
115. Daum, R., et al., *Non-invasive detection of DNA methylation states in carcinoma and pluripotent stem cells using Raman microspectroscopy and imaging.* Scientific Reports, 2019. **9**(1): p. 7014.
116. Kast, R.E., et al., *Emerging technology: applications of Raman spectroscopy for prostate cancer.* Cancer and Metastasis Reviews, 2014. **33**(2): p. 673-693.
117. Pudlas, M., et al., *Non-contact discrimination of human bone marrow-derived mesenchymal stem cells and fibroblasts using Raman spectroscopy.* Medical Laser Application, 2011. **26**(3): p. 119-125.
118. He, X., et al., *Raman spectroscopy coupled with principal component analysis to quantitatively analyze four crystallographic phases of explosive CL-20.* RSC Advances, 2018. **8**(41): p. 23348-23352.
119. Holzweber, M., et al., *Principal component analysis (PCA)-assisted time-of-flight secondary-ion mass spectrometry (ToF-SIMS): a versatile method for the investigation of self-assembled monolayers and multilayers as precursors for the bottom-up approach of nanoscaled devices.* Anal Chem, 2014. **86**(12): p. 5740-8.
120. Muramoto, S., et al., *ToF-SIMS Analysis of Adsorbed Proteins: Principal Component Analysis of the Primary Ion Species Effect on the Protein*

Fragmentation Patterns. J Phys Chem C Nanomater Interfaces, 2011. **115**(49): p. 24247-24255.
121. Pichardo-Molina, J.L., et al., *Raman spectroscopy and multivariate analysis of serum samples from breast cancer patients.* Lasers Med Sci, 2007. **22**(4): p. 229-36.
122. Biesinger, M.C., et al., *Principal component analysis of TOF-SIMS images of organic monolayers.* Anal Chem, 2002. **74**(22): p. 5711-6.
123. Wagner, M.S. and D.G. Castner, *Characterization of Adsorbed Protein Films by Time-of-Flight Secondary Ion Mass Spectrometry with Principal Component Analysis.* Langmuir, 2001. **17**(15): p. 4649-4660.
124. Wagner, M.S., et al., *Maximizing information obtained from secondary ion mass spectra of organic thin films using multivariate analysis.* Surface Science, 2004. **570**(1): p. 78-97.
125. Graham, D.J. and D.G. Castner, *Multivariate analysis of ToF-SIMS data from multicomponent systems: the why, when, and how.* Biointerphases, 2012. **7**(1-4): p. 49.
126. Levander, G. and P. Normann, *The Pathogenesis of Endometriosis an Experimental Study.* Acta obstetricia et gynecologica Scandinavica, 1955. **34**(4): p. 366-398.
127. Tempest, N., et al., *Novel microarchitecture of human endometrial glands: implications in endometrial regeneration and pathologies.* Human Reproduction Update, 2022. **28**(2): p. 153-171.
128. Monis, C.N. and M. Tetrokalashvili, *Menstrual Cycle Proliferative And Follicular Phase*. 2023: StatPearls Publishing, Treasure Island (FL).
129. Maxey, A.P. and M.L. McCain, *Tools, techniques, and future opportunities for characterizing the mechanobiology of uterine myometrium.* Exp Biol Med (Maywood), 2021. **246**(9): p. 1025-1035.
130. Kazlouskaya, V., et al., *The utility of elastic Verhoeff-Van Gieson staining in dermatopathology.* Journal of Cutaneous Pathology, 2013. **40**(2): p. 211-225.
131. Egging, D., et al., *Analysis of obstetric complications and uterine connective tissue in tenascin-X-deficient humans and mice.* Cell and tissue research, 2008. **332**: p. 523-32.
132. Vigano, P., et al., *Time to redefine endometriosis including its pro-fibrotic nature.* Hum Reprod, 2018. **33**(3): p. 347-352.
133. Strehl, J., et al., *Correlation of histological and macroscopic findings in peritoneal endometriosis.* International journal of clinical and experimental pathology, 2014. **7**: p. 152-62.
134. Rich, L. and P. Whittaker. *Collagen and picrosirius red staining: a polarized light assessment of fibrillar hue and spatial distribution*. 2005.
135. Junqueira, L.C.U., G. Bignolas, and R.R. Brentani, *Picrosirius staining plus polarization microscopy, a specific method for collagen detection in tissue sections.* The Histochemical Journal, 1979. **11**(4): p. 447-455.
136. Dayan, D., et al., *Are the polarization colors of Picrosirius red-stained collagen determined only by the diameter of the fibers?* Histochemistry, 1989. **93**(1): p. 27-29.
137. Rittié, L., *Method for Picrosirius Red-Polarization Detection of Collagen Fibers in Tissue Sections.* Methods Mol Biol, 2017. **1627**: p. 395-407.

138. Notingher, I., et al., *Spectroscopic study of human lung epithelial cells (A549) in culture: Living cells versus dead cells.* Biopolymers, 2003. **72**(4): p. 230-240.
139. De Gelder, J., et al., *Reference database of Raman spectra of biological molecules.* Journal of Raman Spectroscopy, 2007. **38**(9): p. 1133-1147.
140. Uzunbajakava, N., et al., *Nonresonant confocal Raman imaging of DNA and protein distribution in apoptotic cells.* Biophys J, 2003. **84**(6): p. 3968-81.
141. Nijssen, A., et al., *Discriminating basal cell carcinoma from its surrounding tissue by Raman spectroscopy.* The Journal of investigative dermatology, 2002. **119**(1): p. 64-69.
142. Stone, N., et al., *Near-infrared Raman spectroscopy for the classification of epithelial pre-cancers and cancers.* Journal of Raman Spectroscopy, 2002. **33**(7): p. 564-573.
143. Patil, C.A., et al., *Integrated system for combined Raman spectroscopy-spectral domain optical coherence tomography.* Journal of biomedical optics, 2011. **16 1**: p. 011007.
144. Ruiz-Chica, A.J., et al., *Characterization by Raman spectroscopy of conformational changes on guanine–cytosine and adenine–thymine oligonucleotides induced by aminooxy analogues of spermidine.* Journal of Raman Spectroscopy, 2004. **35**: p. 93-100.
145. Lin, H.-H., et al., *Single Nuclei Raman Spectroscopy for Drug Evaluation.* Analytical Chemistry, 2012. **84**(1): p. 113-120.
146. Chan, J.W., et al., *Micro-Raman spectroscopy detects individual neoplastic and normal hematopoietic cells.* Biophys J, 2006. **90**(2): p. 648-56.
147. Talari, A.C.S., et al., *Raman Spectroscopy of Biological Tissues.* Applied Spectroscopy Reviews, 2015. **50**(1): p. 46-111.
148. Notingher, I., et al., *Discrimination between ricin and sulphur mustard toxicity in vitro using Raman spectroscopy.* J R Soc Interface, 2004. **1**(1): p. 79-90.
149. Chaffey, N., *Alberts, B., Johnson, A., Lewis, J., Raff, M., Roberts, K. and Walter, P. Molecular biology of the cell. 4th edn*. 2003, Oxford University Press.
150. Shen, Y., et al., *Recent progress of surface-enhanced Raman spectroscopy for subcellular compartment analysis.* Theranostics, 2021. **11**(10): p. 4872-4893.
151. Kurn, H. and D.T. Daly, *Histology, Epithelial Cell*, in *StatPearls*. 2023, StatPearls Publishing

152. Wattanavichean, N., et al., *Organelle specific simultaneous Raman/green fluorescence protein microspectroscopy for living cell physicochemical studies.* Journal of Biophotonics, 2020. **13**(4): p. e201960163.
153. Adamczyk, A., et al., *Toward Raman Subcellular Imaging of Endothelial Dysfunction.* J Med Chem, 2021. **64**(8): p. 4396-4409.

154. Krafft, C., et al., *Label-Free Molecular Imaging of Biological Cells and Tissues by Linear and Nonlinear Raman Spectroscopic Approaches.* Angewandte Chemie International Edition, 2017. **56**(16): p. 4392-4430.
155. Krafft, C., et al., *Near infrared Raman spectra of human brain lipids.* Spectrochimica Acta Part A: Molecular and Biomolecular Spectroscopy, 2005. **61**(7): p. 1529-1535.
156. Czamara, K., et al., *Raman spectroscopy of lipids: a review.* Journal of Raman Spectroscopy, 2015. **46**(1): p. 4-20.
157. Bitar, R.A., et al., *Biochemical analysis of human breast tissues using Fourier-transform Raman spectroscopy.* J Biomed Opt, 2006. **11**(5): p. 054001.
158. Shipp, D.W., F. Sinjab, and I. Notingher, *Raman spectroscopy: techniques and applications in the life sciences.* Advances in Optics and Photonics, 2017. **9**(2): p. 315-428.
159. Martinez, M.G., et al., *Characterisation of structural changes in collagen with Raman spectroscopy.* Applied Spectroscopy Reviews, 2019. **54**(6): p. 509-542.
160. Cheng, W.-T., et al., *Micro-Raman spectroscopy used to identify and grade human skin pilomatrixoma.* Microscopy Research and Technique, 2005. **68**(2): p. 75-79.
161. Becker, L., et al., *Raman microspectroscopy identifies fibrotic tissues in collagen-related disorders via deconvoluted collagen type I spectra.* Acta Biomaterialia, 2023. **162**: p. 278-291.
162. Becker, L., et al., *Raman Imaging and Fluorescence Lifetime Imaging Microscopy for Diagnosis of Cancer State and Metabolic Monitoring.* Cancers, 2021. **13**(22): p. 5682.
163. Huang, Z., et al., *Near-infrared Raman spectroscopy for optical diagnosis of lung cancer.* International Journal of Cancer, 2003. **107**(6): p. 1047-1052.
164. Movasaghi, Z., S. Rehman, and I.U. Rehman, *Raman Spectroscopy of Biological Tissues.* Applied Spectroscopy Reviews, 2007. **42**(5): p. 493-541.
165. Ó Faoláin, E., et al., *A study examining the effects of tissue processing on human tissue sections using vibrational spectroscopy.* Vibrational Spectroscopy, 2005. **38**(1): p. 121-127.
166. Malini, R., et al., *Discrimination of normal, inflammatory, premalignant, and malignant oral tissue: a Raman spectroscopy study.* Biopolymers, 2006. **81**(3): p. 179-93.
167. Frost, R.L., et al., *Raman spectroscopy of selected lead minerals of environmental significance.* Spectrochimica Acta Part A: Molecular and Biomolecular Spectroscopy, 2003. **59**(12): p. 2705-2711.
168. Mostaert, A.S., et al., *Mechanically functional amyloid fibrils in the adhesive of a marine invertebrate as revealed by Raman spectroscopy and atomic force microscopy.* Archives of histology and cytology, 2009. **72**(4+ 5): p. 199-207.
169. Mensch, C., et al., *Raman optical activity of human α-synuclein in intrinsically disordered, micelle-bound α-helical, molten globule and*

oligomeric β-sheet state. Journal of Raman Spectroscopy, 2017. **48**(7): p. 910-918.
170. Maiti, N.C., et al., *Raman spectroscopic characterization of secondary structure in natively unfolded proteins: α-synuclein.* Journal of the American Chemical Society, 2004. **126**(8): p. 2399-2408.
171. Frushour, B.G. and J.L. Koenig, *Raman scattering of collagen, gelatin, and elastin.* Biopolymers: Original Research on Biomolecules, 1975. **14**(2): p. 379-391.
172. Barron, L.D., et al., *Structure and behaviour of proteins, nucleic acids and viruses from vibrational Raman optical activity.* Spectroscopy, 2003. **17**(2-3): p. 101-126.
173. Apetri, M.M., et al., *Secondary structure of α-synuclein oligomers: characterization by raman and atomic force microscopy.* Journal of molecular biology, 2006. **355**(1): p. 63-71.
174. Alimova, A., et al., *In vivo molecular evaluation of guinea pig skin incisions healing after surgical suture and laser tissue welding using Raman spectroscopy.* Journal of Photochemistry and Photobiology B: Biology, 2009. **96**(3): p. 178-183.
175. Gąsior-Głogowska, M., et al., *FT-Raman spectroscopic study of human skin subjected to uniaxial stress.* Journal of the Mechanical Behavior of Biomedical Materials, 2013. **18**: p. 240-252.
176. Frushour, B.G. and J.L. Koenig, *Raman scattering of collagen, gelatin, and elastin.* Biopolymers, 1975. **14**(2): p. 379-391.
177. Maiti, N.C., et al., *Raman Spectroscopic Characterization of Secondary Structure in Natively Unfolded Proteins: α-Synuclein.* Journal of the American Chemical Society, 2004. **126**(8): p. 2399-2408.
178. Gremlich, H.-U. and B. Yan, *Infrared and Raman spectroscopy of biological materials*. 2000: CRC press.
179. Takeuchi, M., S. Kajimoto, and T. Nakabayashi, *Experimental Evaluation of the Density of Water in a Cell by Raman Microscopy.* The Journal of Physical Chemistry Letters, 2017. **8**(21): p. 5241-5245.
180. Wiercigroch, E., et al., *Raman and infrared spectroscopy of carbohydrates: A review.* Spectrochimica Acta Part A: Molecular and Biomolecular Spectroscopy, 2017. **185**: p. 317-335.
181. Chen, Y., et al., *Raman spectroscopy analysis of the biochemical characteristics of molecules associated with the malignant transformation of gastric mucosa.* PLoS One, 2014. **9**(4): p. e93906.
182. Unal, M., H. Jung, and O. Akkus, *Novel Raman Spectroscopic Biomarkers Indicate That Postyield Damage Denatures Bone's Collagen.* Journal of Bone and Mineral Research, 2016. **31**(5): p. 1015-1025.
183. Dong, J., et al., *Insulin Assembly Damps Conformational Fluctuations: Raman Analysis of Amide I Linewidths in Native States and Fibrils.* Journal of Molecular Biology, 2003. **330**(2): p. 431-442.
184. Ortiz, C., et al., *Validation of the drop coating deposition Raman method for protein analysis.* Analytical Biochemistry, 2006. **353**(2): p. 157-166.
185. Camerlingo, C., et al., *μ-FTIR, μ-Raman, and SERS Analysis of Amide I Spectral Region in Oral Biofluid Samples during Orthodontic Treatment.* Sensors (Basel), 2022. **22**(20).

186. Wisniewski, M., et al., *Spectroscopic study of a KrF excimer laser treated surface of the thin collagen films.* Journal of Photochemistry and Photobiology A: Chemistry, 2007. **188**(2-3): p. 192-199.
187. Chandra, G., et al., *Evidence of conformational changes in adsorbed lysozyme molecule on silver colloids.* Int J Biol Macromol, 2010. **47**(3): p. 361-5.
188. Mensch, C., et al., *Raman optical activity of human α-synuclein in intrinsically disordered, micelle-bound α-helical, molten globule and oligomeric β-sheet state.* Journal of Raman Spectroscopy, 2017. **48**(7): p. 910-918.
189. Koster, H.J., et al., *Surface enhanced Raman scattering of extracellular vesicles for cancer diagnostics despite isolation dependent lipoprotein contamination.* Nanoscale, 2021. **13**: p. 14760 - 14776.
190. Malini, R., et al., *Discrimination of normal, inflammatory, premalignant, and malignant oral tissue: A Raman spectroscopy study.* Biopolymers, 2006. **81**(3): p. 179-193.
191. Sadeghi-Jorabchi, H., et al., *Determination of the total unsaturation in oils and margarines by fourier transform raman spectroscopy.* Journal of the American Oil Chemists' Society, 1990. **67**: p. 483-486.
192. T, P.W., et al., *Imaging of lipids in atherosclerotic lesion in aorta from ApoE/LDLR-/- mice by FT-IR spectroscopy and Hierarchical Cluster Analysis.* Analyst, 2011. **136**(24): p. 5247-55.
193. Killeen, D.P., et al., *Raman Spectroscopy of Fish Oil Capsules: Polyunsaturated Fatty Acid Quantitation Plus Detection of Ethyl Esters and Oxidation.* Journal of Agricultural and Food Chemistry, 2017. **65**(17): p. 3551-3558.
194. Frank, C.J., R.L. McCreery, and D.C. Redd, *Raman spectroscopy of normal and diseased human breast tissues.* Anal Chem, 1995. **67**(5): p. 777-83.
195. Kast, R.E., et al., *Raman spectroscopy can differentiate malignant tumors from normal breast tissue and detect early neoplastic changes in a mouse model.* Biopolymers, 2008. **89**(3): p. 235-41.
196. Lakshmi, R.J., et al., *Tissue Raman Spectroscopy for the Study of Radiation Damage: Brain Irradiation of Mice.* Radiation Research, 2002. **157**(2): p. 175-182.
197. Mahadevan-Jansen, A., et al., *Near-infrared Raman spectroscopy for in vitro detection of cervical precancers.* Photochem Photobiol, 1998. **68**(1): p. 123-32.
198. Nemecek, D., J. Stepanek, and G.J. Thomas, Jr., *Raman spectroscopy of proteins and nucleoproteins.* Curr Protoc Protein Sci, 2013. **Chapter 17**: p. Unit17.8.
199. Dukor, R.K., *Vibrational Spectroscopy in the Detection of Cancer*, in *Handbook of Vibrational Spectroscopy*. 2001.
200. Jackson, M., et al., *Beware of connective tissue proteins: Assignment and implications of collagen absorptions in infrared spectra of human tissues.* Biochimica et Biophysica Acta (BBA) - Molecular Basis of Disease, 1995. **1270**(1): p. 1-6.

201. De Meutter, J. and E. Goormaghtigh, *Evaluation of protein secondary structure from FTIR spectra improved after partial deuteration.* European Biophysics Journal, 2021. **50**(3): p. 613-628.
202. Goormaghtigh, E., V. Cabiaux, and J.-M. Ruysschaert, *Determination of Soluble and Membrane Protein Structure by Fourier Transform Infrared Spectroscopy*, in *Physicochemical Methods in the Study of Biomembranes*, H.J. Hilderson and G.B. Ralston, Editors. 1994, Springer US: Boston, MA. p. 329-362.
203. Wolpert, M. and P. Hellwig, *Infrared spectra and molar absorption coefficients of the 20 alpha amino acids in aqueous solutions in the spectral range from 1800 to 500cm−1.* Spectrochimica Acta Part A: Molecular and Biomolecular Spectroscopy, 2006. **64**(4): p. 987-1001.
204. Unal, M., et al., *Compositional assessment of bone by Raman spectroscopy.* Analyst, 2021. **146**(24): p. 7464-7490.
205. Votteler, M., et al., *Non-contact, label-free monitoring of cells and extracellular matrix using Raman spectroscopy.* J Vis Exp, 2012(63).
206. Novikova, T., *Optical techniques for cervical neoplasia detection.* Beilstein J Nanotechnol, 2017. **8**: p. 1844-1862.
207. Kumamoto, Y., et al., *Label-free Molecular Imaging and Analysis by Raman Spectroscopy.* Acta Histochem Cytochem, 2018. **51**(3): p. 101-110.
208. Ramakrishnaiah, R., et al., *Applications of Raman spectroscopy in dentistry part II: Soft tissue analysis.* Applied Spectroscopy Reviews, 2016. **51**: p. 799 - 821.
209. Yang, Y., et al., *Differential diagnosis of breast cancer using quantitative, label-free and molecular vibrational imaging.* Biomedical Optics Express, 2011. **2**(8): p. 2160-2174.
210. D'Acunto, M., et al., *Contribution of Raman Spectroscopy to Diagnosis and Grading of Chondrogenic Tumors.* Scientific Reports, 2020. **10**(1): p. 2155.
211. Bensalah, K., et al., *Raman spectroscopy: a novel experimental approach to evaluating renal tumours.* Eur Urol, 2010. **58**(4): p. 602-8.
212. Hollon, T., et al., *Near real-time intraoperative brain tumor diagnosis using stimulated Raman histology and deep neural networks.* Nature Medicine, 2020. **26**: p. 1-7.
213. Pavićević, A., et al., *Raman microspectroscopy as a biomarking tool for in vitro diagnosis of cancer: a feasibility study.* Croat Med J, 2012. **53**(6): p. 551-7.
214. Ji, M., et al., *Rapid, Label-Free Detection of Brain Tumors with Stimulated Raman Scattering Microscopy.* Science Translational Medicine, 2013. **5**(201): p. 201ra119-201ra119.
215. Ember, K.J.I., et al., *Raman spectroscopy and regenerative medicine: a review.* NPJ Regen Med, 2017. **2**: p. 12.
216. Laing, S., et al., *Surface-enhanced Raman spectroscopy for in vivo biosensing.* Nature Reviews Chemistry, 2017. **1**(8): p. 0060.
217. Pelissier, A., *Intelligent measurement analysis on single cell Raman images for the diagnosis of follicular thyroid carcinoma.* arXiv preprint arXiv:1904.05675, 2019.

218. Dochow, S., et al., *Comparing Raman and fluorescence lifetime spectroscopy from human atherosclerotic lesions using a bimodal probe.* Journal of Biophotonics, 2016. **9**(9): p. 958-966.
219. Drifka, C.R., et al., *Comparison of Picrosirius Red Staining With Second Harmonic Generation Imaging for the Quantification of Clinically Relevant Collagen Fiber Features in Histopathology Samples.* J Histochem Cytochem, 2016. **64**(9): p. 519-29.
220. Smith, S., et al., *P158 Raman Spectroscopy demonstrates biomolecular changes and predicts response to biological therapy in inflammatory bowel disease*. Vol. 70. 2021. A125.1-A125.
221. Beyer, T. and L. Becker, *Marker-independent imaging reveals a correlation of fibrotic and epigenetic alterations in endometriosis.* 2024.
222. Jiang, L., et al., *Inflammation and endometriosis.* Front Biosci (Landmark Ed), 2016. **21**(5): p. 941-8.
223. Suthahar, N., et al., *From Inflammation to Fibrosis—Molecular and Cellular Mechanisms of Myocardial Tissue Remodelling and Perspectives on Differential Treatment Opportunities.* Current Heart Failure Reports, 2017. **14**(4): p. 235-250.
224. Chimenti, I., et al., *Editorial: Fibrosis and Inflammation in Tissue Pathophysiology.* Front Physiol, 2021. **12**: p. 830683.
225. Muschler, J. and C.H. Streuli, *Cell-Matrix Interactions in Mammary Gland Development and Breast Cancer.* Cold Spring Harbor Perspectives in Biology, 2010. **2**(10): p. a003202-a003202.
226. Abraham, E.T., et al., *Collagen's primary structure determines collagen:HSP47 complex stoichiometry.* J Biol Chem, 2021. **297**(6): p. 101169.
227. Zeichen, J., et al., *Die Expression von Typ-VI-Kollagen bei der ArthrofibroseEine immunhistochemische Untersuchung*.* Der Unfallchirurg, 2000. **103**(8): p. 640-644.
228. Karsdal, M.A., et al., *The good and the bad collagens of fibrosis - Their role in signaling and organ function.* Adv Drug Deliv Rev, 2017. **121**: p. 43-56.
229. Rich, L. and P. Whittaker, *Collagen and picrosirius red staining: a polarized light assessment of fibrillar hue and spatial distribution.* Biology, 2005.
230. Matsuzaki, S., et al., *Fibrogenesis in Peritoneal Endometriosis: A Semi-Quantitative Analysis of Type-I Collagen.* Gynecologic and Obstetric Investigation, 1999. **47**(3): p. 197-199.
231. Rygula, A., et al., *Raman spectroscopy of proteins: a review.* Journal of Raman Spectroscopy, 2013. **44**(8): p. 1061-1076.
232. Marcelino, A.M. and L.M. Gierasch, *Roles of beta-turns in protein folding: from peptide models to protein engineering.* Biopolymers, 2008. **89**(5): p. 380-91.
233. Krafft, C., et al., *Near infrared Raman spectroscopic mapping of native brain tissue and intracranial tumors.* Analyst, 2005. **130**(7): p. 1070-7.
234. Andrus, P.G. and R.D. Strickland, *Cancer grading by Fourier transform infrared spectroscopy.* Biospectroscopy, 1998. **4**(1): p. 37-46.

235. Yu, C.-X., et al., *Correlation between replicative senescence of endometrial gland epithelial cells in shedding and non-shedding endometria and endometriosis cyst during menstruation.* Gynecological Endocrinology, 2018. **34**(11): p. 981-986.
236. Evers, J.L. and D. Willebrand, *The basement membrane in endometriosis.* Fertil Steril, 1987. **47**(3): p. 505-7.
237. Wilson, R.B., *Hypoxia, cytokines and stromal recruitment: parallels between pathophysiology of encapsulating peritoneal sclerosis, endometriosis and peritoneal metastasis.* Pleura Peritoneum, 2018. **3**(1): p. 20180103.
238. D'Alterio, M.N., et al., *Management Challenges of Deep Infiltrating Endometriosis.* Int J Fertil Steril, 2021. **15**(2): p. 88-94.
239. Barron, L.D., et al., *Solution structure and dynamics of biomolecules from Raman optical activity.* Progress in biophysics and molecular biology, 2000. **73 1**: p. 1-49.
240. Carpinteri, A., et al., *Global Vibrational Modes in Proteins: Raman Spectroscopy and Numerical Modeling*. 2018. p. 15-18.
241. Lee, D., et al., *Adsorption of dipeptide L-alanyl-L-tryptophan on gold colloidal nanoparticles studied by surface-enhanced Raman spectroscopy.* Spectrochimica Acta Part A: Molecular and Biomolecular Spectroscopy, 2021. **247**: p. 119064.
242. Barth, A., *Infrared spectroscopy of proteins.* Biochimica et Biophysica Acta (BBA) - Bioenergetics, 2007. **1767**(9): p. 1073-1101.
243. Kerfah, R., et al., *CH3-specific NMR assignment of alanine, isoleucine, leucine and valine methyl groups in high molecular weight proteins using a single sample.* Journal of Biomolecular NMR, 2015. **63**(4): p. 389-402.
244. Berg, J.M., et al., *Zusammensetzung und Struktur der Proteine*, in *Stryer Biochemie*, J.M. Berg, et al., Editors. 2018, Springer Berlin Heidelberg: Berlin, Heidelberg. p. 31-77.
245. Ortega, Á., *Methylation of Proteins: Biochemistry and Functional Consequences*, in *Cellular Ecophysiology of Microbe: Hydrocarbon and Lipid Interactions*, T. Krell, Editor. 2018, Springer International Publishing: Cham. p. 571-584.
246. Critchley, H.O.D., et al., *Physiology of the Endometrium and Regulation of Menstruation.* Physiol Rev, 2020. **100**(3): p. 1149-1179.
247. Garcia Garcia, J.M., et al., *Endometriosis: Cellular and Molecular Mechanisms Leading to Fibrosis.* Reproductive Sciences, 2023. **30**(5): p. 1453-1461.
248. Hill, C.J., et al., *Endometriosis and the Fallopian Tubes: Theories of Origin and Clinical Implications.* J Clin Med, 2020. **9**(6).
249. Fidler, A.L., et al., *The triple helix of collagens – an ancient protein structure that enabled animal multicellularity and tissue evolution.* Journal of Cell Science, 2018. **131**(7).
250. Gargett, C.E., H.P. Nguyen, and L. Ye, *Endometrial regeneration and endometrial stem/progenitor cells.* Rev Endocr Metab Disord, 2012. **13**(4): p. 235-51.
251. Chui, M.H., T.L. Wang, and I.M. Shih, *Endometriosis: benign, malignant, or something in between?* Oncotarget, 2017. **8**(45): p. 78263-78264.

252. Cárcamo, J.J., et al., *Raman study of the shockwave effect on collagens.* Spectrochimica Acta Part A: Molecular and Biomolecular Spectroscopy, 2012. **86**: p. 360-365.
253. Smolarz, B., K. Szyłło, and H. Romanowicz, *Endometriosis: Epidemiology, Classification, Pathogenesis, Treatment and Genetics (Review of Literature).* Int J Mol Sci, 2021. **22**(19).
254. Dutta, M., et al., *Metabolomics reveals perturbations in endometrium and serum of minimal and mild endometriosis.* Scientific Reports, 2018. **8**(1): p. 6466.
255. Baiocchini, A., et al., *Extracellular Matrix Molecular Remodeling in Human Liver Fibrosis Evolution.* PLoS One, 2016. **11**(3): p. e0151736.
256. Reynaud, E., *Protein misfolding and degenerative diseases.* Nat. Educ., 2010. **3**.
257. Marchandot, B., et al., *Endometriosis and cardiovascular disease.* Eur Heart J Open, 2022. **2**(1): p. oeac001.
258. Mu, F., et al., *Association Between Endometriosis and Hypercholesterolemia or Hypertension.* Hypertension, 2017. **70**(1): p. 59-65.
259. Melo, A.S., et al., *Unfavorable lipid profile in women with endometriosis.* Fertility and Sterility, 2010. **93**(7): p. 2433-2436.
260. von der Saal, K., *Lipide und Zellmembranen*, in *Biochemie*, K. von der Saal, Editor. 2020, Springer Berlin Heidelberg: Berlin, Heidelberg. p. 57-66.
261. Weijers, R.N., *Membrane flexibility, free fatty acids, and the onset of vascular and neurological lesions in type 2 diabetes.* J Diabetes Metab Disord, 2015. **15**: p. 13.
262. Noutsi, P., E. Gratton, and S. Chaieb, *Assessment of Membrane Fluidity Fluctuations during Cellular Development Reveals Time and Cell Type Specificity.* PLoS One, 2016. **11**(6): p. e0158313.
263. Ammendolia, D.A., W.M. Bement, and J.H. Brumell, *Plasma membrane integrity: implications for health and disease.* BMC Biology, 2021. **19**(1): p. 71.
264. Chen, J., et al., *Unlocking the mysteries of VLDL: exploring its production, intracellular trafficking, and metabolism as therapeutic targets.* Lipids in Health and Disease, 2024. **23**(1): p. 14.
265. Lee, H.C., A. Akhmedov, and C.H. Chen, *Spotlight on very-low-density lipoprotein as a driver of cardiometabolic disorders: Implications for disease progression and mechanistic insights.* Front Cardiovasc Med, 2022. **9**: p. 993633.
266. Chiurchiù, V., A. Leuti, and M. Maccarrone, *Bioactive Lipids and Chronic Inflammation: Managing the Fire Within.* Front Immunol, 2018. **9**: p. 38.
267. Lee, Y.H., et al., *Dysregulated sphingolipid metabolism in endometriosis.* J Clin Endocrinol Metab, 2014. **99**(10): p. E1913-21.
268. Czamara, K., et al., *Unsaturated lipid bodies as a hallmark of inflammation studied by Raman 2D and 3D microscopy.* Scientific Reports, 2017. **7**(1): p. 40889.
269. Lukianova, L., et al., *Anti-Inflammatory Effect of Coxibs and their Compositions with Caffeine on the Level of Conjugated Dienes in the*

Formalin-Induced Edema Model. Journal of the Turkish Chemical Society Section A: Chemistry, 2022. **9**(4): p. 1029-1034.
270. Bik, E., et al., *Menadione-induced endothelial inflammation detected by Raman spectroscopy.* Biochimica et Biophysica Acta (BBA) - Molecular Cell Research, 2021. **1868**(2): p. 118911.
271. Maenhoudt, N., A. De Moor, and H. Vankelecom, *Modeling Endometrium Biology and Disease.* J Pers Med, 2022. **12**(7).
272. Murgia, F., et al., *Metabolic Profile of Patients with Severe Endometriosis: a Prospective Experimental Study.* Reproductive Sciences, 2021. **28**(3): p. 728-735.
273. Chiriboga, L., et al., *Infrared spectroscopy of human tissue. I. Differentiation and maturation of epithelial cells in the human cervix.* Biospectroscopy, 1998. **4**(1): p. 47-53.
274. Lu, C., et al., *Chronic Stress Blocks the Endometriosis Immune Response by Metabolic Reprogramming.* International Journal of Molecular Sciences, 2024. **25**(1): p. 29.
275. Young, V.J., et al., *Transforming Growth Factor-β Induced Warburg-Like Metabolic Reprogramming May Underpin the Development of Peritoneal Endometriosis.* The Journal of Clinical Endocrinology & Metabolism, 2014. **99**(9): p. 3450-3459.
276. Lebovic, D.I., M.D. Mueller, and R.N. Taylor, *Immunobiology of endometriosis.* Fertil Steril, 2001. **75**(1): p. 1-10.
277. Yassine, W., et al., *Reversible transition between α-helix and β-sheet conformation of a transmembrane domain.* Biochimica et Biophysica Acta (BBA) - Biomembranes, 2009. **1788**(9): p. 1722-1730.
278. Nothinger, I. and L.L. Hench, *Raman microspectroscopy: a noninvasive tool for studies of individual living cells in vitro.* Expert Rev Med Devices, 2006. **3**(2): p. 215-234.
279. Chan, J.W., et al., *Micro-Raman Spectroscopy Detects Individual Neoplastic and Normal Hematopoietic Cells.* Biophysical Journal, 2006. **90**(2): p. 648-656.
280. Nothinger, I., J. Selvakumaran, and L.L. Hench, *New detection system for toxic agents based on continuous spectroscopic monitoring of living cells.* Biosens Bioelectron, 2004. **20**(4): p. 780-789.
281. Stone, N., Kendall, C., Smith, J., Crow, P., Barr, H., *Raman spectroscopy for identification of epithelial cancers.* Faraday Discussions, 2004. **126**: p. 141-157.
282. Ruiz-Chica, A.J., et al., *Characterization by Raman spectroscopy of conformational changes on guanine–cytosine and adenine–thymine oligonucleotides induced by aminooxy analogues of spermidine.* Journal of Raman Spectroscopy, 2004. **35**(2): p. 93-100.
283. Frank, C.J., R.L. McCreery, and D.C. Redd, *Raman spectroscopy of normal and diseased human breast tissues.* Anal Chem., 1995. **67**(5): p. 777-783.
284. Letsiou, S., et al., *Transcriptional and epigenetic effects of Vitis vinifera L. leaf extract on UV-stressed human dermal fibroblasts.* Molecular Biology Reports, 2020. **47**(8): p. 5763-5772.

285. Butler, H.J., et al., *Using Raman spectroscopy to characterize biological materials.* Nature Protocols, 2016. **11**(4): p. 664-687.
286. Atkins, C.G., et al., *Raman Spectroscopy of Blood and Blood Components.* Applied Spectroscopy, 2017. **71**(5): p. 767-793.
287. Monici, M., *Cell and tissue autofluorescence research and diagnostic applications.* Biotechnol Annu Rev, 2005. **11**: p. 227-56.
288. Demtröder, W., *Laser Raman Spectroscopy*. 2015, Springer Berlin Heidelberg. p. 149-181.
289. Yanina, I.Y., E.N. Lazareva, and V.V. Tuchin, *Refractive index of adipose tissue and lipid droplet measured in wide spectral and temperature ranges.* Appl Opt, 2018. **57**(17): p. 4839-4848.
290. Notingher, I., et al., *Discrimination between ricin and sulphur mustard toxicity in vitro using Raman spectroscopy.* Journal of The Royal Society Interface, 2004. **1**(1): p. 79-90.
291. Ó Faoláin, E., et al., *A study examining the effects of tissue processing on human tissue sections using vibrational spectroscopy.* Vibrational Spectroscopy, 2005. **38**(1-2): p. 121-127.

8 Erklärung zum Eigenanteil

Die Arbeit wurde am Department für Frauengesundheit der Universität Tübingen und an der AG Schenke-Layland in Tübingen unter der Betreuung von Herrn Prof. Dr. med. Martin Weiss und Frau Prof. Dr. rer. nat. Katja Schenke-Layland (Doktormutter) durchgeführt. Die Konzeption der Studie erfolgte durch Herrn Jun. Prof. Dr. med. Martin Weiss und mich selbst. Sämtliche Versuche wurden nach Einarbeitung durch Labormitglieder (Dr. rer. nat. Julia Marzi, Simone Liebscher, Daniel Carvajal Berrio, Dr. rer. nat. Eva Brauchle) eigenständig an die Fragestellung adaptiert und durchgeführt. Bei der Auswertung der Ergebnisse des Raman-Imagings wurde ich unterstützt durch Frau Dr. rer. nat. Julia Marzi, Herrn Daniel Carvajal Berrio und Herrn Dr. rer. nat. Lucas Becker. Die Probenvorbereitung und -behandlung wurde durch mich durchgeführt. Die statistische Auswertung erfolgte eigenständig nach Rücksprache mit Prof. Dr. med. Martin Weiss durch mich. Ich versichere, das Manuskript selbstständig verfasst zu haben und keine weiteren als die von mir angegebenen Quellen verwendet zu haben. Die wörtlich übernommenen Textpassagen aus der Originalpublikation wurden von mir selbst verfasst. Sämtliche übernommenen und / oder modifizierten Abbildungen wurden ebenfalls von mir selbst unter der Aufsicht von Jun. Prof. Dr. med. Martin Weiss entworfen.

Tübingen, den

07.07.2025

9 Veröffentlichungen

Marker-independent imaging reveals a correlation of fibrotic and epigenetic alterations in endometriosis.

Tara Beyer [a,c§,], Lucas Becker [a,b§], Simone Liebscher [a], Carvajal-Berrio [a,b], Hans Bösmüller, Katharina Rall [c], Sara Y Brucker [c], Katja Schenke-Layland [a,b,e], Martin Weiss [c,e] and Julia Marzi [*a,b,e]

10 Danksagung

I would like to express my deepest gratitude to Prof. Dr. Katja Schenke-Layland for giving me the opportunity to conduct my thesis at the AG Schenke-Layland, a truly inspiring and nurturing environment both professionally and personally. My sincere thanks also go to my supervisor, Jun. Prof. Dr. med. Martin Weiss, for his unwavering support, insightful guidance, and encouragement throughout this journey. I am profoundly grateful to Dr. rer. nat. Julia Marzi and Dr. rer. nat. Eva Brauchle for their invaluable expertise, patience, and dedication in helping me navigate the complexities of my research and shaping this work to its current form. I also wish to thank Daniel Carvajal Berrio and Simone Liebscher for their exceptional assistance, not only during my experiments but also in offering support beyond the laboratory, always ready to answer questions and lend a hand. I am also thankful to Dr. rer. nat. Lucas Becker, who joined me on this project and carried it forward. My heartfelt appreciation goes to the entire Schenke-Layland lab family, who made my time here an enjoyable and enriching experience. The lunchtime conversations have been and still are a constant source of joy.

Lastly, I am deeply thankful to my family and friends, whose unwavering support, encouragement, and resilience have been the foundation of my journey. I would especially like to mention David Venus and Prof. (apl.) Dr. med. Dominik Saul for the inspiring conversations and the occasional push that kept me moving forward.